Institute of
Electrified Aero Engines

Brandenburg
University of Technology
Cottbus - Senftenberg

Design and Preparation of a Manufacturable Flux-Switching Machine

by

Aruli Karuppu Umapathi

Bachelor of Technology in Mechanical Engineering
SASTRA University, 2020

Performed at

German Aerospace Center (DLR)
Institute of Electrified Aero Engines
Cottbus

Submitted to the

Faculty of Mechanical Engineering, Electrical and Energy Systems

in partial fulfillment of the requirements for the degree of

Master of Science in Power Engineering

at the

Brandenburg University of Technology Cottbus - Senftenberg

May 2026

Authored by	:	Aruli Karuppu Umapathi
Matriculation number	:	5008917
Date of Registration	:	February 17, 2026
Date of Submission	:	

Institute Supervisor	:	M.Eng. Enrico Teichert, Research Associate, Component Technologies Department, Institute of Electrified Aero Engines
Academic 1st Supervisor	:	Prof. Dr. rer. nat. Lars Enghardt, Faculty of Mechanical Engineering, Electrical and Energy Systems, Brandenburg University of Technology Cottbus - Senftenberg
Academic 2nd Supervisor	:	M.Sc. Paul Abromeit, Faculty of Mechanical Engineering, Electrical and Energy Systems, Brandenburg University of Technology Cottbus - Senftenberg

Declaration

- The report embodies the results of my own work and has been composed by myself. All methodological developments, conceptual ideas, analyses, and implementations presented in this report have been carried out by me unless explicitly stated otherwise.
- Where appropriate, I have made acknowledgment of the work of others and have made reference to work carried out in collaboration with other persons.
- The report is the correct version of the report for submission and is the same version as any electronic versions submitted*.
- I understand that as a student of the University I am required to abide by the Regulations of the University and to conform to its discipline.
- I confirm that the report has been verified against plagiarism via an approved plagiarism detection application e.g. Turnitin.
- I declare that the lecturer can submit the electronic copy of the report to a plagiarism detection application e.g. Turnitin.
- Artificial intelligence tools were used in this thesis solely for grammatical corrections, linguistic refinement, and for the generation of utility scripts used for data post-processing and simulation automation.

* Please note that it is the responsibility of the student to ensure that the correct version of the report is submitted.

Name of the student: **Aruli Karuppu Umapathi**
Date:

Signature of the student:

Acknowledgements

I would like to express my sincere gratitude to the Director of the **Institute of Electrified Aero Engines**, **Prof. Dr. rer. nat. Lars Enghardt**, to the Head of the Component Technologies Department, **Dr.-Ing. Stefan Kazula**, and to **Dr.-Ing. Ilja Koch**, Team Leader for Electric Drives and Power Electronics (EAL), for providing me with the opportunity to conduct my Master's thesis at this esteemed institute.

I am profoundly grateful to my institute supervisor, **M.Eng. Enrico Teichert**, whose unwavering support and dedication have been instrumental throughout the course of this work. His patience, generosity in sharing knowledge, and constant encouragement have not only guided this thesis but have also greatly shaped my professional growth. I am sincerely thankful for the trust he placed in me, the continuous learning opportunities he provided, and the kindness and understanding he consistently showed. His mentorship has been invaluable, and I remain deeply appreciative of all the time and effort he invested in my development.

My heartfelt thanks also go to **Dr.-Ing. Matthias Lang**, who supported me at various stages of the FEA modeling and also for contributing as a member of the senior panel during the technical workshop, and to **Dr.-Ing. Robert Goraj**, who provided valuable guidance in 3D FEA modeling. I am also sincerely grateful to **Dr. Amadeus Cavalcanti Salvador de Alcântara** for his insightful discussions and support during the brainstorming of optimization strategies.

Furthermore, I would like to extend my appreciation to **Dr.-Ing. Sebastian Hakansson**, and **M.Sc. André Vetterlein** for their valuable participation as members of the senior panel during the technical workshop conducted as part of this thesis. Their critical evaluation of the design and constructive suggestions significantly contributed to the refinement of this work.

Special thanks are extended to the entire **Component Technologies Department** at the Institute of Electrified Aero Engines for fostering a collaborative and enriching environment that greatly enhanced my research experience.

I would like to express my deepest gratitude to my family for their love, support, and encouragement throughout my academic journey.

Lastly, I would like to thank **Brandenburg University of Technology Cottbus-Senftenberg** for their academic guidance and support throughout the duration of my studies.

Abstract

To meet the strict targets of the Paris Agreement and Flightpath 2050, the aerospace sector is transitioning toward electric propulsion. While Permanent Magnet Synchronous Motors are widely used due to their high efficiency and power density [1], they face challenges related to cooling and magnet demagnetization, motivating the need to re-evaluate machine topologies. In this study, an outer-rotor Flux Switching Permanent Magnet (FSPM) machine is developed, which involves designing the machine with mechanical constraints derived from utilizing the Hacker Q150 motor components. In addition, electrical constraints such as a maximum DC supply voltage limit of 100 V and a phase RMS current limit of 80 A arising from the existing experimental test setup are also included. These constraints enable the performance enhancement of the machine under study through the geometric optimization of the magnetic circuit. The parametrically developed 2D base model was analyzed for electromagnetic performance characteristics through magnetostatic and transient analyses. Three optimization approaches, Parametric Sweep Optimization, Direct Optimization, and Meta-Model-Based Optimization, are implemented and compared to find optimal tradeoffs between average torque, efficiency, and torque ripple. The chosen design is validated through 3D finite element analysis to account for end-winding effects and axial flux leakage. Finally, the chosen design is translated into a manufacturable prototype, involving mechanical assembly development and technical drawing preparation. In addition, a structured failure mode analysis is conducted through a technical workshop to identify potential risks across electromagnetic, mechanical, and manufacturing domains, ensuring robustness and practical reliability of the proposed design with the help of a 3D-printed functional mock-up. The results show that a constraint-driven optimization approach enables the realization of a high-performance FSPM machine while maintaining practical feasibility and highlights the effectiveness of advanced optimization methodologies for highly coupled electromagnetic systems.

Contents

List of Abbreviations

Abbreviations and Acronyms

Abbreviation	**Meaning**
2D	Two-dimensional
3D	Three-dimensional
AC	Alternating Current
ALHS	Adaptive Latin Hypercube Sampling
ATAG	Air Transport Action Group
BEM	Boundary Element Method
BEV	Battery Electric Vehicle
BLAC	Brushless Alternating Current
BLDC	Brushless Direct Current
CAD	Computer-Aided Design
CNC	Computer Numerical Control
CO_2	Carbon dioxide
COP	Coefficient of Prognosis
DC	Direct Current
DLR	Deutsches Zentrum für Luft- und Raumfahrt
DSPM	Doubly Salient Permanent Magnet
Dy	Dysprosium
EA	Evolutionary Algorithm
EAL	Elektrische Antriebe und Leistungselektronik
EASA	European Union Aviation Safety Agency
EMF	Electromotive Force
EV	Electric Vehicle
FDM	Finite Difference Method
FEA	Finite Element Analysis
FEM	Finite Element Method
FOC	Field Oriented Control
FRM	Flux Reversal Permanent Magnet
FSM	Flux Switching Machine
FSPM	Flux Switching Permanent Magnet
FVM	Finite Volume Method
GD&T	Geometric Dimensioning and Tolerancing
HEV	Hybrid Electric Vehicle
H Q150	Hacker Q150 Motor
HVAC	Heating, Ventilation, and Air Conditioning
IATA	International Air Transport Association
ICE	Internal Combustion Engine
IEA	International Energy Agency
IM	Induction Machine
IPM	Interior Permanent Magnet
ISO	International Organization for Standardization
MOM	Method of Moments
MOO	Multi-Objective Optimization
MOP	Metamodel of Optimal Prognosis
NdFeB	Neodymium-Iron-Boron

Abbreviation	**Meaning**
NO_x	Nitrogen oxides
NSGA-II	Non-dominated Sorting Genetic Algorithm II
NVH	Noise, Vibration, and Harshness
PCD	Pitch Circle Diameter
PM	Permanent Magnet
PMSM	Permanent Magnet Synchronous Machine
PWM	Pulse Width Modulation
RMS	Root Mean Square
RSM	Response Surface Methodology
SAF	Sustainable Aviation Fuel
SPM	Surface Permanent Magnet
SPWM	Sinusoidal Pulse Width Modulation
SRM	Switched Reluctance Machine
SVPWM	Space Vector Pulse Width Modulation
UAM	Urban Air Mobility

Greek Symbols

Symbol	**Meaning**	**Unit**
α_{20}	Temperature coefficient of resistivity at 20°C	1/K
α_{R}	Rotor pole pitch angle	rad, degree
α_{S}	Stator pole pitch angle	rad, degree
β	Current angle	degree
β_{PM}	Permanent magnet arc angle	rad, degree
β_{R}	Rotor tooth arc angle	rad, degree
β_{S}	Total stator pole arc angle	rad, degree
β_s	Individual stator tooth arc angle	rad, degree
β_{Slot}	Slot opening arc angle	rad, degree
ϵ	Permittivity	F/m
η	Efficiency	%
η_{avg}	Average efficiency	%
$\eta_{\mathrm{avg,max}}$	Maximum value of average efficiency	—
$\eta_{\mathrm{avg,min}}$	Minimum value of average efficiency	—
$\eta_{\mathrm{avg,norm}}$	Min–Max normalized average efficiency	—
γ_{β_s}	Stator arc ratio / optimization ratio	—
γ_{R}	Rotor yoke thickness ratio coefficient	—
γ_{S}	Stator yoke thickness ratio coefficient	—
λ_d	d-axis flux linkage	Wb
λ_m	Magnet flux linkage / PM flux linkage term	Wb
λ_q	q-axis flux linkage	Wb
μ	Magnetic permeability	H/m
ν	Magnetic reluctivity	1/(H/m)
ω_e	Electrical angular speed	rad/s
π	Mathematical constant pi	—
ρ	Charge density / resistivity (context dependent)	C/m^3, Ωm
ρ_{20}	Copper resistivity at 20°C	Ωm
ρ_{Cu}	Copper resistivity at operating temperature	Ωm
θ	Electrical angle	rad, degree
$\theta_{\mathrm{initial}}$	Initial electrical angle / d-axis position	rad, degree
θ_{pitch}	Mean coil pitch angle	rad, degree
θ_{taper}	Rotor tooth taper angle	rad, degree
∇	Del (nabla) operator	—
$\nabla\cdot$	Divergence operator	—
$\nabla\times$	Curl operator	—
$\frac{\partial}{\partial t}$	Partial derivative with respect to time	—

Symbol	**Meaning**	**Unit**
$e^{j\frac{2\pi}{3}}$, $e^{j\frac{4\pi}{3}}$	Complex exponential operators	—
Ω	Feasible design space	—

Latin Symbols

Symbol	**Meaning**	**Unit**
$\mathbf{A}$	Magnetic vector potential vector	Wb/m
A_i	Nodal magnetic vector potential	Wb/m
A_{hs}	Slot-shoe / head-space related area term	mm^2
A_{shaft}	Shaft area	mm^2
A_{slot}	Slot area	mm^2
A_{stator}	Stator area	mm^2
A_{teeth}	Teeth area	mm^2
A_{wire}	Wire cross-sectional area	mm^2
A_{yoke}	Yoke area	mm^2
AG	Air gap length	mm
$\mathbf{B}$	Magnetic flux density vector	T
B_m	Peak flux density in core loss model	T
$\mathbf{D}$	Electric displacement field vector	$\mathrm{C/m}^2$
$\mathbf{E}$	Electric field vector	V/m
$\mathbf{F}$	Source vector in FEM formulation	—
$\mathbf{F}(\mathbf{x})$	Vector objective function	—
f	Electrical frequency	Hz
$f(\mathbf{x})$	Scalar objective function	—
$g_i(\mathbf{x})$	Inequality constraint function	—
$\mathbf{H}$	Magnetic field intensity vector	A/m
$h_j(\mathbf{x})$	Equality constraint function	—
hs_0	Radial slot opening height	mm
I_a, I_b, I_c	Three-phase currents	A
$I_{\mathrm{A}}, I_{\mathrm{B}}, I_{\mathrm{C}}$	Three-phase supply currents	A
I_d, I_q	*d*- and *q*-axis currents	A
I_{peak}	Peak current	A
$I_{\mathrm{phase,rms}}$	Phase RMS current	A
I_{rms}	RMS current	A
I_α, I_β	Clarke transformed currents	A
IRD	Inner rotor diameter	mm
$\mathbf{J}$	Current density vector	$\mathrm{A/m}^2$
J_{max}	Maximum current density	$\mathrm{A/mm}^2$
j	Imaginary unit	—
$[\mathbf{K}]$	Global stiffness / reluctance matrix	—
k_{e}	Classical eddy current loss coefficient	—
k_{ex}	Excess loss coefficient	—
k_{h}	Hysteresis loss coefficient	—
L_1, L_2	Measured edge lengths on rotor geometry	mm
$L_{\mathrm{A}}, L_{\mathrm{B}}, L_{\mathrm{C}}$	Three-phase inductors	H
L_{active}	Active stack length	mm
L_d, L_q	*d*- and *q*-axis inductances	H
$L_{\mathrm{edge,min}}$	Minimum edge length	mm
$L_{\mathrm{net_A}}$	Net inductance of phase A	H
$L_{\mathrm{self_A}}$	Self inductance of phase A	H
$L_{\mathrm{B.EMF},A}$, $L_{\mathrm{B.EMF},B}$ $L_{\mathrm{B.EMF},C}$	Inductors used for back EMF measurement	H
m	Number of phases	—
$M_{\mathrm{AB}}, M_{\mathrm{AC}}$	Mutual inductances between phases	H
M_{H}	Magnet height	mm

Symbol	**Meaning**	**Unit**
MLT	Mean length of one turn	mm
M_{T}	Magnet thickness	mm
N	Mechanical speed	rpm
$N_i(x, y)$	Shape function	—
N_{gen}	Maximum number of generations	—
N_{pop}	Surviving population	—
N_{pph}	Number of parallel paths per phase	—
N_{r}	Number of rotor poles	—
N_{s}	Number of stator slots / stator poles	—
N_{samples}	Total number of evaluated machine designs	—
N_{start}	Initial scatter population size	—
n	Positive integer / number of turns (context dependent)	—
ORD	Outer rotor diameter	mm
OSD	Outer stator diameter	mm
P	Pole pairs	—
P_{e}	Classical eddy current loss	W
P_{core}	Core loss	W
P_{Cu}	Copper loss	W
P_{ex}	Excess loss	W
P_{h}	Hysteresis loss	W
P_{magnet}	Magnet eddy current loss	W
P_{out}	Output power	W
p	Rotor pole number	—
$R_{\mathrm{A}}, R_{\mathrm{B}}, R_{\mathrm{C}}$	Three-phase resistors	Ω
R_{coil}	Resistance of one concentrated coil	Ω
R_{f}	Fillet ratio	—
R_{fillet}	Fillet radius	mm
R_{mean}	Geometric mean radius	mm
$R_{\mathrm{outer,taper}}$	Rotor tooth taper parameter	—
R_{phase}	Phase resistance	Ω
R_{thick}	Rotor thickness ratio / design variable	—
$R_{\mathrm{tooth,ratio}}$	Rotor tooth ratio parameter	—
$\mathbb{R}^n$	n-dimensional Euclidean space of real numbers	—
RTH	Rotor tooth height	mm
RTW	Rotor tooth width	mm
RYW	Rotor yoke width / thickness	mm
S	Effective coil overhang diameter	mm
S_{dia}	Shaft diameter	mm
S_{total}	Total weighted score	—
STH	Stator tooth height	mm
STW	Stator tooth width	mm
Strands	Number of strands per turn	—
SYW	Stator yoke width / thickness	mm
T_{amb}	Ambient temperature	°C
T_{avg}	Average torque	Nm
$T_{\mathrm{avg,max}}$	Maximum value of average torque	—
$T_{\mathrm{avg,min}}$	Minimum value of average torque	—
$T_{\mathrm{avg,norm}}$	Min–Max normalized average torque	—
T_e	Electromagnetic torque	Nm
T_{elec}	Electrical period	s
T_{rise}	Temperature rise	°C
T_{ripple}	Torque ripple	%
$T_{\mathrm{ripple,max}}$	Maximum value of torque ripple	—
$T_{\mathrm{ripple,min}}$	Minimum value of torque ripple	—
$T_{\mathrm{ripple,norm}}$	Inverted Min–Max normalized torque ripple	—
t	Time	s

Symbol	**Meaning**	**Unit**
V_a, V_b, V_c	Three-phase voltages	V
V_{DC}	DC-link voltage	V
V_d, V_q	d- and q-axis voltages	V
$V_{\text{L,A}}, V_{\text{L,B}}, V_{\text{L,C}}$	Three-phase inductance voltage drop	V
V_{peak}	Peak voltage	V
$V_{\text{phase,peak}}$	Phase peak voltage	V
$V_{\text{R,A}}, V_{\text{R,B}}, V_{\text{R,C}}$	Three-phase resistance voltage drop	V
$\mathbf{V}_s$	Voltage space vector	V
$V_{\text{BEMF},A}$, $V_{\text{BEMF},B}$, $V_{\text{BEMF},C}$	Three-phase back EMF voltages	V
w_1, w_2, w_3	Weighting coefficients	—
X	Untoothed circumference (air gap)	mm
$\mathbf{x}$	Design vector / optimization vector	—
Y	Untoothed circumference (slot depth)	mm
Δt	Time step	s
Error(%)	Absolute percentage deviation	%

Units

Unit	**Meaning**
%	Percent
°	Degree
°C	Degree Celsius
μH	Microhenry
Ω	Ohm
Ωm	Ohm metre
1/K	Per kelvin
A	Ampere
A/m	Ampere per metre
A/m^2	Ampere per square metre
A/mm^2	Ampere per square millimetre
C/m^3	Coulomb per cubic metre
C/m^2	Coulomb per square metre
degree	Degree
F/m	Farad per metre
H	Henry
H/m	Henry per metre
Hz	Hertz
kW	Kilowatt
mΩ	Milliohm
mm	Millimetre
mm^2	Square millimetre
MW	Megawatt
Nm	Newton metre
rad	Radian
rad/s	Radian per second
rpm	Revolutions per minute
s	Second
T	Tesla
V	Volt
V/m	Volt per metre
W	Watt
Wb	Weber

List of Figures

List of Tables

1 Introduction

The global climate crisis has reached a pivotal juncture. The average temperature around the world exceeded 1.48°C for a short time in 2024 and 2025, which was very close to the 1.5°C limit set by international treaties. The increase in global mean temperature over the last century shown in Figure 1, is an accelerating trend that puts the stability of planetary ecosystems at risk. A total of 196 parties signed the legally binding Paris Agreement in 2015 at the Conference of the Parties (COP 21) to halt this trend. The agreement established a global framework to keep the rise in global average temperature well below 2°C above pre-industrial levels, while also pursuing efforts to limit it to 1.5°C [2]. All industries are under pressure to reduce carbon emissions, yet the transportation sector remains a major contributor to global warming. The Cragoson 2024 report [3] states that the global transportation sector emitted 8.4 gigatons of CO_2 equivalent, representing 15.9% of total global emissions. The aviation industry accounts for 2% of total global emissions, corresponding to approximately 1 gigaton of CO_2 emissions per year. Commercial aviation is responsible for around 90% of these emissions [4], [5].

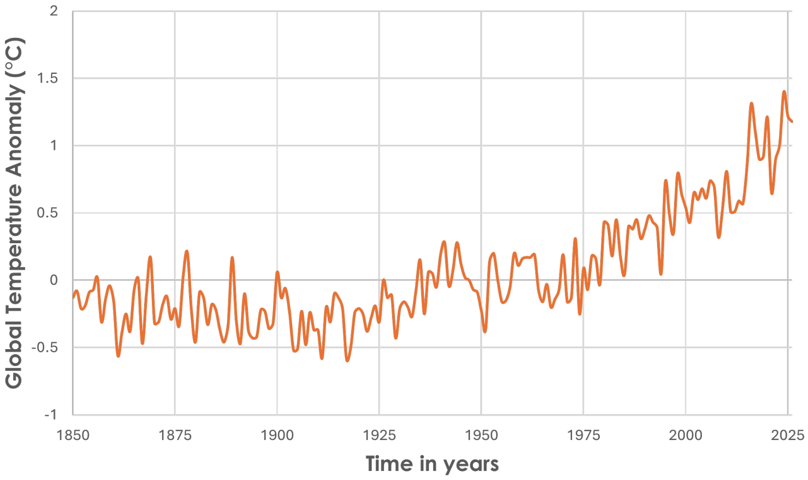

Figure 1: Global land and ocean temperature anomaly over time [6]

However, focusing solely on CO_2 significantly underestimates aviation's total climate impact. Unlike ground transport, aircraft emit pollutants in the upper troposphere and lower stratosphere. These non-CO_2 emissions including nitrogen oxides, soot, and water vapor trigger the formation of persistent contrails and cirrus clouds that trap terrestrial radiation. Recent studies by the European Union Aviation Safety Agency (EASA) indicate that these non-CO_2 effects account for approximately 66% of aviation's total effective radiative forcing [7]. Consequently, the industry's contribution to global warming is roughly three times higher than suggested by its CO_2 emissions alone. In response to these escalating environmental pressures, the European aviation sector has established rigorous technical performance goals. Issued by the European Commission, the "Flightpath 2050" vision provides the specific engineering mandates required to align aviation with the Paris Agreement. These goals are significantly more technical than the Paris Agreement, setting strict environmental targets.

The key objectives of Flightpath 2050 regarding environmental protection and energy supply area [8].

1. In 2050 technologies and procedures available allow a 75% reduction in CO_2 emissions per passenger kilometer to support the ATAG target and a 90% reduction in NO_x emissions. The perceived noise emission of flying aircraft is reduced by 65%. These are relative to the capabilities of typical new aircraft in 2000.
2. Aircraft movements are emission-free when taxiing.
3. Air vehicles are designed and manufactured to be recyclable.
4. Europe is established as a center of excellence on sustainable alternative fuels, including those for aviation, based on a strong European energy policy.
5. Europe is at the forefront of atmospheric research and takes the lead in the formulation of a prioritized environmental action plan and establishment of global environmental standards.

Meeting the Flightpath 2050 targets, specifically the 90% reduction in NOx and emission-free taxiing, is difficult with the current gas turbine technology. Even with the introduction of Sustainable Aviation Fuels (SAF), combustion engines continue to emit NOx and contrail-forming particles. The industry needs to look beyond thermodynamic improvements and fuel blends to reach true climate neutrality and meet the strict standards of Flightpath 2050. A suitable solution to this problem is to completely change how planes are powered and make them electric.

Conventional propulsion systems currently used in aviation are reaching their thermodynamic limits, with annual efficiency improvements typically in the range of 1 to 2% [9]. Meanwhile, the aviation sector is projected to emit approximately 21.2 gigatons of CO_2 between 2021 and 2050 under a business-as-usual scenario, which must be mitigated to achieve net zero targets [10]. Achieving this magnitude of reduction is not viable without a fundamental shift in propulsion technologies. ICE systems have been the mainstay of aviation for decades, but they have had a significant impact on the environment. In contrast, electric propulsion offers a paradigm shift in energy conversion. Electric motors typically operate at 90 to 95% efficiency, a stark contrast to the maximum 25 to 40% efficiency of various ICE architectures. This technology is already ubiquitous in other sectors; in fact, electric motor systems account for approximately 53% of the world's total electricity consumption [11]. Figure 2 illustrates typical applications of electric motors across these industries. In the heavy industrial and marine sectors, pioneers in electric machine manufacturing have already achieved efficiencies as high as 99.5% for large synchronous motors [12].

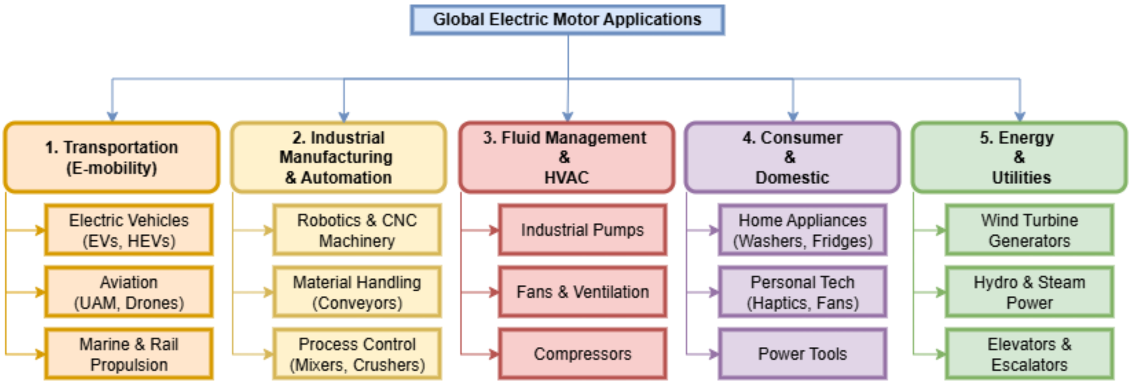

Figure 2: Global applications of electric motors across sectors

Beyond efficiency, electric motors offer distinct operational advantages for flight. Unlike air-breathing ICEs, electric motors do not require oxygen to produce torque and provide consistent power regardless of altitude or air density, enabling more efficient flight paths at higher altitudes. Electric powertrains are significantly quieter, a critical factor for the acceptance of Urban Air

Mobility (UAM) and reduced noise pollution. Moreover, an electric motor has vastly fewer moving parts than a piston or turbine engine, reducing maintenance complexity and cost. Crucially, electric motors produce zero CO_2, NO_x, or particulates during operation, directly addressing the non-CO_2 climate effects.

Globally the automotive industry has served as a proving ground for this transition, successfully adapting electric motors to create hybrid and battery electric vehicles (BEVs). The maturity of these technologies provides a foundation for aviation, although the requirements differ largely in scale and reliability.

1.1 Electrification

An electric motor is a device that converts electrical energy into mechanical energy with high reliability and limited critical parts. The classification of common electrical drives is illustrated in the Figure 3. While the automotive industry currently utilizes motors in the power range of several hundred kilowatts with specific power densities of 1 to 3 kW/kg [3], aviation imposes far stricter requirements. According to NASA's research on electrified propulsion, the specific power of electric machines must be drastically increased to make electric flight viable. To enable electric flight, high power densities are required to offset the significant weight penalty of energy storage systems [13]. NASA has identified that for single-aisle commercial transport, electric motors must achieve specific powers greater than 13 kW/kg with efficiencies exceeding 96% while operating at the megawatt (MW) power level [13].

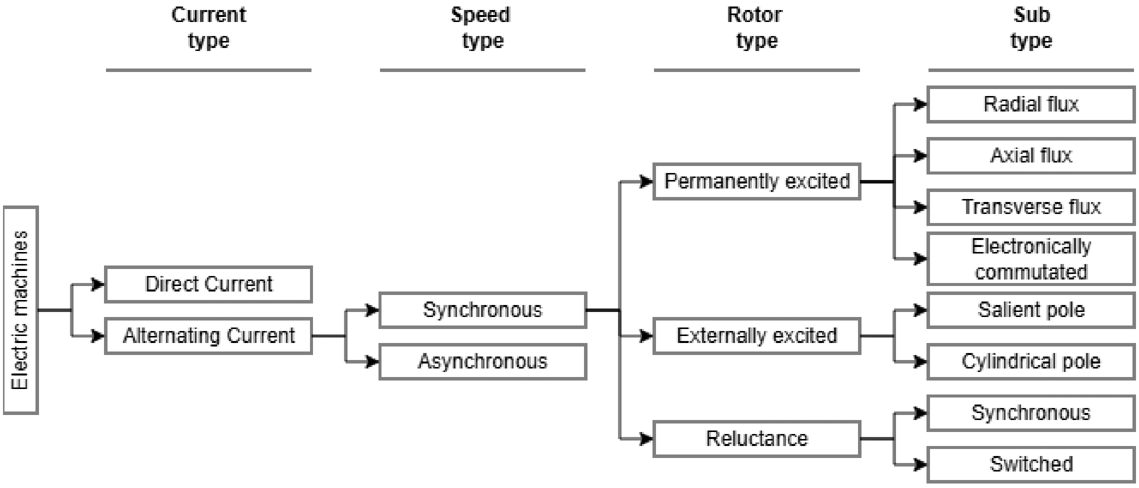

Figure 3: Classification of common electric motor topologies adopted from [1]

Among various motor topologies used in the automotive industry, primarily Induction Machines (IM), Permanent Magnet Synchronous Machines (PMSM), and Switched Reluctance Machines (SRM), the PMSMs have emerged as the dominant choice for high-performance applications [1], [14]. PMSMs are favored for aviation due to their superior power density, high efficiency, and compatibility with modern low-cost electronic control strategies. Within the PMSM category, two primary control and construction variants exist.

In control variants, Brushless DC motors are characterized by a trapezoidal back electromotive force (EMF) and driven by rectangular current waveforms. While they allow for simpler control and lower-cost position sensing, they suffer from higher torque ripple. Brushless AC motors have a sinusoidal back EMF and are powered by sinusoidal currents. These need very precise position sensors like resolvers and comparatively complicated vector control strategies, but they provide torque smoothly with little ripple, which makes them ideal for aviation propulsion. In terms of mechanical construction, PMSMs are grouped by where the magnets are placed. The magnets on Surface Permanent Magnet (SPM) motors are on the rotor's surface and face the air gap. At higher speeds, such rotor design can have trouble holding onto magnets, which often means adding non-magnetic bandage that makes the air gap bigger. Interior Permanent Magnet (IPM) motors have magnets embedded into the rotor laminations. No retaining bandage is required which makes these motors suitable for high-speed operation. Furthermore, due to increased saliency, flux weakening can be utilized to increase the speed range.

Despite the advantages of PMSMs, significant challenges remain regarding thermal management and materials used. Unlike the stator, which is stationary and can be cooled via liquid jackets or housing fins, the rotor is isolated. Heat generated in the rotor due to eddy currents and core losses must be evacuated through the shaft or bearings, a passive process that poses a risk of overheating. Excessive heat is particularly dangerous for Neodymium-Iron-Boron (NdFeB) magnets, which are the industry standard for high power density. Manufacturers add dysprosium (Dy) to the magnet alloy to keep it from becoming permanently demagnetized at higher temperatures. Adding more dysprosium raises the thermal limit, but it also makes the product much more expensive. The supply chain for these rare earth elements is also full of political tensions and environmental issues. The mining of neodymium and dysprosium is associated with environmental pollution. As shown in Figure 4, the volatility in raw material costs presents a strategic risk for the widespread scaling of electric aviation motors.

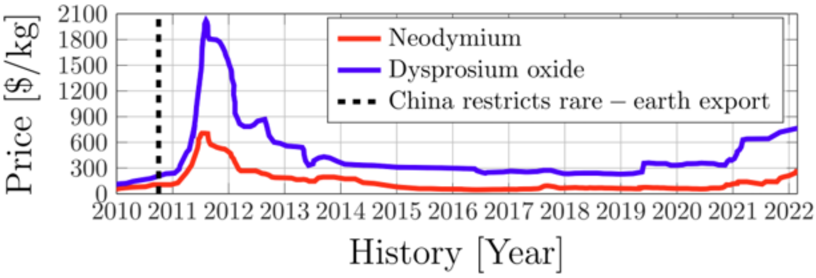

Figure 4: Price evolution of neodymium and dysprosium over the last decade [15]

1.2 Emergence of Stator-Permanent-Magnet Motors

To mitigate the reliance on expensive, heavy rare earth elements like dysprosium and to minimize the risk of thermal demagnetization, new electric machine topologies utilizing stator-mounted magnets have emerged. By relocating the excitation source from the rotating rotor to the stationary stator, these designs address the critical thermal limitations of conventional PMSMs. This arrangement enables easier cooling of the magnets via housing cooling jackets and allows for a simple, robust, and low-cost salient pole rotor, while retaining the high-power density of permanent magnets. The foundational study establishing this concept was published in 1955 by S.E. Rauch and L.J. Johnson. Their work introduced the "Flux-Switching Alternator," a high-frequency, single-phase machine where the magnetic flux was modulated by a robust, non-excited rotor, while both the magnets and armature windings remained stationary on the stator [16]. This topology laid the groundwork for modern Flux-Switching Machines (FSM).

Working Principle of FSM

The principle of operation of flux switching machines is different from the permanent magnet synchronous machines with rotor magnets. The FSM has a unique stator-excited configuration, which is different from traditional synchronous machines, where the excitation source rotates. The stator holds both the armature windings and the permanent magnets. The rotor in the FSM machine carries no magnets or excitation windings as in the SRM design; this design combines the advantages of both SRM and PMSM machines.

The basic idea depends on the flux switching mechanism, which changes the path of the magnetic flux made by the stationary magnets when the salient rotor poles rotate. The stator in a conventional FSM consists of U-shaped modular cores with permanent magnets sandwiched between them. Crucially, these magnets are magnetized circumferentially in alternating directions, which creates a flux-focusing effect. The arrangement concentrates the magnetic flux from two adjacent magnets into a single stator tooth, resulting in an air-gap flux density that exceeds the remanence of the magnets themselves. The generation of back-EMF and the torque is driven by the reversal of flux linkage polarity in the armature windings as the rotor moves. This process is best understood by analyzing the magnetic flux path at four distinct rotor positions over one electrical period, as illustrated in Figure 5.

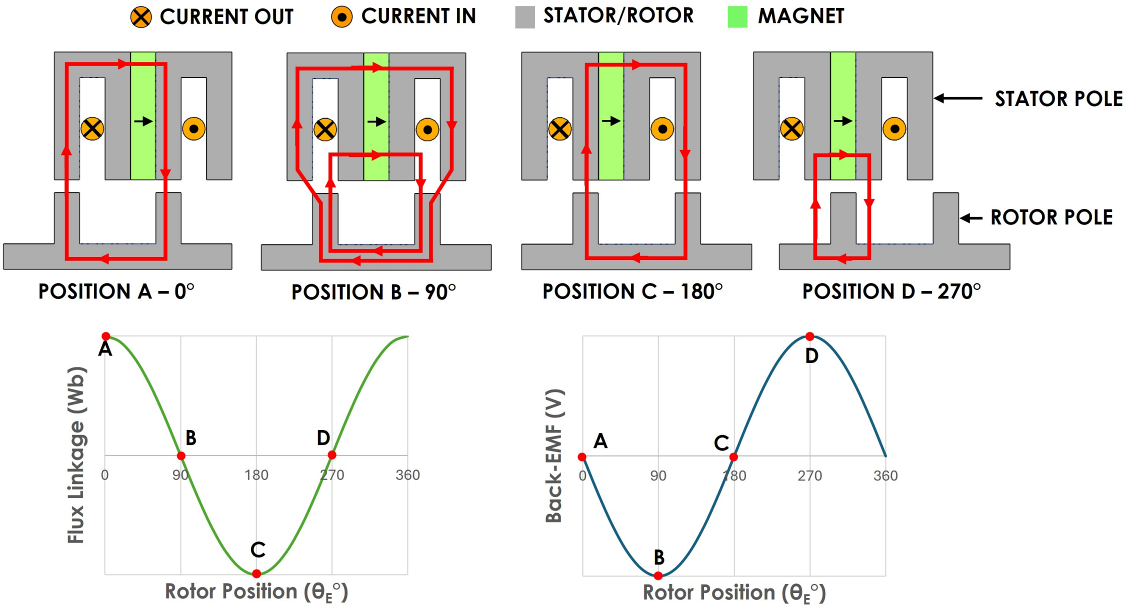

Figure 5: Illustration of the flux-switching principle

In the initial **position A**, a rotor pole is perfectly aligned with one of the stator teeth belonging to a U-shaped core. The magnetic flux generated by the adjacent permanent magnets is guided through the stator tooth, across the air gap into the rotor pole, and loops back into the adjacent stator unit. At that instant, the flux linkage in the armature coil wound around the stator tooth reaches its maximum positive flux linkage value as shown in the flux linkage versus rotor position plot in Figure 5 . As the rotation continues, the rotor pole moves away from the alignment with the stator tooth and enters the slot region between teeth as in **position B**. In this intermediate position, the magnetic circuit essentially short circuits or balances such that the net flux passing through the armature coil drops to zero. This point corresponds to the zero crossing of the flux linkage waveform. As the rotor rotates in the same direction, it aligns with the adjacent pole of the same U-shaped stator tooth as in **position C**. Since the magnet is alternatively polarized on this side, the flux achieves a peak in the opposite direction. Consequently, the flux linkage reaches its maximum negative value. Finally, the rotor moves past the stator pole and come in alignment with the magnet as in **position D**, and the flux linkage returns to zero before the cycle repeats. This continuous switching of flux polarity from positive to negative produces a bipolar flux linkage waveform. This is a critical distinction from the unipolar flux linkage found in conventional switched reluctance machines. Z. Q. Zhu et al. [17] studied that this bipolar capability allows the FSPM to utilize the full magnetic cycle, resulting in a sinusoidal back-EMF waveform.

Furthermore, the frequency of this flux switching is high; the electrical frequency (f) is proportional to the number of rotor poles (p) and the mechanical speed (N) in rpm, where (p) is equivalent to number of pole-pairs (P):

$$f = \frac{pN}{60}. \tag{1}$$

This relationship implies that FSPM machines operate at twice the electrical frequency than conventional machines for the same mechanical speed, necessitating careful consideration of iron losses in the stator laminations. However, the stationary location of the magnets offers a decisive thermal advantage; heat generated by the magnets due to eddy currents can be easily evacuated through the stator housing, preventing the risk of thermal demagnetization that plagues conventional interior permanent magnet (IPM) rotors.

1.3 Evolution of Flux Switching Machines

This section presents the evolution of FSMs, highlighting the key topologies and design improvements developed over time to enhance performance, torque density, and efficiency.

Doubly Salient Permanent Magnet (DSPM) Machines

In 1995, Y. Liao et al. [18] first introduced the DSPM machine built with the magnets placed in the stator yoke as shown in Figure 6, enabling high-speed capability of the rotors. The flux linkage in the coil is unipolar, and the motor operates on the flux switching principle. The rotor is a simple stack of laminated steel with no active components. As the rotor rotates, its poles align and unalign with the stator poles, modulating the flux path. The magnet arrangement allowed the concentration of flux into the air gap, resulting in high air-gap flux density. The interaction between the rotor and stator produces a trapezoidal back EMF. Consequently, the motor is electrically similar to a square wave BLDC motor and can be driven using 6-step commutation strategies.

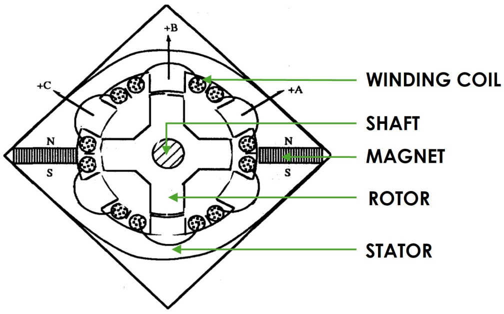

Figure 6: 2D cross-section of the DSPM machine [18]

Torque is produced primarily through the interaction of the stator current and the permanent magnet flux, rather than pure reluctance torque. This allows for a linear relationship between torque and current. Their study concluded that the DSPM machine achieved a higher torque-to-volume ratio than an equivalent induction motor. The prototype in their study offered high efficiency due to the use of high-energy magnets and the absence of rotor losses, as there are no rotor windings. The motor exhibits a high torque-to-current ratio and a low inertia, making it highly responsive for dynamic applications.

Flux Reversal Permanent Magnet (FRM) Machines

To address the unipolar flux linkage in the stator coils limiting the use of magnetic material and the high cogging torque of the DSPM machine. R. P. Deodhar et al. in 1997 [19] proposed FRM with a change in the magnet placement. The FRM machine retained the advantages of the DSPM machine such as robust rotor, high-speed capability, but the core innovation was the placement of the magnets. Instead of placing the magnets in the stator yoke, the magnets were placed on the stator tooth tips, creating a flux reversal mechanism that produces a bipolar flux linkage in this study. The FRM machine is also a doubly salient machine where the stator tooth tip carries 2 alternating pole magnets, e.g., a north pole on the right half and a south pole on the left half, as shown in Figure 7.

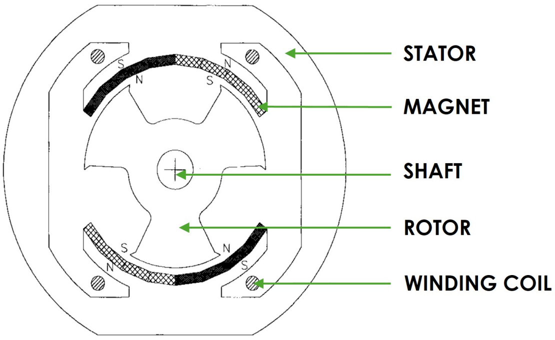

Figure 7: 2D cross-section of the FRM machine [19]

The rotor is a simple, robust stack of laminated steel with no windings or magnets, similar to an SRM machine. As the rotor pole rotates past a stator tooth, the magnetic flux linking the stator coil reverses polarity. When the rotor pole aligns with the north magnet, flux flows in one direction, and as it moves to align with the south magnet on the same tooth, the flux direction reverses. This natural reversal creates a bipolar variation of the flux linkage with rotor position, which is ideal for generating AC back EMF. This allows the FRM to be driven with AC drives or brushless DC controllers without the need for the specialized unipolar converters often required by SRM or early DSPM machines.

Their study concluded that sinusoidal bipolar flux linkage reduced the inductance variation compared to the DSPM machine. This leads to lower torque ripple and better compatibility with standard AC drive electronics. The phase inductance, being low and constant, improved the power factor and allowed for fast current control response. Like SRM machines, the phase windings are electrically isolated, offering good fault tolerance. Though this topology offers advantages over the DSPM machine, the placement of magnets on the tooth surface increases the risk of mechanical damage if the rotor were to rub against the stator. A significant amount of flux leaks between the adjacent magnets on the stator tooth without crossing the air gap to the rotor. This short-circuiting of flux reduces the effective torque density compared to the DSPM, where the magnets are in the yoke. Although better than DSPM, the FRM still exhibits notable cogging torque due to the slotting effect and the strong interaction between the surface magnets and rotor saliency.

Flux Switching Permanent Magnet (FSPM) Machines

While the foundational principles of flux switching were established in 1955, the topology remained largely impractical for high-performance industrial applications due to its single-phase nature and the limitations of early magnetic materials. The modern evolution of this machine, capable of competing with IPM machines, is bracketed by two seminal contributions: the introduction of the polyphase topology by Hoang et al. in 1997 [20] and the rigorous electromagnetic characterization and modeling by Z. Q. Zhu et al. in 2005 [21]. The 2D cross section of FSPM machines from Hoang's design and Z. Q. Zhu's design are shown in Figures 8 (left) and (right), respectively.

Hoang et al. introduced a novel stator structure that departed from the conventional distributed windings of AC induction motors. Their design featured a stator composed of elementary 'U-shaped' magnetic cores. The critical innovation was the placement of the permanent magnets. Instead of placing the magnets on the surface as in FRMs, Hoang et al. sandwiched the magnets between the U-shaped stator segments. This arrangement allowed two adjacent magnets to drive flux into a single stator tooth increasing the air-gap flux density. This study detailed the bipolar flux linkage principle in a polyphase context and distinguished the FSPM from the unipolar DSPM machine, theoretically allowing for a higher torque capability for the same volume of iron and copper. Z. Q. Zhu et al. presented a comprehensive analysis of the FSPM machine, validating its electromagnetic performance using a nonlinear adaptive lumped parameter magnetic circuit model. The study demonstrated that the FSPM topology achieves significantly higher torque density

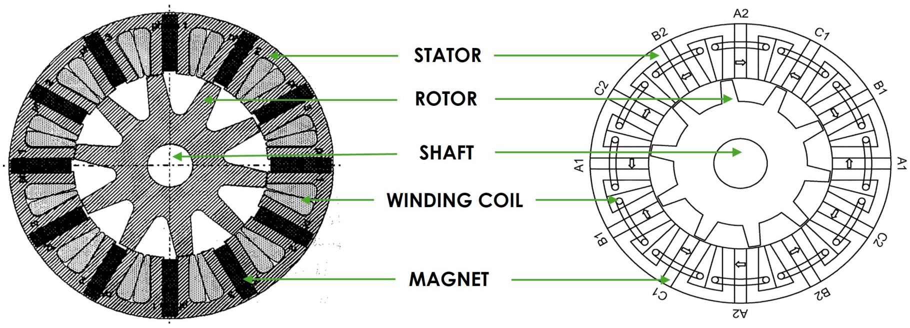

Figure 8: 2D cross-section of the FSPM machines - Hoang et al. design[20] (left) and Z. Q. Zhu et al. design [21] (right)

than conventional SPM machines [22] due to the flux focusing effect. Furthermore, the research confirmed that unlike other doubly salient machines, the FSPM produces an essentially sinusoidal back-EMF waveform and negligible cogging torque when the rotor pole width is optimized. The analysis also highlighted the machine's relatively high winding inductance, though it limits the rate of current rise, the study concluded it is highly advantageous for flux-weakening operation, enabling the machine to maintain constant power over wide speed range significantly beyond the base speed.

These three machines namely, DSPM, FRM and FSPM primarily differ in the magnets placement within the stator, which critically influences their electromagnetic performance. While all three machines share a salient rotor structure and concentrated windings, their torque production capability and flux interaction mechanisms vary. A comparative evaluation [23] shows that the FSPM machine exhibits the highest air-gap torque for the given machine volume among others, making it suitable for high torque density applications.

Multi-tooth Flux Switching Machines

Following the development of conventional FSPM machines, structural modifications are performed to enhance the torque density and to minimize the cogging torque. A significant advancement is the multi-tooth FSPM topology by Chen et al. in 2008 [24]. In the multi-tooth topology, a complex stator structure is introduced where each stator pole is split into multiple smaller teeth as shown in Figure 9. Their study focused on increasing the frequency of flux variation without increasing the mechanical speed, which allowed for an investigation of studies on 2, 4, and 6 teeth per stator pole. A significant 30% improvement in output torque was achieved in a design that used 4 teeth per pole compared to a conventional 12-slot/2-tooth-per-pole FSPM machine. Further studies involved reducing the permanent magnet usage while optimizing the stator core structure to enhance torque density.

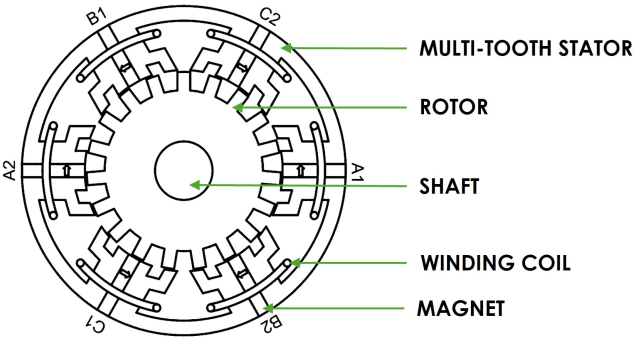

Figure 9: 2D cross-section of multi-tooth FSPM machine [24]

E-core and C-core Flux Switching Machines

E-core and C-core FSPM topologies were studied by Chen et al. [25], [26], which addressed the constraints of slot area and permanent magnet volume as shown in Figure 10 (left) and (right), respectively. These topologies were designed with significantly enlarged slot openings with wider slots to accommodate more armature winding, thereby increasing the electric loading capability. Also, these structures utilize only half the volume of permanent magnets compared to the conventional U-core design. The C-core topology was shown to achieve a torque density comparable to or higher than conventional designs, primarily due to the increased slot area compensating for the reduced magnet volume. Also, the E-core FSPM structure separates the phases physically and magnetically, which makes it easier to handle faults [27]. The alternate wound tooth structure makes the phases' self-inductance much higher while lowering the mutual inductance between them. This high self-inductance helps keep short-circuit currents low, which makes the machine naturally fault tolerant.

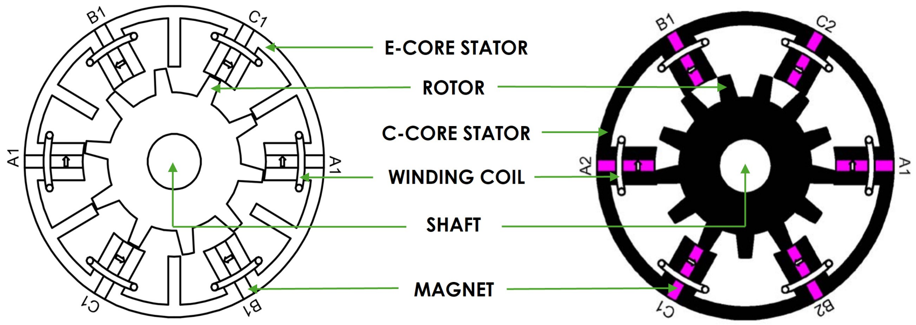

Figure 10: 2D cross-section of an E-core FSPM machine [25](left) and a C-core FSPM machine [26](right)

II-shaped and V-shaped Flux Switching Machines

While cost reduction can be achieved by minimizing permanent magnet volume within E-core and C-core topologies, researchers Fei et al. [28] and Y. J. Zhou et al. [29] studied II-shaped and V-shaped magnet arrangement in FSPM respectively, which increase the magnet volume to increase the flux focusing effect. Fei et al. study involved a 6-slot, 10-pole topology where, unlike conventional designs with single magnets, two parallel magnet pieces are embedded in each stator pole as shown in Figure 11 (left). With this configuration, a higher winding fill factor, higher torque density, and lower copper mass were achieved compared to a conventional 12-slot/10-pole structure.

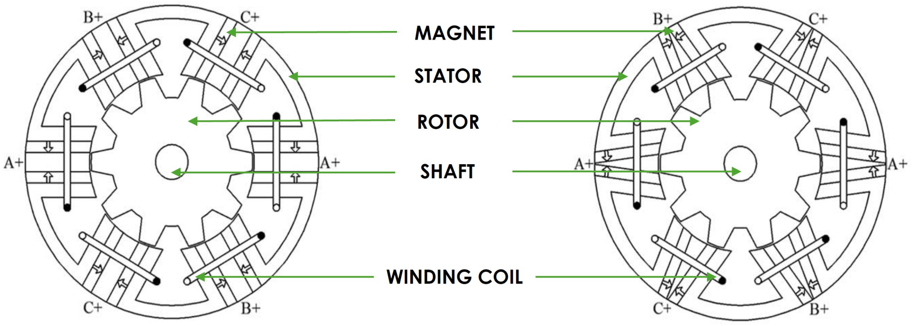

Figure 11: 2D cross-section of FSPM machine with II-shaped magnet arrangement (left) and V-shaped magnet arrangement [29] (right)

Building on this concept, Y. J. Zhou et al. proposed the V-shaped topology in their study in 2013 as shown in Figure 11 (right). Instead of simple parallel placement, this design inclines the two magnet pieces within each stator tooth to form a V-shape. This study found that this V-shaped arrangement significantly enhances the flux focusing effect, concentrating more flux into the air gap than parallel or single magnet designs leading to a 13.8% increase in output torque compared to the II-shaped arrangement.

Outer-Rotor Flux Switching Machines

While most FSPM topologies initially focused on inner rotor configurations, the specific requirements of in-wheel electric vehicle drives, namely high torque density and direct mechanical integration with the wheel, prompted the development of outer-rotor topologies. Weizhong Fei et al. [30] proposed a novel outer-rotor 12-slot, 22-pole FSPM machine built for light traction. This design features a stationary inner stator with the armature windings and permanent magnets surrounded by a robust passive outer rotor as shown in Figure 12. In this study, analytical sizing equations were derived and validated through finite element analysis (FEA), demonstrating that this outer-rotor configuration achieves higher torque density than comparable inner-rotor counterparts. A key finding was the machine's robust flux weakening capability. The research also highlighted that the 22-pole rotor was optimal for minimizing the cogging torque while maximizing back EMF symmetry.

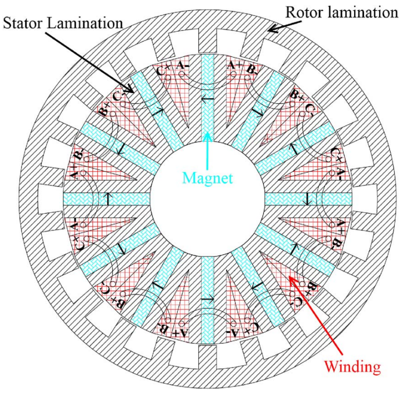

Figure 12: 2D cross-section of an outer-rotor FSPM machine [30]

Furthermore, in a subsequential study published in 2014 [31], the authors used frozen permeability method to rigorously decompose and analyses the machine's torque production. This study identifies that cogging torque is the dominant component of torque ripple in this topology rather than the interaction between armature and PM fields. Their analysis explicitly showed that magnetic saturation in the stator iron bridges significantly affects the inductance profiles and back EMF waveforms, leading to nonlinear torque behaviors under load. By comparing the results of 2D and 3D finite element analyses, the authors found that end effects reduce the average torque due to axial flux leakage.

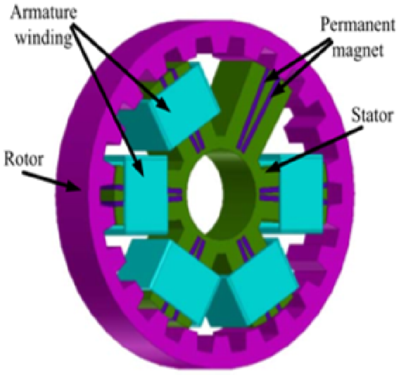

Figure 13: Outer-rotor FSPM machine with V-shaped magnet arrangement [32]

Further research on the outer-rotor topology by X. Zhu [32] led to the development of a V-shaped arrangement of magnets combining the advantages of the outer rotor with the superior flux focusing capabilities of V-shaped magnets as shown in Figure 13. The study conducted a multi-objective optimization where the initial design was established using analytical sizing equations in computing the electromagnetic performance. It is followed by sensitivity analysis, which is used to identify the most significant design parameters affecting torque and efficiency. Less influential variables were filtered ut using this process, thereby reducing the computational burden for subsequent optimization. The final level of this study involved multi-objective optimization, where a response surface methodology (RSM) combined with a genetic algorithm was used to find the optimal tradeoff between maximizing average torque while minimizing torque ripple. The findings from this study demonstrated that the optimized OR-VFSPM could achieve a significant reduction in cogging torque and torque ripple without compromising the high torque density inherent to the V-shaped magnet configuration.

1.4 Research Gap and Problem Statement

Research on FSPM Machines has largely concentrated on enhancing electromagnetic characteristics through topological alterations, including multi-tooth stators, V-shaped magnet configurations, and using different stator cores structures. Simultaneously, numerous investigations have examined the optimization of FSPM machines employing analytical techniques [33], parametric design optimizations [34], and metaheuristic algorithms like genetic algorithms [35], and response surface methods [36]. These studies primarily seek to improve torque density, efficiency, and torque ripple profiles through the systematic adjustment of geometric parameters and multi-objective optimization strategies [37]. Although these methodologies have yielded significant performance enhancements, they are formulated under idealized design scenarios characterized by considerable geometric flexibility, with comparatively limited consideration given to practical constraints such as mechanical integration, manufacturability and experimental validation. Although analytical sizing methods provide an initial framework for machine design, they are limited in capturing the highly nonlinear electromagnetic behavior inherent to doubly salient FSPM topologies. Effects such as localized magnetic saturation, complex flux paths, and torque ripple depend on geometric interactions requiring FEA-based optimization strategies to improve the prediction accuracy. However, FEA-based studies on such machines have limited focus on electromagnetic performance optimization with practical boundary conditions. Also in particular, only limited studies investigate the comparative effectiveness of different optimization approaches under constrained design spaces.

Research focused on electromagnetic optimization of an FSPM topology with electrical and thermal constraints are limited. In practical applications, considering the existing experimental test setup supply capabilities, the allowable electrical loading is restricted. In this thesis study, the current density is limited to 5 A/mm^2 to ensure thermal stability and prevent excessive copper losses and overheating during operation. Alongside this, the system is constrained by a DC voltage supply below 100 V and phase RMS current below 80 A, derived from the test bench available at Hybrid Electric Propulsion Cottbus (HepCO). These constraints significantly limit the ability to increase torque through electrical loading, thereby shifting the design challenge toward maximizing performance through geometric optimization of the magnetic circuit rather than increasing excitation. In addition to electrical constraints, the mechanical design is bounded by the requirement to integrate with components derived from the commercially available outer-runner Hacker Q150 motor. This imposes fixed constraints on the stator inner diameter and active stack length. The current density limit and adaptation of the Hacker Q150 geometry were defined through discussions with M.Eng. Enrico Teichert. Hence, this work adopts a constraint driven design approach, where the optimization will be performed with predefined mechanical and electrical boundaries. Consequently, the design space is significantly reduced, and the interaction between geometric variables becomes highly coupled.

Due to this strong parameter coupling, traditional one variable at a time optimization approach are inadequate for identifying optimal solutions. Key design parameters including stator pole arc, rotor pole arc, magnet arc and yoke dimensions, influence each other in a non-linear manner. Therefore, a multi-objective optimization framework is required to simultaneously maximize average torque and efficiency while minimizing torque ripple within the imposed electrical and mechanical constraints. Although multi-objective optimization techniques such as Pareto-based evolutionary algorithms (EAs) are widely reported in the literature, there remains limited understanding of their comparative effectiveness when integrated with FEA under realistic constraints.

To address these limitations, this thesis is structured as a sequence of interrelated steps. The study begins with a detailed review of flux-switching machines, focusing on their operating principles and sizing approaches. Subsequently, an automated simulation framework is developed to enable efficient parametric modeling and optimization. Based on this framework, the FSPM machine is designed and sized using the reference geometry of the Hacker Q150 motor, with the objective of maximizing torque and efficiency while minimizing torque ripple under the defined constraints. This study integrates FEA with multiple optimization approaches, including Parametric Sweep Optimization, Direct Optimization, and Meta-Model-Based Optimization, within a constrained design space. In addition, a comparative evaluation of two-dimensional and three-dimensional FEA is carried out. The work further extends toward practical realization through the development of a manufacturable CAD model and preparation of technical drawings. A prototype mock-up is also considered to evaluate manufacturability, assembly challenges, and potential failure modes.

The selection of the FSPM topology and the use of optimization strategies were initially suggested by M.Eng. Enrico Teichert, during early discussions. The incorporation of Failure Mode and Effects Analysis (FMEA) was later proposed by Dr.-Ing. Stefan Kazula, leading to the workshop presented in this thesis. While these suggestions guided the research direction, all detailed implementation, analysis and development were carried out independently by the author.

1.5 Thesis Outline

This thesis work is split into eight chapters, including the Introduction and Literature Review. A brief overview of the remaining chapters is provided below:

- **Chapter 2:** Develops the analytical foundation for the base model. The machine geometry is derived using established sizing equations, and a fully parameterized geometric model is developed for further optimization.
- **Chapter 3:** Describes the implementation and analysis of the machine in ANSYS Maxwell. Both magnetostatic and transient analyses are conducted to evaluate performance, including torque and inductance characteristics.
- **Chapter 4:** Presents the core contribution of the thesis by applying and comparing multiple optimization strategies.
- **Chapter 5:** Extends from improved 2D design to 3D model to evaluate end effects, axial flux leakage, and overall performance.
- **Chapter 6:** The optimized electromagnetic design is translated into a manufacturable prototype. This includes mechanical assembly design, integration with existing motor components, and preparation of technical drawings.
- **Chapter 7:** Addresses FMEA and includes a technical workshop to identify and discuss potential failure modes across electromagnetic, mechanical, and manufacturing domains.
- **Chapter 8:** Concludes the thesis and outlines directions for future work as an extension of the current study.

2 Machine Sizing

This chapter deals with analytically sizing the 2D base model geometry for the outer-rotor FSPM following the geometric relations in [30] by Weizhong Fei et al. Though [38] was the first study published by Weizhong Fei et al. on the outer-rotor FSPM topology, the design in this study was based on an analytical approach to address the electromagnetic design issues with no experimental validation. Whereas in [30], the authors conducted experiments on the prototype machine and found reasonable agreements with the predicted results from FEA. This confirmed the machine's suitability for the proposed application, owing to its relatively high efficiency and flux-weakening capability over the operational speed range. The analytical sizing equations based on [30] are derived to determine the main design parameters of the base model for this thesis study.

2.1 Slot and Pole Configuration

The FSPM machine is distinguished from conventional topologies by housing all active excitation sources on the stator. In this thesis study, the baseline design developed has each stator pole constructed from two laminated iron teeth that sandwich a rectangular permanent magnet similar to the configuration proposed in [30]. However, small iron bridges are incorporated at the radial ends of the magnets slot to enable manufacturing of the stator as a single integrated piece. These stator poles are circumscribed by fractional slot concentrated armature windings. This design choice was established following discussions between the author and M.Eng. Enrico Teichert. The selection of stator and rotor pole combinations is subject to electromagnetic constraints to ensure balanced multi-phase operation. According to [30], the number of stator slots N_s must be a multiple of the number of phases m. Furthermore, N_s must be an even integer to accommodate the alternating face-to-face magnetization polarities of the PMs in adjacent stator poles. For any three-phase machine ($m = 3$), the stator pole count is inherently restricted to multiples of six. For an outer-rotor FSPM topology, the feasible number of rotor poles N_r is dictated by the relationship from [30],

$$N_\mathrm{r} = \frac{(12 \pm n)N_\mathrm{s}}{6}, \tag{2}$$

where n is a positive integer that is not a multiple of three. It is preferable that N_r remains an even number. An even rotor pole count guarantees a symmetrical spatial distribution of the flux density in the air gap, which nullifies the resultant radial magnetic forces. From a mechanical standpoint, avoiding unbalanced magnetic pull is crucial. If left unaddressed, this imbalance causes asymmetric bearing loads, increases acoustic noise, and degrades the machine's structural integrity. Driven by these dual electrical and mechanical requirements and based on the study results from [30], a 12-slots/14-poles configuration is adopted for this study, following discussion between the author and M.Eng. Enrico Teichert.

2.2 Mechanical Constraints and Boundary Dimensions

The dimensional sizing of the baseline machine is bounded by the physical constraints of the Hacker Q150 motor. Mechanical integration requirements defined the baseline dimensions, locking the shaft diameter at 100 mm and restricting the active stack length to 25 mm.

$$\mathrm{ORD} = \left(\frac{7}{6} + \frac{\pi}{2N_\mathrm{s}}\right)\mathrm{OSD} + \mathrm{AG}, \tag{3}$$

Although the preliminary sizing equation (3) from [30] yielded an optimal outer-rotor diameter of 188 mm, this dimension had to be adjusted for the experimental test setup. Specifically, the machine must be mounted with a horizontal shaft axis during testing. To prevent any physical interface between the rotating housing and the stationary testbed surface, the absolute maximum permissible oute-rotor diameter is capped to 186 mm as it guarantees safe operational testing.

2.3 Geometric Parameterization and Dimensionless Ratios

Establishing a robust 2D geometric model is a prerequisite for systematically evaluating the electromagnetic performance and executing subsequent parametric optimizations. Utilizing a fully parametric approach defined by fundamental angular pitches, specific component arcs, and dimensionless ratios allows the machine's geometry to scale proportionally during the iterative FEA sweeps. This mathematical framework prevents simulation boundary violations such as overlapping geometry or the generation of non-physical structural dimensions. Figure 14 shows the base model design with geometric parameters.

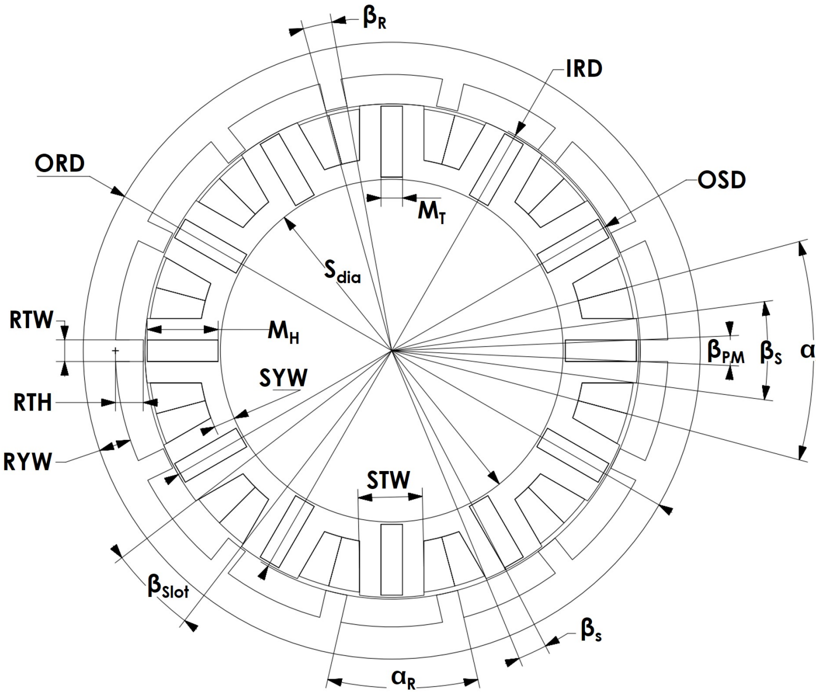

Figure 14: Geometric parameters and dimensionless ratios in the 2D base model

2.3.1 Fundamental Angular Pitches

Fundamental angular pitches reflect the structural repetition of the machine, which is inherently dictated by the fixed number of stator and rotor poles. The fundamental pitches define the exact angular sectors required to capture one complete, repeating unit of the active magnetic circuit. The stator pole pitch α_S is mathematically defined as the full circumference divided by the total number of stator slots N_s, expressed by,

$$\alpha_\mathrm{S} = \frac{360^\circ}{N_\mathrm{s}}. \tag{4}$$

For the selected design utilizing 12 stator poles, the fundamental stator pitch is 30°. This 30° angular sector marks the strict spatial footprint for one complete stator section. Physically, a single stator pole pitch encapsulates one complete stator pole assembly comprising two separate laminated iron teeth and one sandwiched permanent magnet alongside one adjacent armature winding slot. This pitch serves as the master spatial boundary for all subsequent stator-side geometric parameter deviations.

The rotor pole pitch α_{R} is determined by dividing the total circumference by the chosen number of rotor poles N_{r}, expressed by,

$$\alpha_{\mathrm{R}} = \frac{360^\circ}{N_{\mathrm{r}}}. \tag{5}$$

For the established 14-rotor-pole configuration, this parameter equates to ∼25.7°. This angle governs the spatial period of the rotor's geometric saliency. A complete rotor pitch encompasses exactly one salient rotor iron tooth and one adjacent open rotor slot. The dimension of the rotor pole pitch directly dictates the fundamental electrical frequency of the induced back-EMF during the flux-switching process.

2.3.2 Component Arc Dimensions and Geometric Deviation

To formulate a balanced initial baseline geometry, the 30° fundamental stator pole pitch is analytically divided between its active solid components and the open winding slot. A critical geometric distinction is maintained between the individual stator tooth arc β_{s} and the total stator pole arc β_{S}. The total stator pole arc represents the entirety of the solid magnetic material situated on the stator per pitch, which is the combination of the two iron teeth and the central magnet. It can be calculated by,

$$\beta_{\mathrm{S}} = 2\beta_{\mathrm{s}} + \beta_{\mathrm{PM}}. \tag{6}$$

The spatial equation governing the entirety of one complete stator pitch requires the summation of its physical parts which includes two individual stator teeth, one permanent magnet, and one slot, given by,

$$2\beta_{\mathrm{s}} + \beta_{\mathrm{PM}} + \beta_{\mathrm{Slot}} = \alpha_{\mathrm{S}}. \tag{7}$$

For this initial outer-rotor design, the individual stator tooth arc β_{s}, the permanent magnet arc β_{PM}, and the rotor tooth arc β_{R} are intentionally constrained to be exactly one-third of the total stator pole arc β_{S}, as followed in [30]. This initialization maximizes the available area for the armature windings while maintaining symmetric magnetic flux paths. This mathematical constraint is expressed as,

$$\beta_{\mathrm{s}} = \beta_{\mathrm{PM}} = \beta_{\mathrm{R}} = \frac{\beta_{\mathrm{S}}}{3} = \frac{\pi}{3N_{\mathrm{s}}}. \tag{8}$$

Solving equations (7) and (8), the individual component arcs for the baseline design are sized as shown in Table 1.

Table 1: Component arc dimensions of the 2D base model

Component	**Arc Angle**
β_{s}	5°
β_{PM}	5°
β_{R}	5°
β_{Slot}	15°

This specific geometric derivation analytically verifies that the 30° stator pole pitch is split with symmetry into exactly 15° of core material with solid magnets and 15° of open winding slot area.

2.3.3 Linear Widths and Trigonometric Projections

To transition from angular arcs to finalized 2D structural cross-section ready for automated multi-objective optimization, the angular dimensions are converted into explicit physical linear widths. The linear stator tooth width STW is the physical width of a single stator pole, derived via a direct trigonometric projection. The mathematical formulation is given by,

$$\mathrm{STW} = \mathrm{OSD}\sin\left(\frac{\beta_{\mathrm{S}}}{2}\right). \tag{9}$$

The explicit thickness of the rectangular permanent magnet M_{T} utilizes the identical trigonometric projection logic applied to the magnet's designated arc, given by,

$$M_{\mathrm{T}} = \mathrm{OSD}\sin\left(\frac{\beta_{\mathrm{PM}}}{2}\right). \tag{10}$$

Unlike the stator components, the physical width of the salient rotor pole RTW is calculated directly at the inner diameter of the outer rotor, given by,

$$\mathrm{RTW} = \mathrm{IRD}\sin\left(\frac{\beta_{\mathrm{R}}}{2}\right). \tag{11}$$

2.3.4 Dimensionless Optimization Coefficients and Yoke Sizing

To finalize the geometric parameterization of the machine, specific dimensionless optimization coefficients such as γ_{S} and γ_{R} are defined. These coefficients establish proportional sizing for the stator and rotor yokes directly from the calculated linear component widths. The stator yoke thickness ratio coefficient γ_{S} dictates the proportional sizing of the stator yoke. It is initialized at a baseline value of 1/3. The physical dimension of the stator yoke width is defined as a mathematical fraction of the linear stator tooth width, given by the expression:

$$\mathrm{SYW} = \gamma_{\mathrm{S}}\mathrm{STW}. \tag{12}$$

This specific fraction of 0.333 ensures the stator back iron provides the necessary magnetic return capacity to prevent severe saturation, without unnecessarily increasing the static core mass of the machine.

The rotor yoke thickness ratio γ_{R} parameter defines the proportional sizing of the active rotor yoke. Instead of scaling the rotor tooth, the rotor yoke thickness ratio scales the rotor yoke width directly from the computed stator yoke dimensions, adhering to relations from [30]. The coefficient is initialized at a fixed multiplier of 1.5. The exact physical dimension of the rotor yoke width is defined mathematically as,

$$\mathrm{RYW} = \gamma_{\mathrm{R}}\mathrm{SYW}. \tag{13}$$

Maintaining this 1.5 multiplicative ratio over the stator yoke width serves a dual engineering purpose in an outer-rotor topology. It absorbs vibrations in the rotor while simultaneously providing a robust magnetic flux return path.

2.4 Phase Winding Resistance Calculation

To compute the copper losses and the efficiency of the machine, the phase resistance must be calculated using the physical dimensions of the phase winding during optimization. The analytical model first determines the Mean Length of a Turn MLT, by evaluating the physical arc length of the end windings. MLT is calculated by finding the mean coil pitch angle θ_{pitch}, geometric mean radius R_{mean} and the effective coil overhang diameter S. Figure 15 shows the graphical cut section of the base model representing the winding parameters used for calculating the phase resistance of the windings.

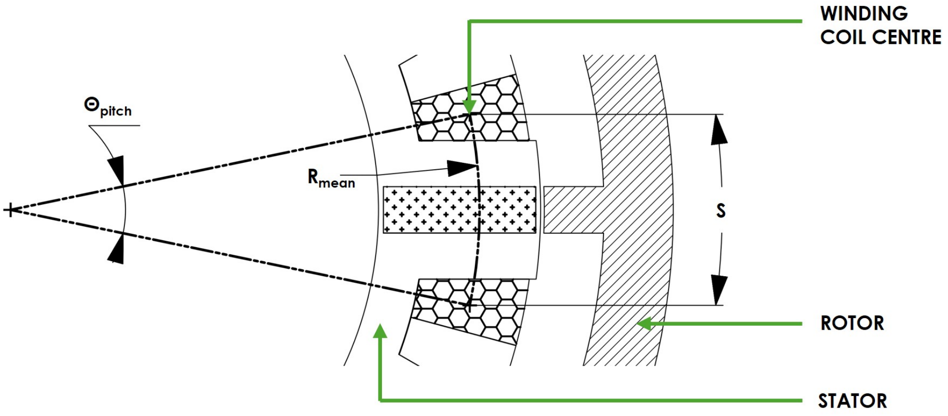

Figure 15: Visual representation of winding parameters

The mean coil pitch angle θ_{pitch} is determined by,

$$\theta_{\text{pitch}} = \frac{\alpha_{\text{S}} + \beta_{\text{S}}}{2}. \tag{14}$$

The geometric mean radius R_{mean} is determined by,

$$R_{\text{mean}} = \left(\frac{S_{\text{dia}}}{2} + \text{SYW}\right) + \frac{\left(\frac{\text{IRD}}{2} - \text{AG} - hs_0\right) - \left(\frac{S_{\text{dia}}}{2} + \text{SYW}\right)}{2}. \tag{15}$$

The effective coil overhang diameter S is,

$$S = R_{\text{mean}} \left(\theta_{\text{pitch}} \frac{\pi}{180}\right). \tag{16}$$

The Mean Length of a Turn (MLT) is,

$$\text{MLT} = 2L_{\text{active}} + \pi S. \tag{17}$$

With the MLT determined, the framework computes the final electrical phase resistance by accounting for the thermal conditions. The temperature-dependent copper resistivity ρ_{Cu} is adjusted for specific ambient T_{amb} and operational temperature rise T_{rise} and calculated as,

$$\rho_{\text{Cu}} = \rho_{20} \left[1 + \alpha_{20}(T_{\text{amb}} + T_{\text{rise}} - 20)\right]. \tag{18}$$

The electrical resistance of a single concentrated coil R_{coil} is,

$$R_{\text{coil}} = \frac{n \rho_{\text{Cu}} \text{MLT}}{A_{\text{cond}} \text{Strands}}. \tag{19}$$

The total equivalent phase resistance R_{phase} calculated from the individual coil resistance is,

$$R_{\text{phase}} = \left(\frac{N_{\text{s}}}{m}\right) R_{\text{coil}} \left(\frac{1}{N_{\text{pph}}^2}\right). \tag{20}$$

Based on the geometrical constraints and sizing ratios established in this chapter, the total available winding area per slot for the base 2D model is computed to be 106.5 mm^2. By selecting an appropriate combination of wire diameter, number of parallel paths, number of turns, and number of strands to achieve a fill factor close to 50%, the design results in 10 turns with 2 parallel strands. The bare conductor diameter of SWG 15 is 1.829 mm, which increases to 1.9025 mm with insulation, resulting in an effective fill factor of approximately 53%. Assuming an ambient temperature of 40°C and an operational temperature rise of 60°C, the resulting phase resistance is calculated to be approximately 21.6 mΩ for the 2D base model design.

A summary of the Machine Sizing design parameter values are shown in Tables 2 & 3.

Table 2: Base model design parameters - mechanical and geometrical

Parameter	**Value**
α_{S}	30°
α_{R}	~25.7°
β_{S}	15°
β_{PM}	5°
β_{s}	5°
β_{R}	5°
β_{Slot}	15°
γ_{S}	1/3
γ_{R}	0.5
S_{dia}	100 mm
OSD	144 mm
AG	0.5 mm

Parameter	**Value**
IRD	145 mm
ORD	180 mm
L_{active}	25 mm
M_{T}	~6.3 mm
M_{H}	~20.7 mm
SYW	~6.3 mm
STW	~6.3 mm
STH	~18.8 mm
RYW	~9.4 mm
RTW	~6.3 mm
RTH	~8.1 mm

Table 3: Base model design parameters - electrical

Parameter	**Value**
No. of Phases (m)	3
No. of Stator Poles (N_{s})	12
No. of Rotor Poles (N_{r})	14
No. of Coil Turns (n)	10
No. of strands (Strands)	2
Parallel paths Number (N_{pph})	1
Winding Slot Fill Factor	~53%
Current Density (J_{max})	5 A/mm^2
Rated Speed (N)	2500 rpm
DC Voltage Limit (V_{DC})	100 V
Phase RMS current Limit ($I_{\mathrm{phase,rms}}$)	80A

3 2D Electromagnetic Modeling and Analysis

Engineering problems involving complex geometries and non-linear materials rarely possess accurate analytical solutions, as the analytical methods rely on simplified mathematical models. Experimental methods are helpful but are often cost-intensive to utilize at the initial design stage, particularly when testing multiple design iterations or materials is required. One suitable solution is to use numerical methods, which address the limitations of analytical and experimental methods. Numerical methods provide approximate yet highly accurate solutions by breaking down continuous physical domains into discrete computable segments. There are several different numerical methods that are prevalently used, each suited to a specific physical phenomenon. The Finite Difference Method (FDM) is one of the oldest numerical methods, most suitable for solving differential equations by approximating derivatives with finite differences over structured grids [39]. The Finite Volume Method (FVM) is suitable for solving problems involving fluids and is used largely in fluid dynamics [40]. This method calculates the flux of the conserved quantities across the boundaries of small control volumes. The Boundary Element Method (BEM) simplifies calculation by discretizing only the boundary of the domain rather than discretizing the entire domain [41]. This advantage makes this BEM method highly efficient for infinite space problems like acoustics. The Method of Moments (MOM) is predominantly used in high-frequency electromagnetics for analyzing wire antennas and scattering problems [42].

Finite Element Method (FEM) is the most predominant industry standard for designing electric machines [43]. Electric motors have complex structures, featuring different stator slot geometries, narrow air gaps, and highly non-linear magnetic materials like electrical steel lamination used in the stator and rotor core. With the help of FEM, these geometric complexities can be handled through adaptive meshing and accurately computes magnetic saturation, eddy currents, and localized flux densities.

3.1 Governing Maxwell Equations

In electromagnetic design, the core behavior of a motor is universally governed by Maxwell's equations [44]. These four fundamental equations describe how electric and magnetic fields are generated and undergo change under each other's influence as well as by the charges and currents. The complete set in differential form are as follows:

Gauss's Law for Electricity

$$\nabla \cdot \mathbf{D} = \rho, \tag{21}$$

where

$$\mathbf{D} = \epsilon \mathbf{E}. \tag{22}$$

This law states that the electric flux through a surface depends on the enclosed charge. In other words, it relates the electric displacement field $\mathbf{D}$ to the free charge density ρ. The electric field displacement is further defined by the relation (22), where ϵ represents permittivity of the material and $\mathbf{E}$ represents electric field intensity.

Gauss's Law for Magnetism

$$\nabla \cdot \mathbf{B} = 0 \tag{23}$$

This law dictates that there are no magnetic monopoles; that is, the divergence of the magnetic flux density $\mathbf{B}$ is always 0. In other words, magnetic field lines never begin or end, they always form loops.

Faraday's Law of Electromagnetic Induction

$$\nabla \times \mathbf{E} = -\frac{\partial \mathbf{B}}{\partial t} \tag{24}$$

It describes the fundamental principle of voltage generation. It mathematically tells how a time-varying magnetic field $\frac{\partial \mathbf{B}}{\partial t}$ creates an electromotive force or an electric field $\mathbf{E}$. In other words, changing magnetic fields create an electric field (induced voltage).

Ampere Maxwell Law

$$\nabla \times \mathbf{H} = \mathbf{J} + \frac{\partial \mathbf{D}}{\partial t} \tag{25}$$

This law relates magnetic field intensity $\mathbf{H}$ to the electric current density $\mathbf{J}$ and the time-varying electric field $\frac{\partial \mathbf{D}}{\partial t}$. In other words, electric currents and changing electric fields generate magnetic fields.

For standard electric machines operating at low frequencies, the displacement current term is negligible compared to the conduction current. Therefore, the equation simplifies to the quasistatic form given as,

$$\nabla \times \mathbf{H} = \mathbf{J}. \tag{26}$$

From the equation $\nabla \cdot \mathbf{B} = 0$, the magnetic flux density $\mathbf{B}$ has 0 divergence. A vector field with 0 divergence can be expressed as the curl of another vector field. Therefore, $\mathbf{B}$ can be represented in terms of the magnetic vector potential $\mathbf{A}$, which can be expressed as,

$$\mathbf{B} = \nabla \times \mathbf{A}. \tag{27}$$

Assuming an isotropic material, the constitutive relation between $\mathbf{B}$ and $\mathbf{H}$ is

$$\mathbf{H} = \nu \mathbf{B} = \frac{1}{\mu}\mathbf{B}. \tag{28}$$

In electrical steel, the magnetic permeability μ is highly nonlinear and depends on the magnetic flux density $\mathbf{B}$.

Substituting the relations $\mathbf{B} = \nabla \times \mathbf{A}$ and $\mathbf{H} = \nu \mathbf{B}$ into the simplified equation (26) yields,

$$\nabla \times (\nu \nabla \times \mathbf{A}) = \mathbf{J}. \tag{29}$$

An equivalent form is,

$$\nabla \times \left(\frac{1}{\mu} \nabla \times \mathbf{A} \right) = \mathbf{J}. \tag{30}$$

This partial differential equation forms the basis of magnetostatic finite element formulations. FEM takes this continuous differential equation and solves it by discretizing the motor's geometry.

Deconstructing the Finite Element Method

The finite element method functions by transforming a continuous physical problem into a larger system of algebraic equations that a computer can solve. The process begins with discretization, commonly known as meshing. The entire geometry of the motor, including the stator, rotor, coil windings, magnets and the surrounding air, is divided into small simple geometric shapes called finite elements, which are typically triangles in 2D or tetrahedra in 3D. Once the meshing is done, the continuous magnetic vector potential **A** within any single element is approximated using the shape functions, $N_i(x, y)$. These interpolation polynomials define how the field varies between the discrete nodes of the element. Rather than calculating an infinite number of points, the solver only determines the values at the nodes. The potential at any point within an element is the sum of the nodal values weighted by their respective shape functions.

$$A(x, y) \approx \sum_{i=1}^{n} N_i(x, y) A_i. \tag{31}$$

The important feature of this method lies in the stiffness matrix created. For each separate element, a local matrix is formed based on the material properties and the shape functions. These local matrices are systematically assembled into a massive global stiffness matrix representing the entire machine. By applying boundary conditions, the solver evaluates the global system of linear equations.

$$[\mathbf{K}]\{\mathbf{A}\} = \{\mathbf{F}\}. \tag{32}$$

In this system, $[\mathbf{K}]$ is the global stiffness matrix or reluctance matrix, $\{\mathbf{A}\}$ is the column vector of unknown magnetic potentials at every node, and $\{\mathbf{F}\}$ represents the source vector containing the excitation from currents or permanent magnets.

3.2 Motor Control Methods

After constructing the 2D base model design, an external circuit representing a controller with an inverter involving a specialized control scheme is required to run the designed machine. The choice of control method heavily depends on the motor type and the machine's dynamic requirements.

The 6-step control method is the industry standard for trapezoidal Brushless Direct Current (BLDC) drives. It is not a continuous but a discrete process where the inverter steps through six specific switching intervals per electrical revolution. Based on the feedback from three Hall effect sensors placed inside the machine, only two of the three motor phases are energized at any given time. This creates a rotating magnetic field in 60-degree increments, pulling the rotor along. While simple and effective for applications like fans and pumps, the commutation transitions cause noticeable torque ripple.

Field-oriented control (FOC) adopts a different mathematical approach and is primarily used for PMSM drives. Controlling three distinct, continuously varying AC currents is not easy as compared to the 6-step BLDC control. In FOC, this is simplified by transforming the stationary three-phase system into a rotating two-coordinate system, effectively making the AC motor behave mathematically like a separately excited DC motor where flux and torque can be controlled independently. This decoupling relies on two crucial mathematical transformations, namely the Clarke and the Park transforms. The Clarke transform takes the three-phase stationary reference frame currents and projects them onto a two-axis orthogonal stationary reference frame denoted by α and β. Figure 16 shows all three reference axes.

Assuming a balanced system where $I_a + I_b + I_c = 0$, the matrix equation expressing α and β

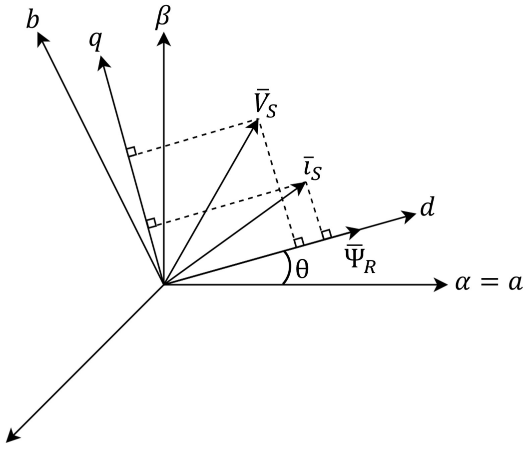

Figure 16: Current, voltage, and rotor flux space vectors in all three reference frames [45]

currents is given by,

$$\begin{bmatrix} I_\alpha \\ I_\beta \end{bmatrix} = \frac{2}{3} \begin{bmatrix} 1 & \frac{-1}{2} & \frac{-1}{2} \\ 0 & \frac{\sqrt{3}}{2} & \frac{-\sqrt{3}}{2} \end{bmatrix} \begin{bmatrix} I_a \\ I_b \\ I_c \end{bmatrix}. \tag{33}$$

Next, the Park transform takes these stationary α and β components and projects them onto a reference frame spinning in synchronization with the rotor at the electrical angle θ. This defines the direct d and the quadrature q axes currents given by,

$$\begin{bmatrix} I_d \\ I_q \end{bmatrix} = \begin{bmatrix} \cos\theta & \sin\theta \\ -\sin\theta & \cos\theta \end{bmatrix} \begin{bmatrix} I_\alpha \\ I_\beta \end{bmatrix}. \tag{34}$$

The peak phase current and voltage values from the d-q reference frame can be obtained as,

$$I_{\text{peak}} = \sqrt{I_d^2 + I_q^2}, \tag{35}$$

$$V_{\text{peak}} = \sqrt{V_d^2 + V_q^2}. \tag{36}$$

Similarly, the d and q axis currents in terms of phase RMS current can be expressed as,

$$I_d = \sqrt{2} I_{\text{rms}} \cos\beta, \tag{37}$$

$$I_q = \sqrt{2} I_{\text{rms}} \sin\beta. \tag{38}$$

In steady state, the sinusoidal AC currents appear as flat DC values in this d-q frame. The d-q equivalent electromagnetic torque T_e, flux linkages and voltages of the machine can then be expressed as,

$$T_e = \frac{3}{2} P(\lambda_m I_q + (L_d - L_q) I_d I_q), \tag{39}$$

$$\begin{bmatrix}\lambda_d \\ \lambda_q\end{bmatrix} = \begin{bmatrix}L_d & 0 \\ 0 & L_q\end{bmatrix}\begin{bmatrix}I_d \\ I_q\end{bmatrix} + \begin{bmatrix}\lambda_m \\ 0\end{bmatrix}, \tag{40}$$

$$\begin{bmatrix}V_d \\ V_q\end{bmatrix} = \begin{bmatrix}R_{\text{phase}} & -\omega_e L_q \\ \omega_e L_d & R_{\text{phase}}\end{bmatrix}\begin{bmatrix}I_d \\ I_q\end{bmatrix} + \begin{bmatrix}0 \\ \omega_e \lambda_m\end{bmatrix}. \tag{41}$$

For a surface-mounted PMSM where $L_d \approx L_q$, the reluctance torque term disappears, and torque becomes directly proportional to the q-axis current. The control algorithm forces the d-axis current to zero ($I_d = 0$) to avoid wasting energy against the permanent magnets, directing all current into the q-axis to maximize the torque production which is purely electromagnetic. In this case, Equation (39) becomes,

$$T_e = \frac{3}{2} P \lambda_m I_q. \tag{42}$$

Since the back-EMF waveform of FSM is sinusoidal [21], the FOC control algorithm can be used to run the machine designed in this thesis.

3.3 PWM Switching Techniques

Modern inverters act as the bridge between a DC power source and the AC motor, using the Pulse Width Modulation (PWM) to synthesize the sinusoidal voltages. Like different control methods exist, there are also many switching methods for inverter operation.

In sine PWM (SPWM), a high-frequency triangular carrier wave is continuously compared against a fundamental sinusoidal reference wave. When the sine wave is higher than the triangular wave, the upper switch of an inverter leg turns on, supplying the motor phase with positive voltage. When the sine wave is lower than the triangular wave, the upper switch turns off and the bottom switch turns on, supplying the motor phase with negative voltage. Figure 17 shows the typical sine PWM switching operation with carrier wave, sinusoidal reference wave, and the generated PWM pulse.

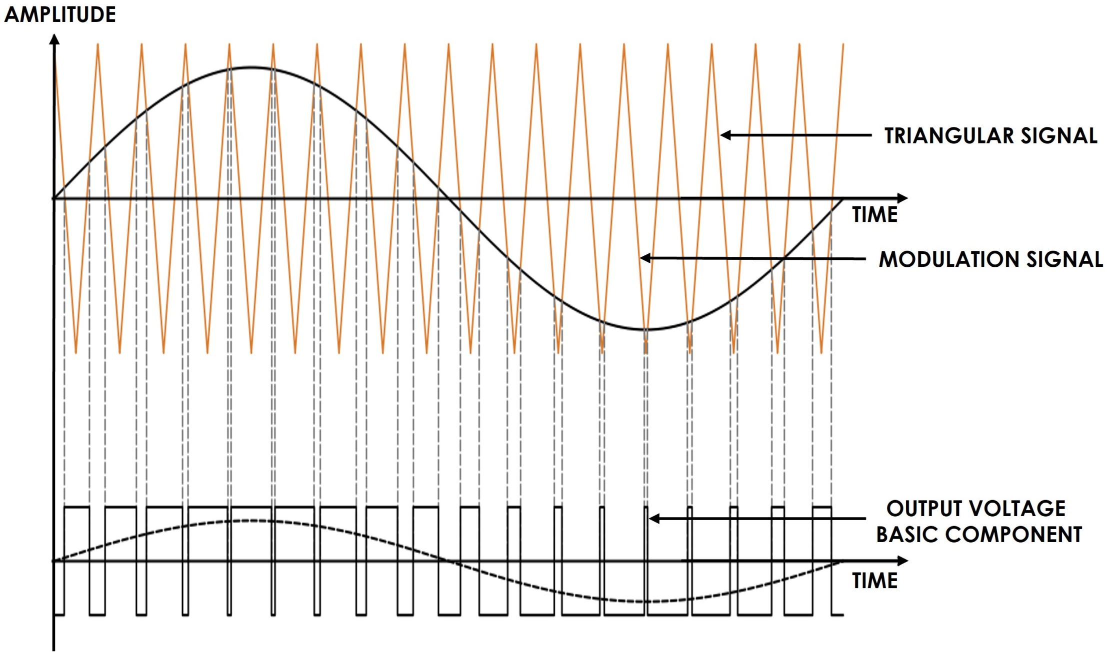

Figure 17: Sinusoidal PWM using triangular carrier and reference signal [46]

Space Vector PWM (SVPWM) is a more advanced approach. Instead of treating three motor phases separately, SVPWM treats the inverter as a single cohesive unit. The three-phase voltages are transformed into a single rotating space vector $\mathbf{V}_s$ on the complex plane using the following mathematical relationship:

$$\mathbf{V}_s = \frac{2}{3}\left(V_a + V_b \cdot e^{j\frac{2\pi}{3}} + V_c \cdot e^{j\frac{4\pi}{3}}\right) \tag{43}$$

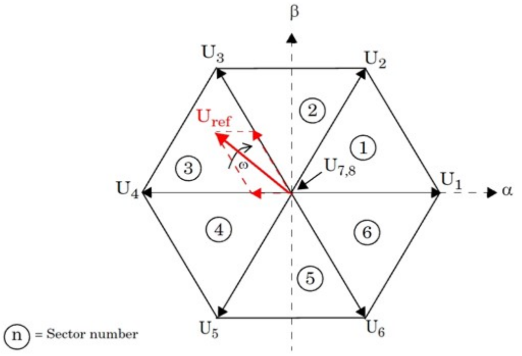

Figure 18: Space vector diagram of SVPWM showing voltage vectors and sector division [47]

Vector	Q1	Q2	Q3
U1	1	0	0
U2	1	1	0
U3	0	1	0
U4	0	1	1
U5	0	0	1
U6	1	0	1
U7	0	0	0
U8	1	1	1

Table 4: SVPWM switching states

This equation generates a hexagon with eight possible switching states, as shown in Figure 18, comprising six active vectors (U1, U2, U3, U4, U5, U6) and two zero vectors (U7, U8). Table 4 shows the 8 possible switching states across three phases. By calculating the precise time durations to dwell on adjacent active vectors and zero vectors, SVPWM constructs a smoothly rotating reference voltage vector U_{ref}. This method is preferred in modern drives because it utilizes DC bus voltage more efficiently than SPWM and inherently reduces harmonic distortion.

3.4 Methodology Justification: Sizing Versus Control Dynamics

It is essential to define the parameters separating the electromagnetic machine design from the dynamic control simulation, while recognizing that both domains inherently influence each other in a complete drive system. Sophisticated control strategies like FOC and SVPWM are mandatory for assessing the transient response, and drive cycle efficiency of the finished system, however, they introduce computational overhead. Simulating thousands of high-frequencies PWM switching events requires tiny time steps in finite element software.

The primary objective of this thesis study was the fundamental electromagnetic sizing of the machine. Sizing dictates the physical geometry required to deliver a specific nominal torque at a specific base speed. The torque density, magnetic saturation levels, and air-gap flux characteristics depend on the machine's geometry and the fundamental electrical currents, which are described by the d-q equations. Therefore, introducing high-frequency inverter switching circuits during the purely geometric sizing phase offers limited additional insight into the machine's absolute torque capability while exponentially increasing simulation times. By utilizing an ideal sinusoidal current source in ANSYS Maxwell to lock the machine into its rated torque-speed operating point, the fundamental electromagnetic parameters were isolated and improved. This approach ensures a mathematically rigorous sizing process, providing an optimized physical machine that can accommodate advanced control methods like FOC in subsequent development stages.

The foundational finite element 2D base model of outer-rotor FSPM machine for this thesis study is defined within the ANSYS Maxwell 2D. This finite element study is split into two computational stages, the first stage involves net inductance computation using magnetostatic solver and the second stage is the transient analysis using transient solver.

3.5 Geometry Setup and Magnetostatic Inductance Computation

The first stage involves magnetostatic simulation, where the core physical and electrical parameters of the machine are established. The process starts with the geometric construction of all fundamental machine components, including the inner stator, the outer rotor, the permanent magnets, and the coil windings based on the analytical sizing from chapter 2. Figure 19 shows the constructed 2D geometry in the Maxwell environment.

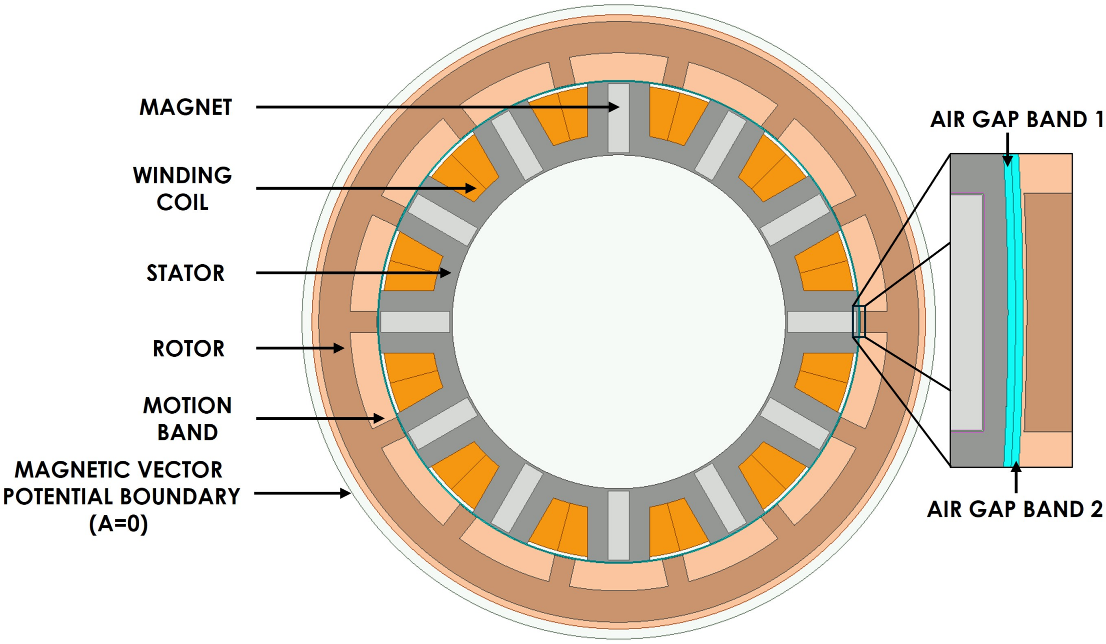

Figure 19: 2D base model geometry built in ANSYS Maxwell 2D

Following the geometry creation using boolean operations in the Maxwell environment, specific electromagnetic materials are assigned to each respective component, as defined in the Table 5, to accurately model their permeability and saturation characteristics. The B-H and J-H curves corresponding to Vacodym 633HR magnets used for this study are shown in Appendix A. After the completion of the material assignment, an electromagnetic boundary circle is drawn with its radius 5 mm larger than the outer-rotor diameter, where the magnetic vector potential ($A = 0$) is assigned. This boundary is created to prevent the solver from computing magnetic fields outside this boundary. This Dirichlet boundary condition effectively contains the magnetic flux within the required boundary.

Table 5: Material specifications of motor components

Component	Material
Stator & Rotor	Vacoflux 48 (0.1 mm)
Magnets	Vacodym 633HR (150°C)
Windings	Electrical-grade Copper

The coil windings in 2D geometry are chosen and assigned with current excitations, where both the current direction and the required number of turns are defined. A crucial computational advantage provided by ANSYS Maxwell is its ability to simplify complex coil geometries. If a coil winding physically consists of n turns and m strands, it is not required to draw every individual conductor cross section. Instead, a simple rectangular or trapezoidal cross section can be modeled inside the slots, depending on whether the corresponding stator pole geometry is rectangular or trapezoidal. The base 2D model in this study utilizes a trapezoidal geometry for copper windings. The winding pattern for the design is shown in Figure 20.

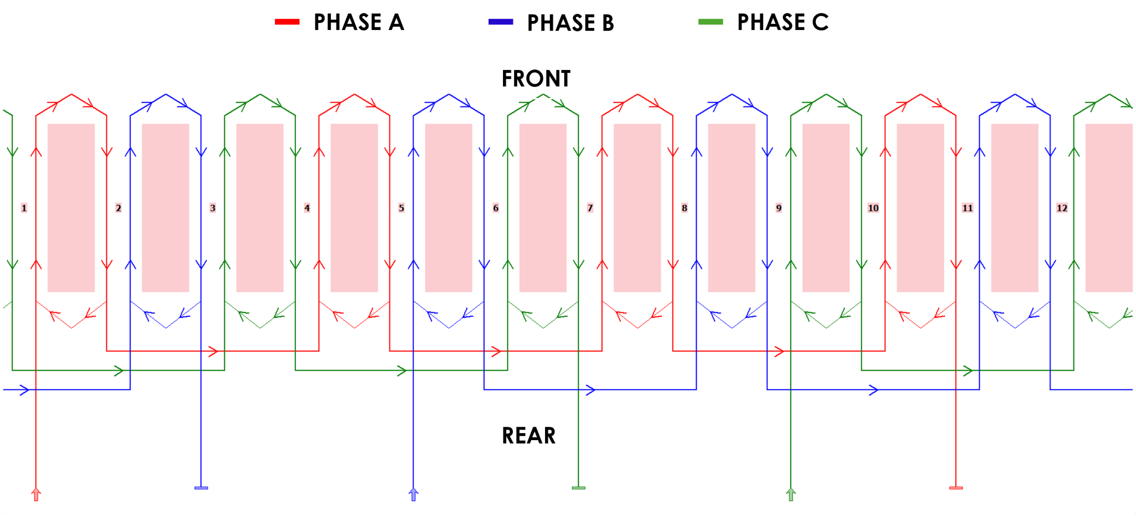

Figure 20: Winding pattern generated for the base model using ANSYS Motor-CAD

After the current excitations are assigned to every coil winding, a matrix parameter is created to group the respective coils into three phases, namely Phase A, Phase B, and Phase C, which is helpful in calculating the inductance profiles of individual phases. Then, the outer rotor is selected individually, and a torque parameter is assigned to it. This specific parameter assignment is needed for measuring the static torque generated by the rotor during the magnetostatic computation.

Before starting the analysis, the created 2D geometry needs to be meshed with finite elements. In order to capture the flux density at the air gap, a non-model object in the form of a circle is drawn exactly at the center of the air gap. Two air-gap bands with different radii are drawn in the shape of a hollow cylinder within the air gap as shown in detailed view in Figure 19. These bands are chosen, and a mesh element size of 0.5 mm is assigned; the line drawn to capture the air-gap flux density is assigned with an element size of 0.2 mm.

Aspect ratio is defined as the ratio of maximum edge length to the minimum edge length in a mesh element.

$$\text{Aspect Ratio} = \frac{\text{Maximum Edge Length}}{\text{Minimum Edge Length}}. \tag{44}$$

For a triangular mesh element, maintaining an aspect ratio close to 1 enables the mesh element to form an equilateral triangle. Higher aspect ratios would result in stretched, skewed, or flattened mesh elements that make it difficult to achieve an accurate mathematical interpolation across the element's volume, leading to inaccurate results. An aspect ratio of 3 is applied to every part, including the vacuum, inside the magnetic vector potential boundary. Finite element analyses have been conducted by keeping an aspect ratio of 1 and 3; it was found that by keeping the aspect ratio as 3, the difference in results between when the aspect ratio is kept as 1 is less than 0.5%, but this helps in reducing the computation time. The meshed 2D cross section of the base model is shown in Figure 21.

The main objective of this step is to extract air-gap flux density, specifically the radial flux density component which can be calculated using the fields calculator in ANSYS Maxwell. The computed radial flux density plot in the air gap is shown in Figure 22 with the peak value of flux density reaching close to 2.1 T in the air gap . This step also helps to capture the net inductance value of the phase coils, which is required for running the transient simulation in the next step. This calculated inductance value is needed to assign all three-phase inductor components in the external circuit used during transient analysis. To accurately compute this net inductance, the matrix parameter is used. This process involves energizing Phase A coils with a current of 1 A, when the rotor

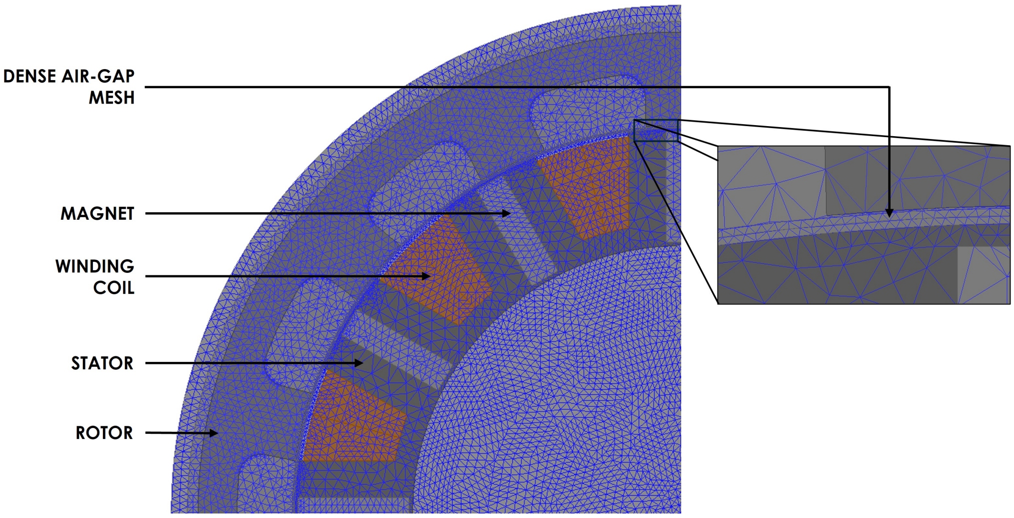

Figure 21: Meshed 2D base model highlighting the air-gap region

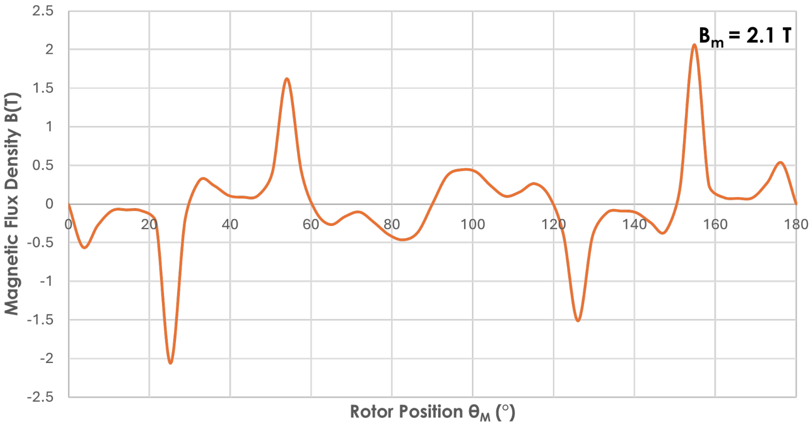

Figure 22: Radial flux density distribution in the air-gap region (half-model using 180° symmetry)

is aligned with Phase A stator poles. The self-inductance of Phase A coils, the average value of the mutual inductances between Phase A and the other two phases are computed and the net inductance value for the Phase A coil is calculated as,

$$L_{\text{net}_\text{A}} = L_{\text{self}_\text{A}} - \left(\frac{M_{\text{AB}} + M_{\text{AC}}}{2} \right). \tag{45}$$

From the computation, the values of L_{self_A}, M_{AB}, and M_{AC} are found and the net inductance of Phase A is found to be,

$$L_{\text{net}_\text{A}} = 73.9\,\mu\text{H} - \left(\frac{-35.7\,\mu\text{H} + (-35.8\,\mu\text{H})}{2} \right), \tag{46}$$

$$L_{\text{net}_\text{A}} = 73.9\,\mu\text{H} - (-35.7\,\mu\text{H}), \tag{47}$$

$$L_{\text{net}_\text{A}} = 109.7\,\mu\text{H}. \tag{48}$$

3.6 Transient Analysis and Results

After extracting L_{net_A} from step 1, the methodology transitions to step 2. In this step, the solver within the Maxwell environment is changed from magnetostatic to transient type, with the same 2D geometry from step 1 with minor changes. The material assignments are the same, but the excitations are converted to coil excitations rather than current excitations to couple the external circuit with the windings. The specific number of turns n, and the coil polarity are defined during this assignment. During this configuration, the physical nature of the conductors must be specified; a stranded geometry is chosen over a solid structure to accurately reflect the true winding composition and to prevent the solver from computing larger eddy current losses within the copper area.

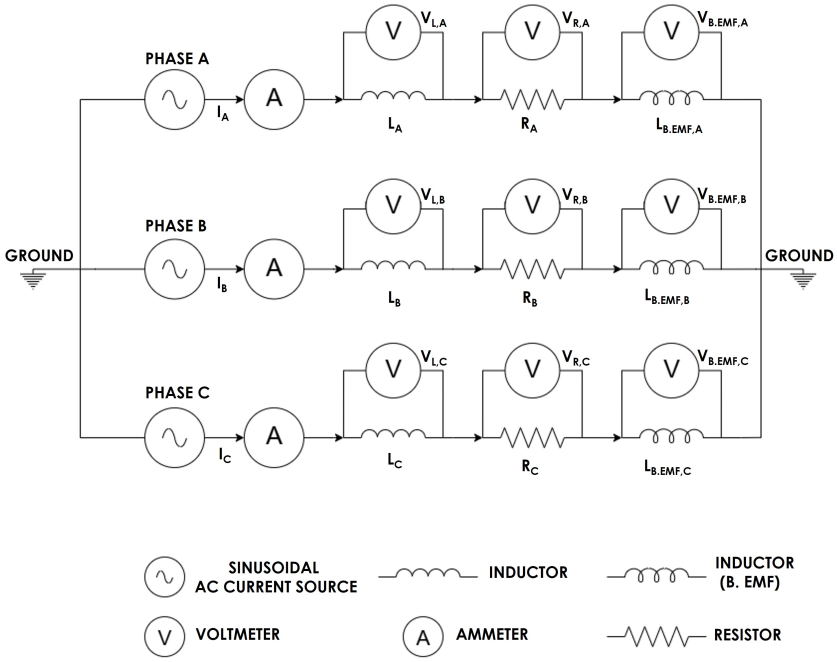

Figure 23: External circuit used for transient analysis

To accurately simulate the dynamic behavior of the outer-rotor FSM machine under load, an external circuit shown in Figure 23 is used. Each phase in this circuit has one sinusoidal current source, an inductor L_{A}, L_{B}, L_{C}, a resistor R_{A}, R_{B}, R_{C}, and another inductor for Back EMF measurement $L_{\mathrm{B.EMF,A}}, L_{\mathrm{B.EMF,B}}, L_{\mathrm{B.EMF,C}}$ connected in series. An ammeter is connected in series next to the current source to measure the three phase supply currents I_{A}, I_{B}, I_{C} and three voltmeters per phase are connected in parallel across the inductors, resistors and the windings to measure the inductance voltage drop $V_{\mathrm{L,A}}, V_{\mathrm{L,B}}, V_{\mathrm{L,C}}$, resistance voltage drop $V_{\mathrm{R,A}}, V_{\mathrm{R,B}}, V_{\mathrm{R,C}}$ and the Back EMF $V_{\mathrm{B.EMF,A}}, V_{\mathrm{B.EMF,B}}, V_{\mathrm{B.EMF,C}}$, respectively. The three AC current sources supply currents exactly at 120° phase shift between phases. The calculated net inductance value is assigned to all the inductor components across three phases in this external circuit.

An additional motion band is defined in the form of a hollow cylinder enclosing the outer rotor as shown in orange color in Figure 19. To ensure proper mesh generation at the sliding interface, the inner radius of this hollow cylindrical band is set to be 0.1 mm less than the rotor's inner radius, while the outer radius is extended to be 2 mm greater than the rotor's outer diameter and is enclosed by the enclosure with the boundary condition ($\mathbf{A} = 0$). The matrix and the torque parameters from the previous step are removed, as the transient solver dynamically computes these values across the time period. The meshing is left unchanged from Step 1, except the line drawn at the center of the air gap to capture the air-gap flux density is removed. And the time steps across one electrical period is kept as 60. One electrical period T_{elec} and each time step Δt in ms for the base design is calculated as follows,

$$T_{\mathrm{elec}} = \frac{60000}{Np} \text{ ms.} \tag{49}$$

$$T_{\text{elec}} = \frac{60000}{2500 \times 14} = 1.71429 \text{ ms.} \tag{50}$$

$$\Delta t = \frac{T_{\text{elec}}}{60} = \frac{1000}{Np}. \tag{51}$$

$$\Delta t = \frac{1.71429}{60} = 0.02857 \text{ ms.} \tag{52}$$

Before starting the analysis, it is necessary to identify the maximum flux position, or the d-axis position, when the phases are unenergized. This allows for the physical or virtual alignment of the rotor pole to a known reference frame. To maximize torque production, the phase currents must subsequently be applied 90 electrical degrees ahead of this maximum flux linkage position. Mathematically, the initial *d*-axis position can be calculated based on the machine geometry [48] as follows,

$$\theta_{\text{initial}} = \frac{\left(\frac{360^\circ}{N_{\text{r}}}\right)}{\left(\frac{N_{\text{s}}}{m}\right)}. \tag{53}$$

For the base design configuration with $N_{\text{r}} = 14$, $N_{\text{s}} = 12$, and $m = 3$ phases, the substitution and final value are,

$$\theta_{\text{initial}} = \frac{\left(\frac{360^\circ}{14}\right)}{\left(\frac{12}{3}\right)} = \frac{25.714^\circ}{4} = 6.4285^\circ. \tag{54}$$

To verify this through FEA, a transient analysis is performed where the external circuit is decoupled and the phases are supplied with 0 A. The simulation is executed for one full electrical period, and the flux linkage of Phase A is plotted against the rotor position in mechanical degrees. The mechanical rotor position at which the maximum flux linkage occurs corresponds to the d-axis. The relationship between the Phase A flux linkage and the rotor position is illustrated in Figure 24. Figure 24 shows the Phase A flux linkage peak occurs exactly at the calculated rotor position of 6.4285° and the FEA validates the mathematical equation in finding the maximum flux linkage position. The rotor position is then set to θ_{initial} and the current angle β is set to 90° electrical degrees ahead of the rotor position.

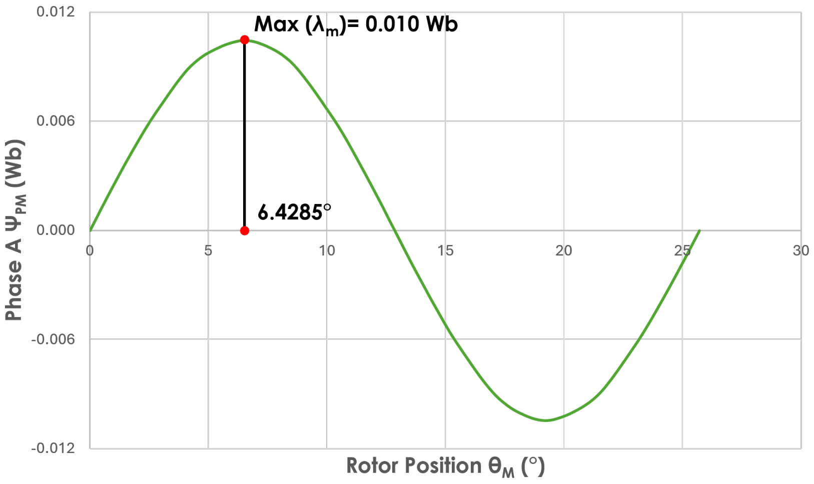

Figure 24: Phase A flux linkage versus rotor position

To analyze the machine's performance, a series of critical waveforms are extracted. Figure 25 shows the plot of the instantaneous torque curve captured across one electrical period when the external circuit is coupled and supplied with three-phase currents. Figure 26 shows the three-phase sinusoidal back EMF waveforms generated by the 2D base model making it suitable to run with FOC control.

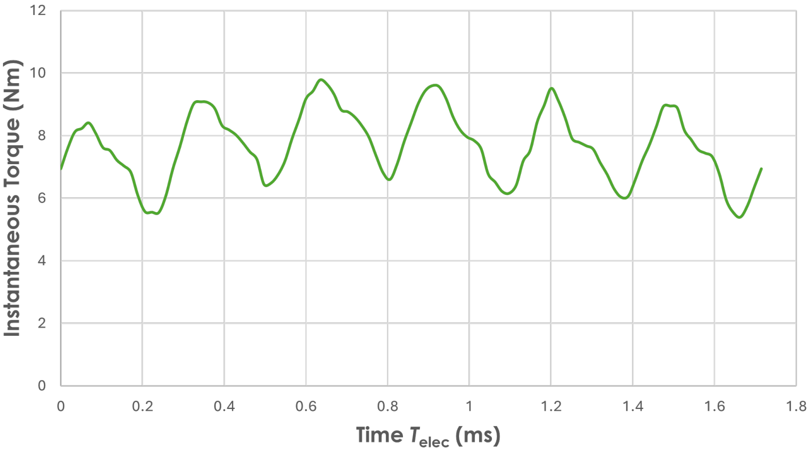

Figure 25: Transient torque curve of the base model

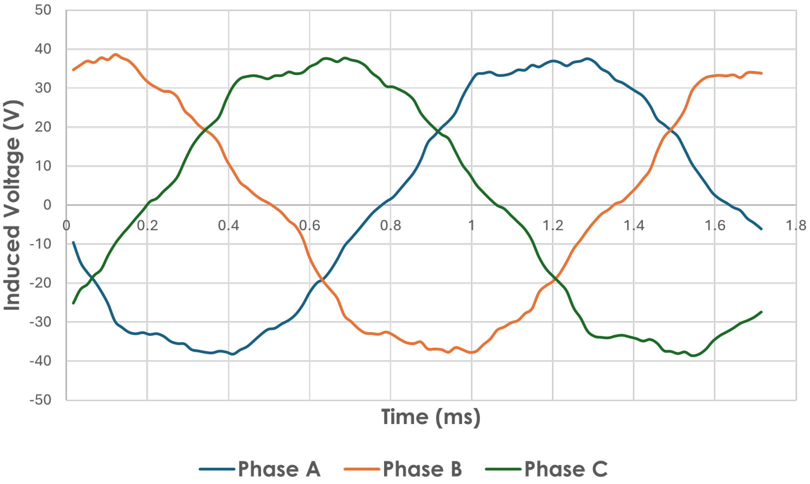

Figure 26: Transient three-phase back EMF waveforms

A critical observation is derived from the d and q axis inductances extracted during this transient study to analytically verify the torque production as per the equation (39). To obtain the inductance values, it is necessary to enable the apparent matrix computation before starting the transient analysis. As shown in Figure 27, the transient profiles of L_{d} and L_{q} expose that the numerical difference between the two waves is 7.6 % which is positive and negligible. Also, from Figure 28, it can be seen that all the current is supplied through q axis and no current through the d axis as the current angle is set to 90°. Because of this negligible d-q inductance difference, the saliency ratio of the machine is close to 1. Recalling the equation (39), this negligible difference between L_{d} and L_{q} along with 0 d-axis current effectively nullifies the reluctance torque component. Therefore, it is conclusively understood that the torque produced in this outer-rotor FSPM base model design is predominantly electromagnetic torque, due to the interaction between the permanent magnet flux linkage and the stator currents. If the difference between d- and q-axis inductances is significant, the current vector should be positioned in either the first or second quadrant of the d-q coordinate system, depending on the L_{d} and L_{q} values. The logic is expressed mathematically in the Table 6.

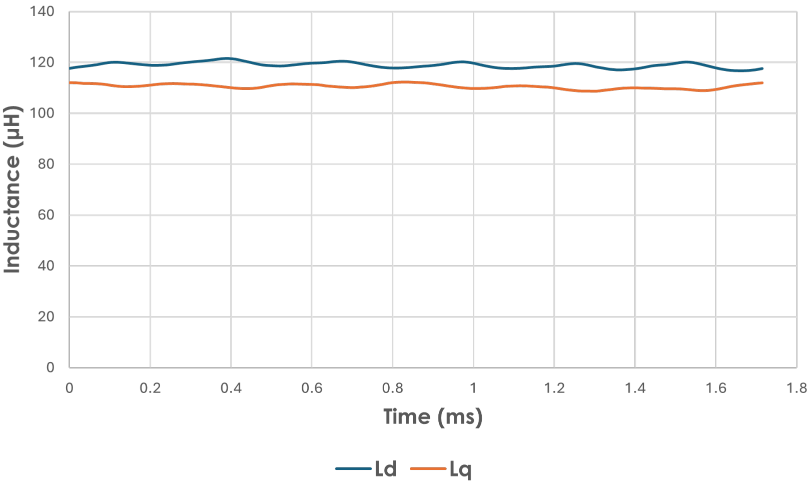

Figure 27: Transient d-q inductance characteristics

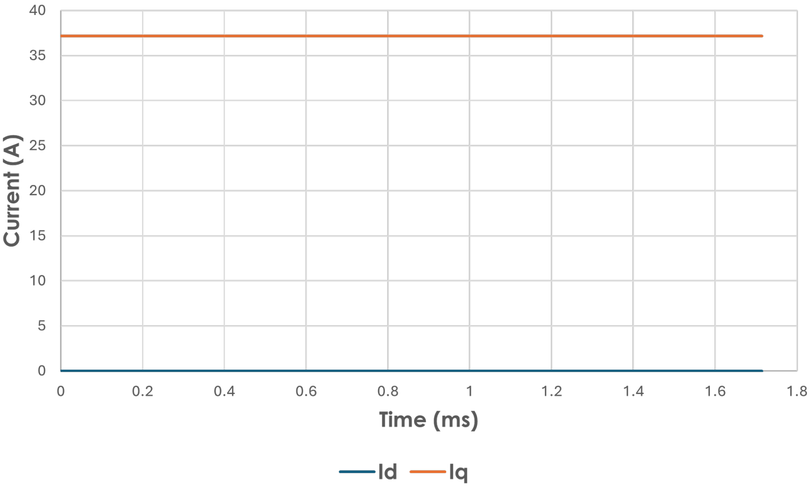

Figure 28: Transient d-q current waveforms

Table 6: Reluctance torque saliency conditions with corresponding quadrant mapping

Case	**Saliency Type**	**Inductance Condition**	**Current Vector**	**Quadrant**
Case 1	Positive Saliency	$L_\mathrm{d} > L_\mathrm{q}$	$I_\mathrm{d} > 0, I_\mathrm{q} > 0$	Quadrant I
Case 2	Negative Saliency	$L_\mathrm{d} < L_\mathrm{q}$	$I_\mathrm{d} < 0, I_\mathrm{q} > 0$	Quadrant II

Following the conditions in Table 6, when there is a difference between the d- and q-axis inductances, the current angle β can be positioned either in the first or second quadrant, depending on whether the saliency is positive or negative. In this way, the reluctance torque, although negligible, can still be utilized. A parametric sweep study of the current angle from 0° to 180° is done to find the optimal current angle at which the resultant torque magnitude is maximum. Figure 29 shows the study results of average torque versus current angle for the 2D base model. It can be seen from the curve that the maximum torque occurs at an angle lesser than 90° due to positive saliency. Though the difference in the resultant torque is negligible, this analysis helps understand that the maximum torque not always occurs at a current angle of 90°.

Losses in the copper windings are computed using the standard expression $(I_\mathrm{A}^2 + I_\mathrm{B}^2 + I_\mathrm{C}^2)R_\mathrm{phase}$. The phase resistance used in this calculation is temperature-dependent, as defined in equation (20)

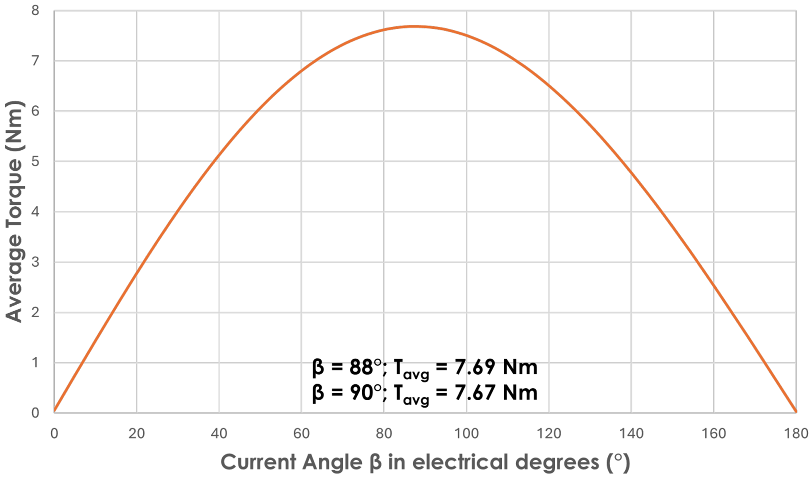

Figure 29: Current angle sweep study results

in Chapter 2, accounting for both ambient conditions and operational temperature rise. Using the instantaneous three-phase supply currents, the total transient copper loss is evaluated at each time step, and its average value over one electrical period for the base model is 45 W.

For the core loss computation in the stator and rotor steel, the "Electrical Steel" loss model is selected during the material assignment phase in ANSYS Maxwell. To enable the solver to accurately calculate losses across a range of operating frequencies, it is critical that the assigned material definition includes empirical B-H curve data and high-frequency power loss curves. Figures 30 and 31 show the B-H curve used for Vacoflux 48 (0.1 mm) and the corresponding B-P curves at different frequencies, obtained from the material library within the Maxwell solver.

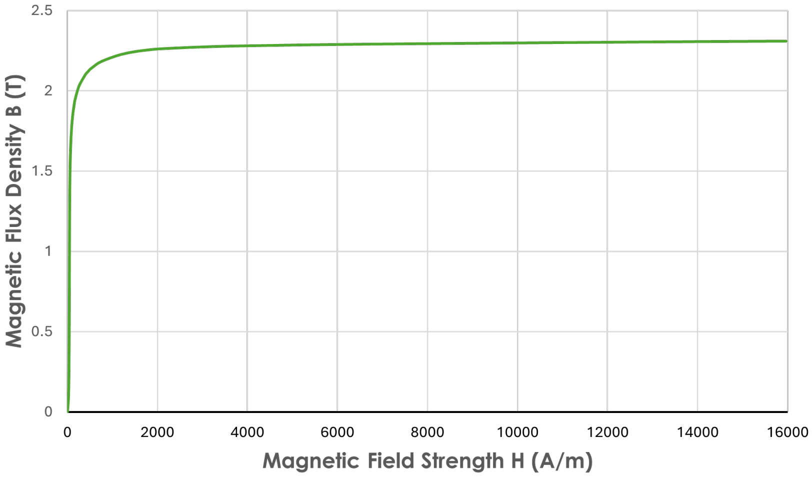

Figure 30: B-H curve for Vacoflux 48 (0.1 mm)

The total core loss calculation evaluates three distinct phenomena: the hysteresis loss component P_{h}, the classical eddy current loss component P_{e}, and the excess loss component P_{ex}. The mathematical expressions for these individual loss components are defined as follows:

$$P_{\mathrm{h}} = k_{\mathrm{h}} f B_{\mathrm{m}}^{2}. \tag{55}$$

$$P_{\mathrm{e}} = k_{\mathrm{e}} (f B_{\mathrm{m}})^{2}. \tag{56}$$

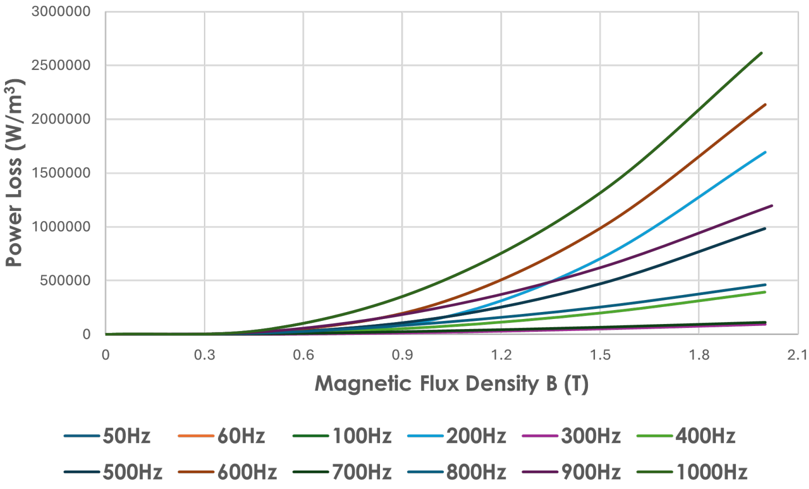

Figure 31: B-P curves for Vacoflux 48 (0.1 mm)

$$P_{\mathrm{ex}} = k_{\mathrm{ex}}(fB_{\mathrm{m}})^{1.5}. \tag{57}$$

Consequently, the fundamental core loss equation summarizing these elements is given by,

$$P_{\mathrm{core}} = k_{\mathrm{h}} f B_{\mathrm{m}}^2 + k_{\mathrm{e}}(fB_{\mathrm{m}})^2 + k_{\mathrm{ex}}(fB_{\mathrm{m}})^{1.5}. \tag{58}$$

Where the utilized core loss coefficients values are $k_{\mathrm{h}} = 87.299$, $k_{\mathrm{e}} = 0$, and $k_{\mathrm{ex}} = 6.648$, which were derived within ANSYS Maxwell from the existing B-P curves at different frequencies available for Vacoflux 48 0.1 mm. The total core loss obtained from the transient analysis for the base model is 17 W. The results obtained from this transient analysis, when current angle equals 88° are listed in Table 7.

Table 7: Electromagnetic performance results of the base model

Outputs	**Value**
T_{avg}	~7.7 Nm
T_{ripple}	57 %
P_{out}	2 kW
η_{avg}	96.5 %
V_{DC}	54.6 V
$I_{\mathrm{phase,rms}}$	26.3 A

4 Multi-Objective Optimization

Electrical machine performance is highly influenced by geometric configurations, necessitating optimization of the geometry to achieve the required performance characteristics, such as maximum torque, maximum efficiency and minimum torque ripple. Different optimization approaches are studied using the 2D base model developed in ANSYS Maxwell 2D for this thesis. Parametric Optimization is performed within ANSYS Maxwell 2D to establish an understanding of the key geometric parameters that affect machine performance. Following this sweep study, the later sections detail about multi-objective optimization, problem formulation, explaining key objectives, constraints, and input design variables chosen for the study. The selection of optimization approaches, including the use of an evolutionary algorithm and the development of the automation framework, was guided by discussions with M.Eng. Enrico Teichert. The automation framework required to create the necessary coupling between ANSYS Maxwell 2D and optiSLang for efficient evaluation of multiple design iterations is also explained. Further subsections provide an overview of the selected evolutionary algorithm, followed by the execution and results of direct optimization approach. To further explore the design space, a subsequent sensitivity analysis is performed, paving the way for the Meta-Model-Based Optimization study.

4.1 Parametric Optimization

To begin the refinement of the machine geometry, the parametric sweep study was performed utilizing the built-in capabilities of Maxwell 2D. As outlined in the sequence of interrelated steps described in the Research Gap and Problem Statement section, the initial stage of the optimization process involves a parametric sweep study. The selection of input variables for this initial stage required consideration of the software's computational limits. A parametric study with a large number of variables experiences exponential growth in design combinations. Exceeding 32000 combinations causes Maxwell 2D software to stop, making large-scale sweeps computationally unfeasible. Consequently, the parameter space was limited to two critical geometric variables, the permanent magnet arc β_{PM}, and the rotor tooth arc β_{R} for this study. These variables govern the respective thicknesses and angular spans of the permanent magnet and the rotor tooth respectively.

Stator geometric parameters, specifically the stator tooth thickness STW dictated by the stator tooth arc β_{s}, were excluded from this sweep study. Altering the stator tooth dimensions, both the tooth thickness and the yoke thickness SYW, directly modifies the available slot area for the phase windings. To maintain a slot fill factor constraint under such variations, the number of turns and parallel wire strands must be dynamically recalculated and adjusted for every combination during the simulation setup. Because automated dynamic winding reconfiguration was not practical within this parametric sweep study, the winding layout and the stator geometry were held constant. Furthermore, the initial magnetostatic study utilized to compute the net inductance of a phase, was bypassed during this study, as that specific process relies on winding modifications that were omitted from this step to reduce the simulation time. The parametric sweep was defined by discrete boundary limits and step sizes for the chosen variables. The permanent magnet arc placed in the stator was varied from 1° to 5° in increments of 0.5°, while the rotor tooth arc was varied from 1° to 5° in increments of 1°. Now, as the magnet arc increases, the thickness of the adjacent stator tooth decreases simultaneously keeping the β_{S} constant. This specific discretization yielded a mathematically bounded design space comprising 54 unique combinations. For each geometry combination, the transient analysis was performed for one electrical period. Despite the limited variable count, the computational expense remained significant.

Following the completion of the parametric sweep, critical performance output metrics were extracted for post-processing evaluation from Maxwell 2D. The primary operational objectives assessed were the average electromagnetic torque, the average efficiency and the transient torque ripple. The extracted data from the Maxwell was processed using a custom-made python script shown in Appendix B. Since these parameters have individual physical units and numerical scales, a linear minimum-maximum normalization transform is performed on the extracted data to a uniform dimensionless parameters ($T_{\text{avg,norm}}, \eta_{\text{avg,norm}}, T_{\text{ripple,norm}}$) whose scale range from 0 to 1 prior to comparative evaluation. For objectives intended to be maximized, such as average electromagnetic torque and average efficiency, standard linear scaling is applied, which are mathematically expressed as,

$$T_{\text{avg,norm}} = \frac{T_{\text{avg}} - T_{\text{avg,min}}}{T_{\text{avg,max}} - T_{\text{avg,min}}}. \tag{59}$$

$$\eta_{\text{avg,norm}} = \frac{\eta_{\text{avg}} - \eta_{\text{avg,min}}}{\eta_{\text{avg,max}} - \eta_{\text{avg,min}}}. \tag{60}$$

Conversely, performance parameter requiring minimization, like the transient torque ripple utilize an inverted normalization logic to ensure lower values translate to higher normalized scores, formulated as,

$$T_{\text{ripple,norm}} = \frac{T_{\text{ripple,max}} - T_{\text{ripple}}}{T_{\text{ripple,max}} - T_{\text{ripple,min}}}. \tag{61}$$

Following this independent mathematical normalization, the definitive optimal geometry is identified by aggregating these individual metrics into a singular composite index using a weighted average. Because this preliminary design phase prioritizes overall torque production, efficiency, and torque quality equally, an equal weighting distribution is applied across the objectives, yielding the final scoring function given as,

$$S_{\text{total}} = w_1 T_{\text{avg,norm}} + w_2 \eta_{\text{avg,norm}} + w_3 T_{\text{ripple,norm}}. \tag{62}$$

Where the individual priority coefficients are established as $w_1 = w_2 = w_3 = \frac{1}{3}$. The corresponding phase voltage and phase RMS current for each design combination were also evaluated during the transient simulations and observed that all designs operated within acceptable electrical limits.

Parametric Optimization Results

The post-processed contour plots of this sweep study are visualized in Figures 32, 33 and 34 which provide a comprehensive understanding of the interaction between the design variables and their combined effect on performance metrics. The torque ripple response surface shows a highly nonlinear behavior with respect to both β_{PM} and β_{R}. The torque ripple varies from approximately 35% to 75% across the design space. Higher torque ripple values above 65% are predominantly associated with lower β_{R} angles (4° to 5°) and mid-level β_{PM} values (2.5° to 3.5°). In contrast, lower torque ripple values below 45% are achieved at higher rotor arc angles ($\beta_{\text{R}} = 9°$ to $10°$) combined with larger magnet arc values ($\beta_{\text{PM}} = 4°$ to $5°$). This trend indicates that increasing the rotor arc improves the magnetic flux distribution in the air gap, thereby reducing torque fluctuations. The average efficiency response surface shows a smoother and more gradual variation compared to torque ripple. Efficiency values range from approximately 92% to 97%, with higher efficiencies achieved at larger values of both β_{PM} and β_{R}. Conversely, lower arc values ($\beta_{\text{PM}} < 2°, \beta_{\text{R}} < 6°$) result in reduced efficiency due to weaker electromagnetic interaction between the poles and also

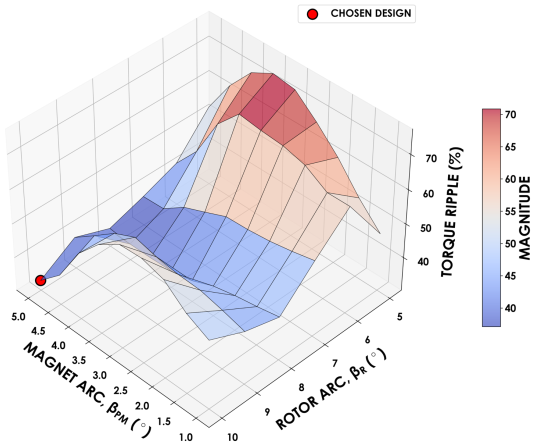

Figure 32: Torque ripple response surface

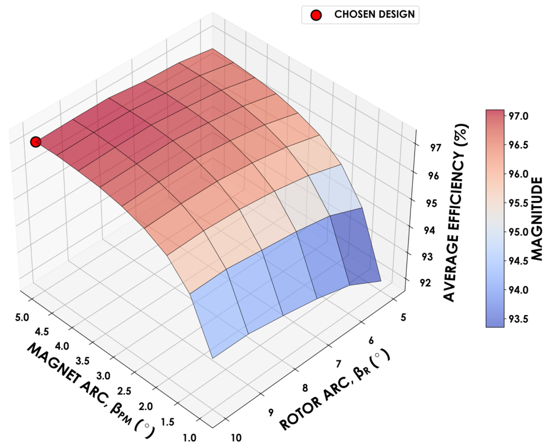

Figure 33: Average efficiency response surface

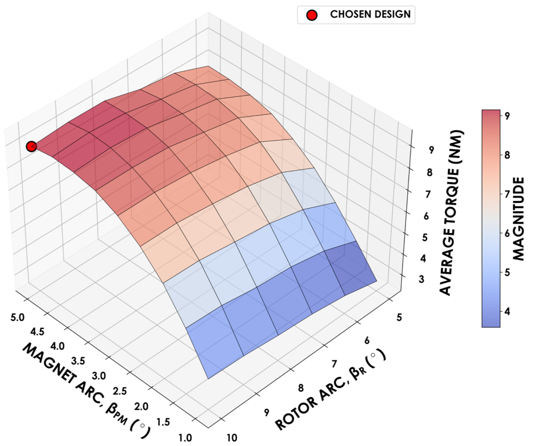

Figure 34: Average torque response surface

due to increased saturation. The average torque response demonstrates a clear increasing trend with respect to both design variables. Torque values range from approximately 3 Nm to 9.5 Nm, with the highest torque values obtained at larger β_{PM} and β_{R} angles. At lower arc values ($\beta_{\mathrm{PM}} = 1°, \beta_{\mathrm{R}} = 5°$), the torque decreases significantly to below ∼4 Nm due to reduced effective air-gap flux density. This highlights the importance of adequate arc values in achieving electromagnetic coupling and higher torque production. Although the optimal design was identified at $\beta_{\mathrm{PM}} = 5°$ and $\beta_{\mathrm{R}} = 10°$, it is important to note that this point lies at the boundary of the explored design space, as evident from the response surface plots. This indicates that the obtained solution is not necessarily a global optimum, but rather the best solution within the constrained and discretized parameter range considered in this study. The average torque and efficiency response surfaces show a consistent trend of improving performance with increasing β_{PM} and β_{R}, suggesting that further improvements may be achievable beyond the current upper bounds. Therefore, the present study represents a preliminary design space exploration rather than a complete optimization. The results of the chosen design in comparison with the base design is shown in Table 8.

This Parametric Sweep Optimization approach is restricted by the combinatorial explosion of the design space. Expanding this preliminary 54 permutation sweep includes essential stator parameters exponentially increasing the combinations, causing the Maxwell solver to stall. Furthermore, relying on the rigid discrete steps of 0.5° and 1° inherently overlooks continuous optimal values that could exist fractionally between these rigid boundaries. Also, the finite element sweeps lack dynamic phase windings design change to maintain a constant slot fill factor when stator dimen-

Table 8: Comparison of electromagnetic performance between the base model and parametric sweep design

Outputs	**Base Design**	**Parametric Sweep Design**	**Difference**
T_{avg}	7.7 Nm	8.97 Nm	+16.49%
T_{ripple}	57%	33%	−42.11%
P_{out}	2 kW	2.35 kW	+17.50%
η_{avg}	96.5%	97%	+0.52%
V_{DC}	54.6 V	67.3 V	+23.2%
$I_{\text{phase,rms}}$	26.3 A	26.3 A	-

sions are modified. These constraints necessitate the transition to the continuous, multi-variable multi-objective optimization framework detailed in the subsequent sections.

4.2 Multi-Objective Optimization

The Parametric Optimization approach discussed in section 4.1 is suitable for initial refinement, but it is limited. To overcome these limitations and to explore continuous multidimensional design space, a formal mathematical optimization framework is necessary. Mathematical optimization is a fundamental process in engineering design, utilized to systematically identify the best possible solution from a vast array of feasible alternatives. At its core, an optimization problem requires translating real world design goals and physical limitations into a mathematical framework [49]. This involves defining a specific objective function to evaluate the quality of a design, alongside a set of constraints that the design must obey to be considered valid.

In a standard, single objective constrained optimization problem, the goal is to find a vector of design variables, $\mathbf{x}$, that minimizes a scalar objective function $f(\mathbf{x})$ [49]. Mathematically, this basic optimization is expressed as,

$$\min f(\mathbf{x}) \tag{63}$$

subject to,

$$\mathbf{x} \in \Omega \tag{64}$$

Here, Ω represents the feasible space, the bounded region containing all physically, geometrically, and electrically viable designs. This feasible space is defined by the mathematical boundaries known as functional constraints, which consist of inequality constraints $g_i(\mathbf{x})$ and equality constraints $h_j(\mathbf{x})$, the feasible set is formally written as,

$$\Omega := \left\{ \mathbf{x} \in \mathbb{R}^n \;\middle|\; \begin{array}{ll} g_i(\mathbf{x}) \leq 0, & i = 1, \ldots, r \\ h_j(\mathbf{x}) = 0, & j = 1, \ldots, m \end{array} \right\}. \tag{65}$$

In this formulation, $\mathbb{R}^n$ denotes the n-dimensional Euclidean space of real numbers, where n represents the number of independent design variables. Any generated design $\mathbf{x}$ that violates these constraints falls outside the feasible space and is rejected by the solver. While single objective optimization is highly effective for linear problems, advanced electrical machine design rarely involves a single, isolated goal. Instead, it requires simultaneously satisfying multiple, often intrinsically conflicting objectives such as maximizing average torque while simultaneously attempting to minimize torque ripple. In these complex scenarios, the problem transitions into Multi-Objective

Optimization (MOO). Instead of minimizing a single scalar function $f(\mathbf{x})$, MOO evaluates a vector of objective functions simultaneously,

$$\min \mathbf{F}(\mathbf{x}) = [f_1(\mathbf{x}), f_2(\mathbf{x}), \ldots, f_k(\mathbf{x})]. \tag{66}$$

Because these objectives inherently conflict, there is almost never a single perfect design that achieves the absolute minimum for all functions concurrently. Improving one objective such as increasing average efficiency typically results in the degradation of another. Consequently, a MOO solver does not search for a single global minimum. Instead, it searches for a set of optimal compromises, mathematically referred to as the Pareto-optimal front. A specific design candidate is considered Pareto-optimal if no single objective can be further improved without directly penalizing at least one other objective. The ultimate goal of the MOO algorithm is to discover and populate this Pareto front, presenting a clearly defined boundary of the absolute best theoretical trade-offs available within the designated feasible space.

4.2.1 Problem Formulation

Unlike the sweep study, the optimization algorithms can dynamically evaluate complex geometric permutations while simultaneously adhering to interrelated physical and electrical boundaries. To successfully deploy the algorithms within the ANSYS optiSLang environment, the design problem must be rigorously defined. This formulation establishes the precise operational targets the algorithm must pursue and the absolute boundaries it cannot violate.

For the primary iteration of the multi-objective optimization, three core operational objectives were established.

$$\text{Objectives:} \quad \begin{cases} \text{Maximize } T_{\text{avg}} \\ \text{Maximize } \eta_{\text{avg}} \\ \text{Minimize } T_{\text{ripple}} \end{cases} \tag{67}$$

In addition to these objectives, electrical constraints were imposed to ensure the algorithm only converges on designs that are practically realizable and safely testable with the existing experimental setup as explained in the problem statement. The physical machine prototype can only be electrically excited by the inverter and power supply hardware that is available in the experimental test setup. This hardware has a maximum DC bus supply limit of 120 V and a maximum phase current capacity of 100 A. To provide a necessary safety margin and operational headroom, the optimization constraints were established below these absolute hardware limits expressed as,

$$\text{Constraints:} \quad \begin{cases} V_{\text{DC}} \leq 100\,\text{V} \\ I_{\text{phase,rms}} \leq 80\,\text{A} \end{cases} \tag{68}$$

Any evaluated geometry that violates either of these electrical boundaries is classified as unfeasible regardless of its resulting electromagnetic performance.

Input Variables

The input variables chosen for this design study are listed with the respective description and symbol in Table 9.

Note: Rotor tooth taper ratio $R_{\text{outer,taper}}$ is used as a scaling factor in the analytical expression defining a polyline in ANSYS Maxwell 2D. This polyline is composed of two arcs and one line

Table 9: Definition and description of input design variables for the optimization study

Symbol	**Parameter Name**	**Description**
γ_{β_s}	Stator Arc Ratio	Ratio of stator pole arc to pole pitch (β_S/α_S).
γ_R	Rotor Yoke Thickness Ratio	Independent coefficient for rotor yoke thickness.
γ_S	Stator Yoke Thickness Ratio	Independent coefficient for stator yoke thickness.
$R_{\text{outer,taper}}$	Rotor Tooth Taper Ratio	Defines the rotor tooth taper angle at the yoke intersection.
$R_{\text{tooth,ratio}}$	Rotor Tooth Thickness Ratio	Independent rotor tooth thickness ratio, equivalent to β_R.
R_{thick}	Magnet Thickness Ratio	Independent magnet thickness ratio, equivalent to β_{PM}.
R_f	Fillet Ratio	Fillet radius at the rotor tooth-yoke intersection.
n	Number of Turns per coil	Total number of wire turns in each coil.
Strands	Parallel Strands	Number of parallel conductors per turn.

segment, representing one half of the rotor tooth geometry. Varying this factor modifies the effective taper of the tooth while preserving geometric continuity.

$$\theta_{\text{taper}} = R_{\text{outer,taper}} \cdot \left[\tanh\left(\frac{\sin\left(\frac{\beta_R}{2}\right) \cdot (0.5\,\text{IRD} + \text{RTH})}{\cos\left(\frac{\beta_R}{2}\right) \cdot (0.5\,\text{IRD} + \text{RTH})} \right) \cdot \frac{180}{\pi} \right] \tag{69}$$

4.2.2 Automation Framework

The fundamental limitation of the conventional parametric sweep is its exponential increase in computations as the design space expands, making more additions of input variables to the optimization unfeasible along with the input variable value selection being discrete, and not continuous. To overcome this limitation and to enable multi objective optimization, an automation framework is necessary and it was developed using python. The developed script is added in the Appendix C.

The script acts as a bridge between ANSYS Maxwell and ANSYS optiSLang. This framework eliminates the limitation of testing only predefined, discrete values as in Parametric Optimization. It also automatically adjusts interrelated physical boundaries ensuring the algorithm can identify the best possible design without generating impossible geometries. The automation framework developed is shown in Figure 35.

The execution begins by setting up a secure workspace. To prevent software crashes or file corruption when running hundreds of tests, the script creates a separate unique folder for every single design combination. It then copies the original simulation template into this safe folder before making any parameter changes. After setup, the script dynamically calculates the machine's geometry from the chosen input variable values. Instead of directly defining linear dimensions like length and thickness, the script parameterizes the geometry using ratios defined in the machine sizing chapter, which are used to determine the exact geometry of the active materials.

Once, the input variables are chosen from the defined range. The magnet height is kept constant as the shaft and the stator diameters remain unchanged, whereas the magnet thickness M_T is

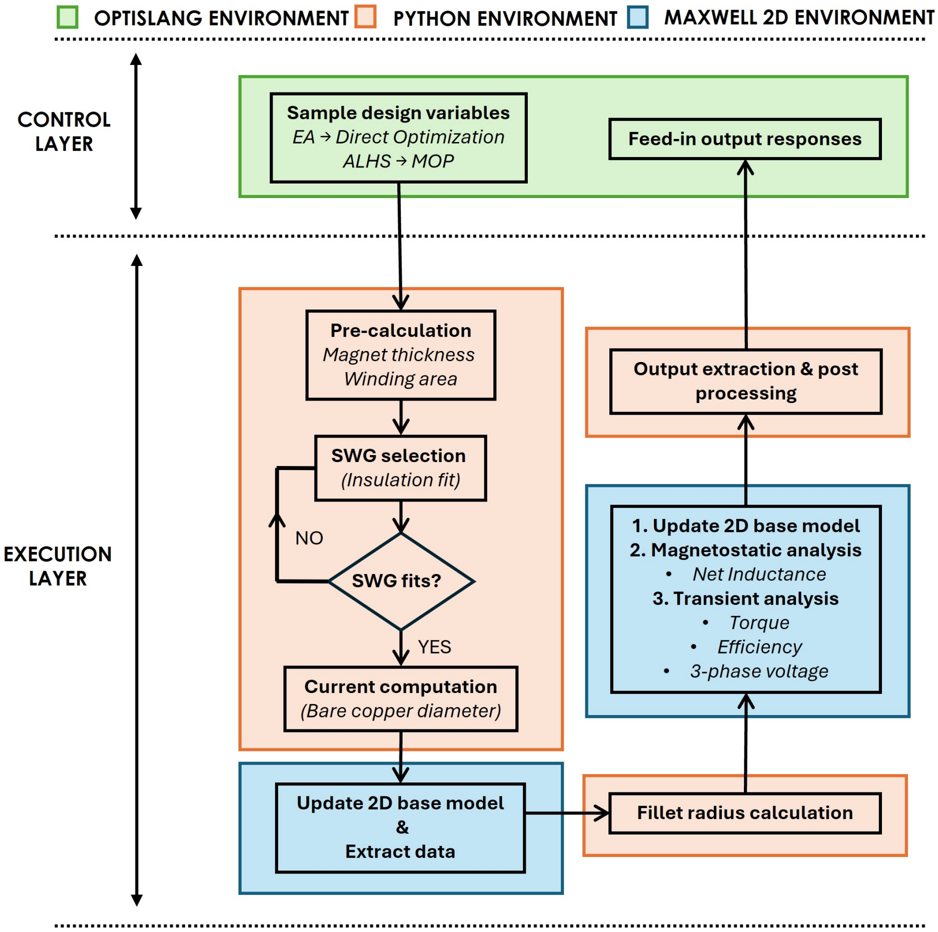

Figure 35: Automation framework flowchart

calculated from the inner rotor diameter IRD, air gap AG, and the stator pole angle β_s using,

$$\beta_\mathrm{s} = \alpha_\mathrm{s}\gamma_{\beta_\mathrm{s}}\left(\frac{\pi}{180}\right). \tag{70}$$

$$M_\mathrm{T} = R_\mathrm{thick}(\mathrm{IRD} - 2\mathrm{AG})\sin\left(\frac{\beta_\mathrm{s}}{2}\right). \tag{71}$$

An advancement of this framework is its automated winding area and wire sizing routine, which bypasses the limitations of the conventional parametric sweep. As optiSLang iteratively alters stator geometry parameters, the physical space available for the copper phase windings inherently fluctuates. To determine the exact available slot area, the script mathematically reconstructs the stator geometry from the inside out. It first calculates the physical dimensions of the stator teeth and yoke based on the optimizer's geometric ratios β_s and γ_s,

$$\mathrm{STW} = (\mathrm{IRD} - 2\mathrm{AG})\sin\left(\frac{\beta_\mathrm{s}}{2}\right). \tag{72}$$

$$\mathrm{SYW} = \gamma_\mathrm{s}\mathrm{STW}. \tag{73}$$

$$\mathrm{STH} = \left(\frac{\mathrm{IRD} - S_\mathrm{dia}}{2}\right) - (\mathrm{AG} + \mathrm{SYW}). \tag{74}$$

With these fundamental dimensions established, the script computes the cross-sectional areas of the internal non-winding components. The area of the shaft A_{shaft}, the stator yoke A_{yoke}, and the total area occupied by the stator teeth A_{teeth} are derived as follows,

$$A_{\text{shaft}} = \frac{\pi S_{\text{dia}}^2}{4}. \tag{75}$$

$$A_{\text{yoke}} = \frac{\pi}{4}\left((S_{\text{dia}} + 2\text{SYW})^2 - S_{\text{dia}}^2\right). \tag{76}$$

$$A_{\text{teeth}} = N_{\text{s}}\left((\text{IRD} - 2\text{AG})\frac{\beta_{\text{s}}}{2}\right)\text{STH}. \tag{77}$$

To account for the precise geometry of the slot openings, the script calculates the trapezoidal area of the slot shoe A_{hs}. It determines the untoothed circumference at the air-gap interface X and at the depth of the slot opening height Y, at depth hs_0 and aggregates them across all slots,

$$A_{\text{hs}} = \left(\frac{X+Y}{2}\right)(2hs_0N_{\text{s}}). \tag{78}$$

Finally, the script calculates the total internal stator area A_{stator} and subtracts all previously derived structural components to isolate the precise copper winding area available per individual slot A_{slot},

$$A_{\text{stator}} = \frac{\pi(\text{IRD} - 2\text{AG})^2}{4}. \tag{79}$$

$$A_{\text{slot}} = \frac{A_{\text{stator}} - (A_{\text{shaft}} + A_{\text{yoke}} + A_{\text{teeth}} + A_{\text{hs}})}{2N_{\text{s}}}. \tag{80}$$

Upon calculating this precise available slot area, the script programmatically interrogates an external database containing standard industrial wire sizes (SWG Table) which is attached in Appendix D. It automatically isolates the specific standard wire gauge that provides the requisite copper cross section to satisfy the chosen number of turns, the required number of parallel strands, and the 50% fill factor constraint. This dynamically selected wire diameter is then written directly into the Maxwell model, ensuring the design remains physically manufacturable. Based on the calculated stator geometry, the mean length of a turn is calculated as explained in chapter 2 and is sent to Maxwell for phase resistance calculation.

To guarantee the generated machine operates within the designated thermal boundaries, the script subsequently performs a dynamic current derivation. Utilizing the physical cross-sectional area of the automatically selected wire A_{cond} and the designated number of parallel strands, the script calculates the absolute maximum phase RMS current $I_{\text{phase,rms}}$ that can be injected into the coils while respecting the predefined current density limit J_{max},

$$I_{\text{phase,rms}} = J_{\text{max}}A_{\text{cond}}\text{Strands}. \tag{81}$$

If the derived current mathematically exceeds the current constraint limit, the script immediately flags the design as a constraint violation for the optimizer.

The script also incorporates an adaptive filleting mechanism via physical edge measurement. Prior to the electromagnetic simulation, the script commands the Maxwell 2D environment to measure the two rotor edge lengths 1 & 2 as mentioned in Figure 36. To establish a safe physical dimension

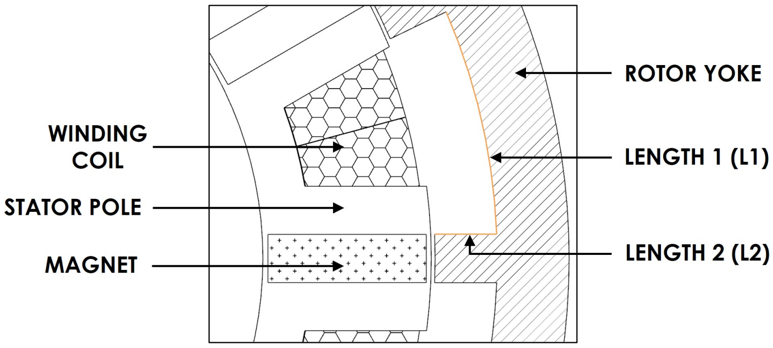

Figure 36: Measured edge lengths on the rotor

and prevent broken geometry generation, the lowest length value is assigned to $L_{\mathrm{edge,min}}$. Then, utilizing the optimizer-chosen fillet ratio R_{f}, the localized fillet radius R_{fillet} is calculated as,

$$L_{\mathrm{edge,min}} = \min(L_1, L_2), \tag{82}$$

$$R_{\mathrm{fillet}} = \frac{L_{\mathrm{edge,min}}}{2} R_{\mathrm{f}}. \tag{83}$$

Once the geometry and electrical boundaries are established, the script executes a sequential two-step FEA in Maxwell 2D. It first initiates a magnetostatic simulation to extract the net phase inductance. This inductance value is dynamically used in the subsequent transient simulation to evaluate the average torque, torque ripple, average efficiency, and three-phase voltages. Upon successful completion of each solver, the python framework analyses the exported raw waveform data files and calculates average torque, torque ripple, average efficiency, three-phase voltages and currents. Based on three-phase voltage values, the script computes the necessary DC bus voltage to verify inverter compatibility, and returns the dataset back to the optiSLang environment. This continuous loop allows the optimizer to mathematically evaluate the fitness of the current generation and proceed with navigating the multidimensional design space. The DC voltage is computed from the total voltage drop measured across the winding resistance, inductance and back-EMF as,

$$V_{\mathrm{DC}} = \frac{V_{\mathrm{phase,peak}}}{0.866}. \tag{84}$$

The factor 0.866 accounts for the maximum linear modulation index achievable by a standard three-phase inverter utilizing SPWM.

4.2.3 Evolutionary Algorithm

The design space of an electrical machine is highly non-linear, highly dimensional, and defined by conflicting objectives, classical gradient based optimization methods are often insufficient. Classical methods typically require a single starting point, rely on differentiable objective functions, and struggle to autonomously balance multi-objective trade-offs, often requiring highly complex mathematical extensions just to approximate a multi-objective tradeoff [50]. Consequently, modern electrical machine optimization relies on evolutionary algorithms (EAs), more specifically the Non-dominated Sorting Genetic Algorithm II (NSGA-II), because evaluating contradictory parameters rarely yields a single optimal design, but rather necessitates finding a set of Pareto optimal solutions [51]. This algorithm is favored for ability to balance conflicting objectives, such as maximizing average torque while minimizing torque ripple [52].

To work out the complex multi-objective optimization problem formulated for this study, the developed framework leverages the specific evolutionary algorithm integrated within the ANSYS optiSLang environment. Evolutionary algorithms are stochastic search methods that mimic the biological processes of natural evolution, specifically selection, recombination, and mutation. The algorithm begins by generating an initial diverse population of individual motor designs. In the optiSLang environment each individual design is computationally evaluated for its fitness based on the defined objective functions and physical constraints. The algorithm then applies evolutionary operators, it selects the highest performing designs to act as parents, recombines their specific input variable traits through crossover to create new offspring and introduces random mutations to maintain genetic diversity and prevent the search from mathematically stalling in local optima. This iterative cycle allows the optiSLang evolutionary algorithm to efficiently search different design landscapes, handle problems with unfeasible designs and simultaneously process both discrete and continuous variables.

Within the scope of this thesis, the optiSLang evolutionary algorithm is strategically deployed using two distinct operational methodologies to solve the formulated problem. The first approach is the Direct Optimization, where the evolutionary algorithm assumes direct control over the parameter generation from the defined input variables range and interacts exclusively with the custom python automation script. Every design created per cycle is evaluated using a full, computationally expensive FEA in ANSYS Maxwell. The second approach is Meta-Model-Based Optimization. To reduce the heavy computational burden of hundreds of direct finite element analyses, advanced statistical sampling techniques like Advanced Latin Hypercube Sampling (ALHS) is utilized to perform a sensitivity analysis. ANSYS optiSLang then constructs an approximate mathematical surrogate, known as the Metamodel of Optimal Prognosis (MOP). Then the evolutionary algorithm is applied directly to the MOP model rather than creating and validating designs using a finite element solver. Because calculating a design on the MOP takes only a fraction of a second, this approach drastically accelerates the discovery of the optimal Pareto front while maintaining sufficient prediction accuracy. Furthermore, this Meta-Model-Based Optimization approach provides flexibility in a way that once the MOP is generated, the fundamental optimization objectives and boundary constraints can be dynamically redefined. This allows for the immediate generation and analysis of entirely new optimal Pareto fronts in seconds, entirely skipping the need for additional FEA. These two distinct approaches of the evolutionary algorithm for this thesis study are detailed and compared in the subsequent sections.

4.3 Direct Optimization Approach

In this traditional computational approach, the evolutionary algorithm evaluates the fitness of every individual design by directly involving the ANSYS Maxwell 2D finite element solver. This method relies purely on raw simulations rather than statistical approximations, guaranteeing the highest level of electromagnetic accuracy for every evaluated generation, but at a significant computational cost. The optimization environment is initialized by importing the python automation script directly into the optiSLang optimization wizard, where the input variables along with their ranges are defined and output responses are chosen. The chosen input variables and their ranges for optimization are mentioned in the Table 10. The multidimensional design space is formally established by enabling nine specific active optimization parameters, which encompasses seven continuous geometric boundary ratios and two discrete winding variables namely, number of turns and number of parallel strands per coil. Concurrently, constant values are locked into the algorithm to define the baseline structural frame of the machine as shown in Table 11.

Respect to the experimental test setup capabilities, constraint boundaries are mathematically enforced using a rank-order method, heavily penalizing and rejecting any design combination that results in a phase RMS current exceeding 80 A or a required DC bus voltage exceeding 100 V. To systematically explore this complex global design space, Nature Inspired Optimization module within optiSLang is deployed using a custom configured evolutionary algorithm. The search strat-

Table 10: Optimization ranges and classification of design variables

Symbol	**Parameter Type**	**Range**
γ_{β_s}	Continuous	0.4 - 0.55
γ_R	Continuous	0.4 - 0.6
γ_S	Continuous	0.2 - 0.25
$R_{\text{outer taper}}$	Continuous	0.8 - 2.2
$R_{\text{tooth ratio}}$	Continuous	0.6 - 0.9
R_{thick}	Continuous	0.25 - 0.35
R_{f}	Continuous	0.6 - 0.8
n	Discrete	7,8,9,10,11,12,13,14
Strands	Discrete	1,2,3,4

Table 11: Fixed structural constants of the baseline machine frame

Description	**Values**
IRD	145 mm
OSD	180 mm
AG	0.5 mm
N	2500 rpm

egy is biased toward global exploration rather than local refinement. The evolutionary process begins with a starting population of 30 unique, randomly generated motor designs N_{samples}. Following this initial explanatory scatter, the core population size N_{pop} is reduced to 20 individuals per generation. The solver is constrained to a maximum of 14 evolutionary generations N_{gen} and a termination limit of 290 total finite element evaluations, ensuring the computational timeline remains manageable. A stagnation limit of 14 generations is also defined, meaning the algorithm will continue searching until the maximum evaluations are reached unless the Pareto front fails to improve. In optiSLang, the initial population is treated as the first generation; therefore, the maximum number of samples is computed as,

$$N_{\text{samples}} = N_{\text{start}} + (N_{\text{gen}} - 1)N_{\text{pop}} = 30 + (14 - 1)20 = 290. \tag{85}$$

The progression from one generation to the next is governed by defined mathematical evolutionary operators. To evaluate multi-objective success without requiring arbitrary weightings, the algorithm utilizes a Pareto dominance fitness method. To select the highest performing parents for reproduction, it applies a Pareto ranking system paired with tournament selection. A tournament size of 2 is used, meaning 2 designs are randomly drawn from the population and the superior design is selected for breeding. To preserve the optimal trade-offs discovered during the run, an external achieve size of 20 is maintained, permanently storing the best non-dominated solutions. During the recombination phase, the algorithm leverages a hybrid crossover strategy to generate offspring parameters. It assigns an equal 50% probability to both uniform crossover and simulated binary crossover, allowing the algorithm to dynamically choose how parent traits are mathematically blended. Finally, to actively prevent the population from experiencing genetic stagnation and becoming trapped in local optimums, a normally distributed mutation operator is applied with an 11% mutation rate. This ensures that a sufficient degree of random parameter variation is continuously introduced into the design pool, thereby forcing the algorithm to consistently explore various regions of the feasible design space.

Direct Optimization Results

Upon completion of the 290 finite element analyses, the Direct Optimization framework successfully evaluated all 290 distinct geometric and electrical permutations. The algorithm effectively navigated the mathematical boundaries, rejecting unfeasible combinations while systematically pushing the surviving population toward the limits of theoretical performance. The resultant 2D scatter plots in Figures 37 and 38 shows the emergence of a 2D Pareto optimal front, showing the inherent conflict between the established objectives. It should be noted that the optimization problem involves three conflicting objectives, while the presented plots show only two-dimensional projections of this multi-dimensional design space. As a result, these projections limit the visual continuity of the Pareto front, leading to a non-smooth and partially scattered appearance, since the influence of the third objective is not explicitly represented. Furthermore, the Pareto front is constructed from a limited number of FEA evaluations, and the presence of discrete design variables such as number of turns and strands, introduces additional discontinuities in the design space. Consequently, the resulting the resulting Pareto boundary appears irregular, reflecting the discrete and finite nature of the evaluated optimal solutions.

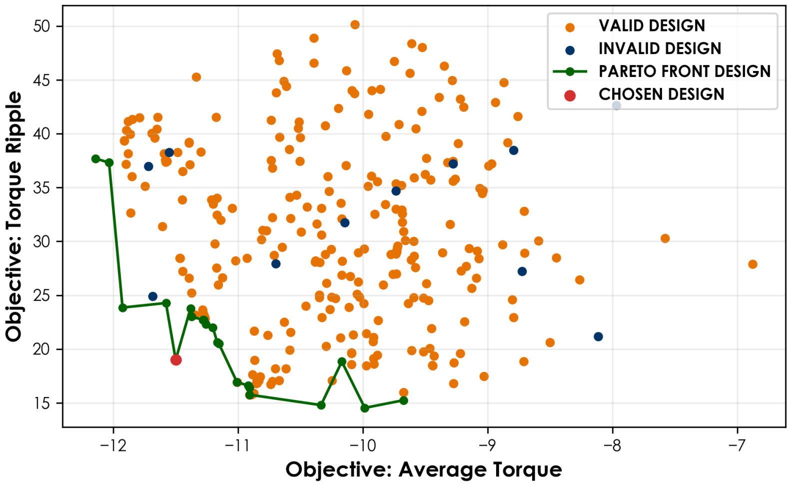

Figure 37: 2D Pareto front for average torque and ripple objectives

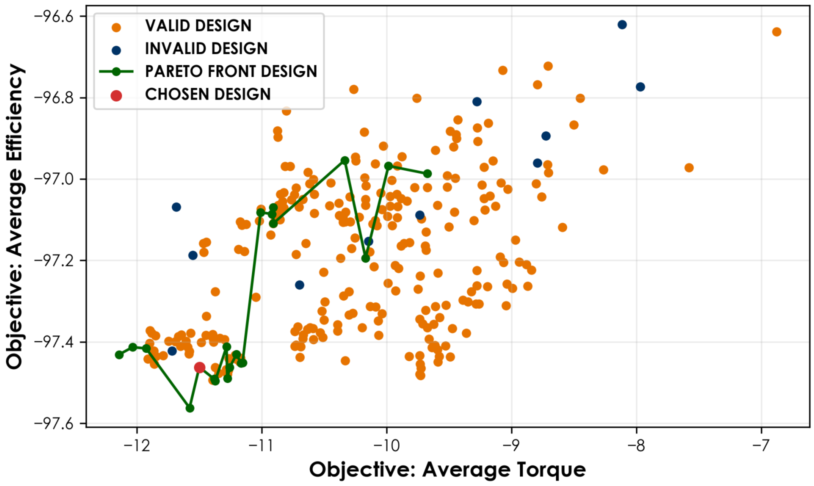

Figure 38: 2D Pareto front for average torque and efficiency objectives

Despite this, Figure 37 illustrates a direct correlation between the maximization of average electromagnetic torque and the increase in the transient torque ripple. Particularly, after 11 Nm, when average torque increases, the transient ripple also increases. The algorithm's distribution of evaluated designs proves that attempting to scale the torque density created problem with the smooth mechanical rotation of the machine in terms of increased ripple. This confirms that no single absolute maximum exists without a corresponding electromagnetic compromise. Furthermore, Figure 38 demonstrates clustering of highly efficient designs near the left bottom corner indicating that the algorithm identified specific geometric parameter combinations that minimize losses across varying torque outputs.

Table 12: Design variables for Design 144

Inputs	**Value**
γ_{β_s}	0.515
γ_R	0.563
γ_S	0.218
$R_{\text{outer taper}}$	0.911
$R_{\text{tooth ratio}}$	0.665
R_{thick}	0.289
R_f	0.798
n	10
Strands	4

Table 13: Performance outputs for Design 144

Outputs	**Value**
T_{avg}	11.5 Nm
T_{ripple}	19 %
P_{out}	3 kW
η_{avg}	~97.5 %
V_{DC}	88.5 V
$I_{\text{phase,rms}}$	31.8 A

From this diverse set of Pareto optimal solutions, a single optimal compromise had to be selected for the final comparison study. The selection process required identifying a design that offered a high mechanical power output while maintaining a stable, low torque ripple profile and remaining strictly within the designated experimental hardware limits. Based on a balanced evaluation of the multi-objective trade-offs, Design 144 was selected as the optimal global solution from the Direct Optimization approach. Design 144 represents a refined, mathematically balanced machine geometry whose corresponding input variable values and the output response values are presented in Tables 12 and 13. These output response values of Design 144 ensures that the improved design discovered by the Direct Optimization approach is not only theoretically performing but also entirely feasible to run within the existing test setup limits.

4.4 Meta-Model-Based Optimization Approach

Relying solely on the finite element solver as followed in the Direct Optimization approach imposes computational bottlenecks. A maximum budget of a few hundred simulations is often insufficient to fully map a highly dimensional, non-linear electromagnetic design space, increasing the risk of premature convergence on a localized optimum. To systematically overcome this sparse sampling and identify a global optimal Pareto front, a Meta-Model-Based Optimization is necessary. A meta-model, commonly referred to as a surrogate model, functions as a efficient mathematical approximation of the complex time intensive FEA. Instead of simulating every new geometric iteration through ANSYS Maxwell, the framework trains a statistical model to instantly predict the electromagnetic responses of the motor based on initial sample data. Once this mathematical surrogate is validated for accuracy, the evolutionary algorithm is applied directly to the surrogate model rather than running an FEA. This shift allows the optimizer to evaluate thousands of design iterations in seconds, exploring the boundaries of the design space without the intensive computational costs.

4.4.1 Sensitivity Analysis and Results

The foundational step in constructing a highly accurate predictive surrogate is performing a comprehensive sensitivity analysis (SA). SA is a statistical process that systematically investigates how variations in the input geometric and electrical parameters influence the target objective functions. This analytical phase is crucial for two primary reasons, the first reason is that it quantifies the relative importance of each design variable, allowing to identify and filter out influential parameters. This reduces the overall dimensionality of the problem and prevents the surrogate model from mathematically overfitting to simulation noise. Second, the discrete designs generated during the analysis serve as the Design of Experiments (DOE), providing the essential, foundational training dataset required to construct the predictive multidimensional surface of the meta-model.

Within ANSYS optiSLang environment, the sensitivity analysis is configured using an Advanced Latin Hypercube Sampling (ALHS) strategy. Unlike basic, random sampling methods, which can inadvertently cause data points to cluster and leave large regions of the design space entirely unexplored, ALHS guarantees a highly uniform, space filling distribution. It systematically divides the multidimensional space into equal intervals, ensuring that the entire functional range of every parameter is adequately represented in the training data. For this specific evaluation, the ALHS algorithm is allocated a maximum budget of 100 initial sample designs.

To maintain a direct comparative analysis with the previous Direct Optimization approach, the sensitivity study is done with the identical parameter boundaries as in the previous study. The sampling algorithm changes 9 active input variables, encompassing the continuous geometric ratios and discrete winding parameters while adhering to the established dimensional constants for the inner stator diameter, outer-rotor diameter and the air gap thickness. Unlike the Direct Optimization method, no objectives and constraints are setup during the sensitivity analysis. The primary goal of this study is the exploration of designs rather than performance optimization at this stage. Therefore, the algorithm simply calculates and records the output responses such as the average torque, operational efficiency, torque ripple, phase current and required DC bus voltage across the initial design samples. This unbiased, unconstrained data collection provides the training set necessary to construct the surrogate model required for Meta-Model-Based Optimization.

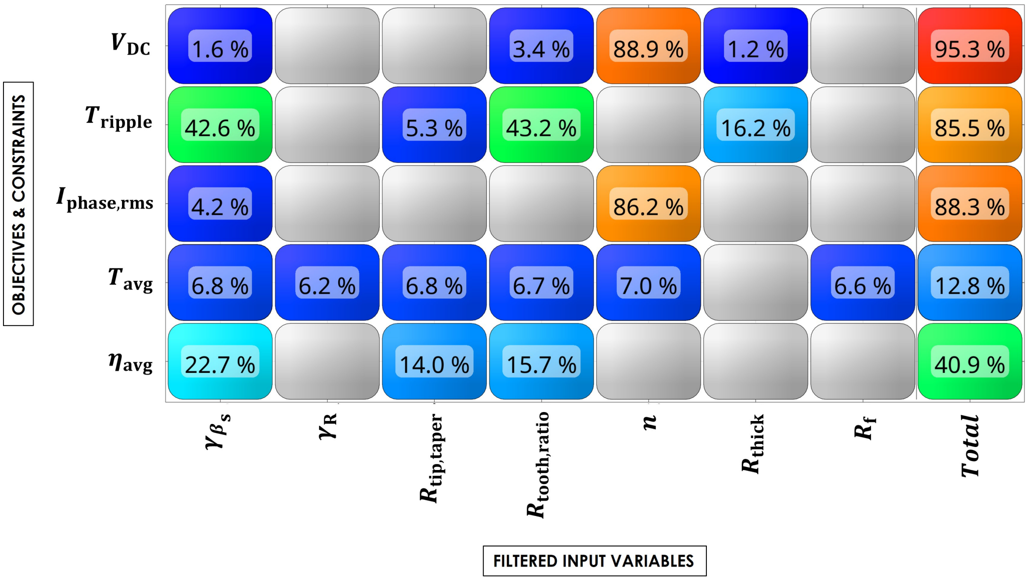

	γ_{β_s}	γ_R	$R_{tip,taper}$	$R_{tooth,ratio}$	n	R_{thick}	R_f	*Total*
V_{DC}	1.6 %			3.4 %	88.9 %	1.2 %		95.3 %
T_{ripple}	42.6 %		5.3 %	43.2 %		16.2 %		85.5 %
$I_{phase,rms}$	4.2 %				86.2 %			88.3 %
T_{avg}	6.8 %	6.2 %	6.8 %	6.7 %	7.0 %		6.6 %	12.8 %
η_{avg}	22.7 %		14.0 %	15.7 %				40.9 %

Figure 39: Coefficient of prognosis matrix

The study was performed and the surrogate model was mathematically constructed within the Advanced Metamodel of Optimal prognosis (AMOP) framework, which determines the best fit using a combination of Polynomial Regression, Moving Least Squares (MLS), and Isotropic Kriging.

After filtering out minor important parameters, it can be seen from the coefficient of prognosis (COP) matrix in Figure 39 that the output responses such as DC voltage and Phase current exhibit high predictability with COP values of 95.3% and 88.3% respectively. Both outputs are strongly dominated by the number of turns n, which contributes more than 80% to their evaluation. This indicates that the winding configuration play a major role in determining the electrical behavior of the machine. In contrast, torque ripple shows a different behavior with a high COP value of 85.5% but without a single dominant parameter. Instead, it is mainly influenced by $\gamma_{\beta_\mathrm{s}}$ and $R_{\mathrm{tooth,ratio}}$, each contributing approximately 40 to 45%.

The average torque exhibits a very low COP value of 12.8% indicating that the selected design parameters and their chosen ranges do not sufficiently explain its variation. The contribution from all parameters is relatively small and evenly distributed, suggesting that average torque is influenced by more complex nonlinear electromagnetic effects that are not fully captured in the parameter set. Similarly, the average efficiency shows a moderate COP value of 40.9%, with contributions distributed across multiple parameters such as $\gamma_{\beta_\mathrm{s}}$, $R_{\mathrm{tooth,ratio}}$, and $R_{\mathrm{tip,taper}}$. In addition, a moderately strong correlation was observed between average efficiency and average torque, suggesting improvements in torque lead to increase in efficiency.

4.4.2 Multi-Objective Trade-off Analysis

Despite the low predictive quality observed for the average electromagnetic torque and efficiency during the sensitivity analysis, the Meta-Model-Based Optimization was executed utilizing the generated surrogate model. This decision is justified as the surrogate model has high predictability for the critical electrical constraints and the transient torque ripple. By relying on these mathematical boundaries, the evolutionary algorithm can navigate the multidimensional space, discarding electrically unfeasible geometries and filtering for smooth mechanical operation with the least ripple values. The advantage of this approach is computational efficiency, by executing the search algorithm directly on the mathematical meta-models rather than invoking the physical finite element solver, the framework can evaluate thousands of discrete machine topologies in mere seconds.

To systematically perform this multi-objective exploration, the framework was configured to evaluate the surrogate responses against the exact performance criteria established in the previous Direct Optimization study. Consistent with the Direct Optimization approach, the run was driven by three simultaneous and inherently conflicting objectives which are maximization of the average torque, the maximization of operational efficiency, and the minimization of transient torque ripple. Concurrently, the operational viability of every evaluated design was mathematically enforced using an identical experimental test setup constraint. Any geometric combination that violated these electrical constraints was immediately penalized by the algorithm's rank order constraint handling, ensuring the optimizer focused on practically drivable solutions, just as it did during the previous study's FEA evaluations.

The optimization process was run by the evolutionary algorithm, configured to execute a global search strategy across the identical 9-dimensional parameter space, encompassing the same 7 continuous geometric boundary ratio and two discrete winding variables while respecting the same locked structural constants utilized previously. However, the sheer computational scale vastly differed. While the Direct Optimization approach was computationally restricted to a termination limit of 290 total evaluations, the Meta-Model-Based Optimization framework was allocated a massive budget of 5000 surrogate evaluations. Similar to the core population structure of the Direct Optimization method, the evolutionary process maintained a constant active population size of 20 discrete machine designs throughout the run. The framework was permitted to evolve over a maximum span of 250 generations and utilized a stagnation limit, cleanly terminating the process if the Pareto front failed to improve for 20 consecutive generations.

To continuously improve the quality of the machine designs, the algorithm mirrored the mathematical evolutionary operators defined in the Direct Optimization approach. It utilized a Pareto dominance fitness method to evaluate multi-objective success and selected parent geometries using a Pareto ranking system paired with a tournament size of 2. The creation of new offspring was governed by the same hybrid crossover strategy, assigning an equal 50% probability to both uniform and simulated binary crossover methods to dynamically blend parent traits. Finally, to actively prevent mutation rate closely aligning with the 11% utilized in the Direct Optimization approach and a fixed standard deviation of 0.1. Through these consistent, biologically inspired mechanisms, the algorithm rapidly mapped the global Pareto front shown in Figures 40 and 41, allowing for a direct mathematically sound comparison against the traditional optimization methodology.

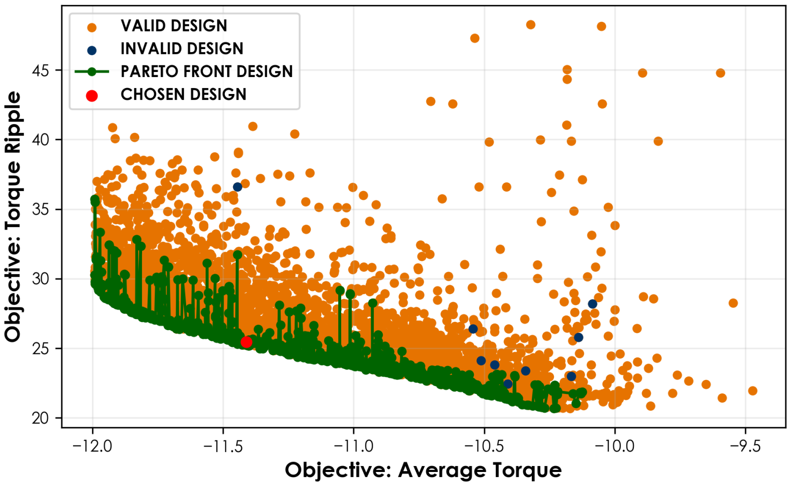

Figure 40: 2D Pareto front for average torque and ripple objectives

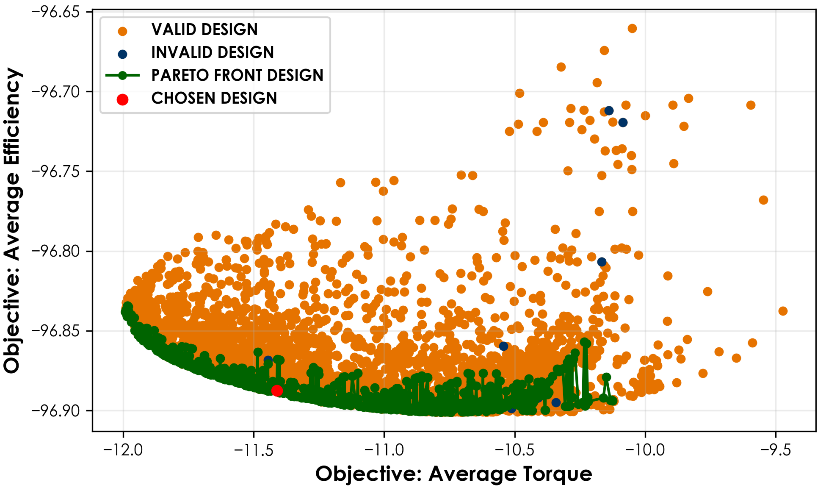

Figure 41: 2D Pareto front for average torque and efficiency objectives

The algorithm had explored spaces and from the results, it can be seen in Figures 40 and 41 that as average torque increases beyond 10.5 Nm, the efficiency decreases gradually with steep increase in torque ripple. In order to validate the theoretical results, an automated validator system is added to the corresponding optimization node within the OptiSLang environment to strategically filter the optimal designs from the generated Pareto front. These filtered design geometries are then automatically evaluated using the ANSYS Maxwell 2D finite element solver.

4.4.3 Optimization Results and Model Validation

Eight final designs were filtered and validated by the finite element solver. The result from the filtered designs were compared with the corresponding surrogate models predictions and presented in the Tables 14 and 15.

Table 14: Comparison of FEA validation results and surrogate model predictions for average efficiency, average torque, and torque ripple of selected Pareto-optimal designs (percentage error with respect to FEA results)

Design	**Efficiency (%)**			**Torque (Nm)**			**Ripple (%)**		
	FEA	**Surrogate**	**Error**	**FEA**	**Surrogate**	**Error**	**FEA**	**Surrogate**	**Error**
1	97.294	96.877	-0.43%	9.333	10.679	14.42%	14.648	22.604	54.31%
2	97.156	96.894	-0.27%	9.492	10.125	6.67%	15.520	21.882	40.99%
3	97.338	96.887	-0.46%	10.801	11.411	5.65%	16.033	25.455	58.77%
4	97.309	96.834	-0.49%	9.133	11.983	31.21%	27.529	29.556	7.36%
5	97.278	96.866	-0.42%	9.498	11.830	24.56%	29.868	32.839	9.95%
6	97.241	96.857	-0.39%	9.552	10.233	7.13%	13.691	20.688	51.10%
7	97.320	96.900	-0.43%	9.815	10.928	11.34%	23.718	28.250	19.11%
8	97.281	96.888	-0.40%	9.578	11.446	19.50%	27.869	31.731	13.86%

Table 15: Comparison of FEA validation results and surrogate model predictions for phase RMS current and DC-link voltage of selected Pareto-optimal designs (percentage error with respect to FEA results)

Design	I_{rms} **(A)**			V_{dc} **(V)**		
	FEA	**Surrogate**	**Error**	**FEA**	**Surrogate**	**Error**
1	23.350	25.859	10.74%	86.444	90.335	4.50%
2	23.350	25.551	9.43%	88.045	91.069	3.43%
3	27.402	26.193	-4.41%	92.375	88.750	-3.92%
4	23.350	26.824	14.88%	83.834	87.401	4.25%
5	23.835	26.518	11.25%	85.830	90.519	5.46%
6	23.835	25.504	7.00%	91.076	92.493	1.56%
7	23.835	25.878	8.57%	89.440	93.414	4.44%
8	23.835	26.248	10.12%	88.472	92.873	4.97%

$$\text{Error (\%)} = \frac{\text{Surrogate} - \text{FEA}}{\text{FEA}} \times 100 \tag{86}$$

This comparison indicates that while the surrogate model successfully captures the overall trends, there are noticeable quantitative deviations present across the performance metrics. These deviations are consistent with the findings of the sensitivity analysis. The efficiency prediction show relatively good agreement, with deviations generally within 0.3 to 0.5%, which aligns with its moderate COP value of 40.9% indicating that the surrogate model captures its behavior with reasonable accuracy. In contrast, the average torque is consistently overestimated by the surrogate model across all designs, with deviations exceeding 2 Nm in some cases. This behavior directly reflects its very low COP value of 12.8% confirming that the selected input variables do not sufficiently explain its variation. Similarly, the phase RMS current and the DC voltage which exhibited high COP values of 88.3% and 95.3% respectively, show comparatively smaller and more consistent deviations, validating the strong predictive capability of the surrogate model for electrically constrained quantities. Torque ripple despite having a high COP value of 85.5% is systematically overestimated by the surrogate model. However since its behavior is influenced by multiple parameters rather than a single dominant variable, the surrogate model is still able to preserve the relative ranking of designs.

Overall the validation results confirm that the predictive accuracy of the surrogate model is correlated with the sensitivity analysis results. Outputs with high COP values demonstrate reliable prediction, whereas those with low COP values, particularly average torque exhibit larger deviations. Despite these limitations, the surrogate model remains effective for rapid exploration of the design space and identification of promising candidate solutions. The final FEA validation step is therefore essential to ensure physically accurate performance evaluation, resulting in a robust optimization framework that combines computational efficiency with high accuracy.

Utilizing the same methodology as in Parametric Optimization to find the improved design by applying equal weights to the normalized FEA values of average efficiency, average torque, and torque ripple, Design 3 was identified as the improved overall solution among the validated candidates from Meta-Model-Based Optimization. This design achieved the highest combined score due to its superior torque and efficiency while maintaining an acceptable low ripple level relative to the other candidates.

Table 16: Comparative analysis of performance metrics across baseline and improved designs

Outputs	**Base Design**	**Parametric Sweep Design**	**Direct Optimization Design**	**Meta-Model-Based Optimization Design**
T_{avg}	7.7 Nm	8.97 Nm	11.5 Nm	10.8 Nm
T_{ripple}	57 %	33 %	19 %	16 %
P_{out}	2 kW	2.35 kW	3 kW	2.83 kW
η_{avg}	96.5 %	97 %	~97.5 %	~97.3 %
V_{DC}	54.6 V	67.3 V	88.5 V	~92.4 V
$I_{\text{phase,rms}}$	26.3 A	26.3 A	31.8 A	27.4 A

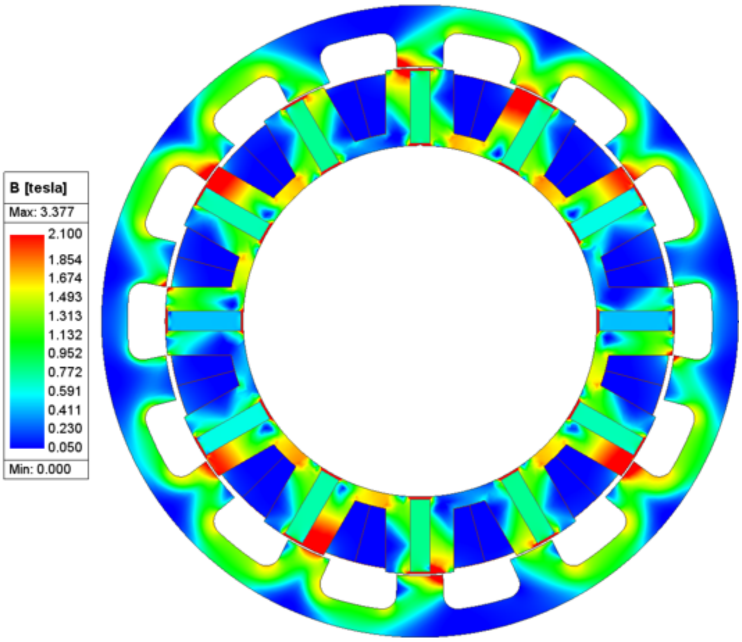

Figure 42: Magnetic flux density distribution of the selected Direct Optimization design

From the comparison shown in Table 16, the Meta-Model-Based optimized design offers the best overall performance when equal importance is given to average torque, average efficiency and torque ripple. However, the Direct Optimization design delivers the highest torque and power output, making it the preferred candidate for further 3D FEA validation. To further examine the electromagnetic behavior of the selected Direct Optimization design, the magnetic flux density distribution of the optimized 2D model is evaluated, as shown in Figure 42. The contour plot provides additional physical insight into the utilization of the active iron regions after optimization. The flux density is concentrated mainly in the stator iron bridges, stator teeth, rotor teeth, and air-gap region, where electromagnetic energy conversion is dominant. However, certain regions of the rotor yoke exhibit comparatively low flux density, indicating that these sections are not fully utilized magnetically. This suggests that although the Direct Optimization design provides the highest torque and output power among the investigated designs, there remains scope for further material reduction or geometric refinement in the low-flux rotor regions.

To visualize the geometric differences in the 2D cross-section, the finalized designs from each optimization method, along with the 2D base model are presented in Figure 43.

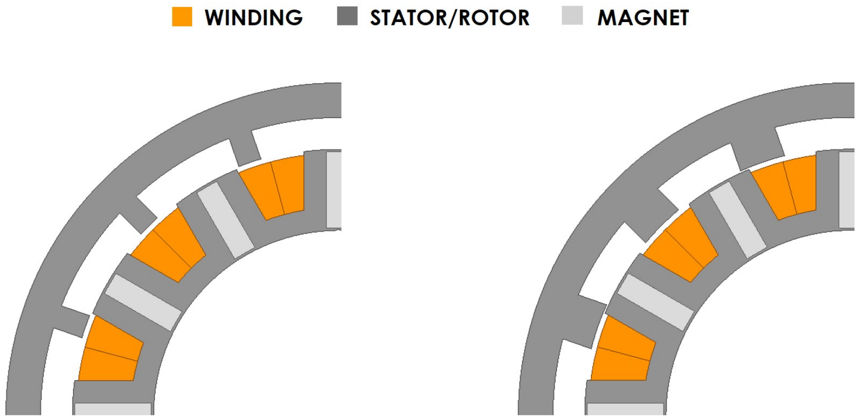

Base design

Parametric sweep design

Direct optimization design

Meta-model optimization design

Figure 43: Comparison of improved designs with the base design

4.5 Comparison of Optimization Approaches

The three optimization approaches executed in this study demonstrates distinct characteristics in terms of computational efficiency, solution quality, and applicability to complex design problems. Parametric Sweep Optimization represents the most straightforward method involving systematic variation of design variables within predefined ranges. Its primary advantage lies in its simplicity and transparency, allowing clear visualization of the relationship between input variables and performance metrics. This method is particularly effective for preliminary design exploration, where the objective is to understand the influence of individual parameters. However, its major limitation is the exponential growth in computational cost with increasing dimensionality. For problems involving multiple variables, such as FSPM machine design, parametric sweeps become computationally infeasible and inefficient in identifying global optima.

Direct Optimization implemented using evolutionary algorithms offers a powerful alternative capable for handling nonlinear and multi-objective problems. This approach directly interacts with the FEA model, enabling evaluation of design candidates without approximation. It is particularly well-suited for problems with strong parameter coupling. The ability to generate Pareto fronts provides valuable insight into trade-offs between competing objectives. However, the primary drawback of Direct Optimization is its high computational demand, as it requires a large number of finite element analyses. This makes it time-intensive, especially when detailed models are used. Meta-Model-Based Optimization addresses the computational limitations of Direct Optimization by introducing surrogate models that approximate the relationship between input variables and performance outputs. Techniques such as ALHS are used to construct these models based on a limited set of FEA simulations. The key advantage of this approach is its significant reduction in computational cost while still enabling efficient exploration of the design space. Additionally, sensitivity analysis was integrated to identify the most influenced variables, further improving optimization efficiency. However, the accuracy of the results depends on the quality of the surrogate model, and errors may arise if the model fails to capture nonlinear behaviors. From this study, it is understood that Parametric Sweep Optimization is preferred during the initial design phase for finding critical input variables, understanding system behavior and validating model setup. Direct Optimization is most suitable when high accuracy is required and computational resources are available, particularly for final design refinement. Meta-Model-Based Optimization is preferred for complex multi-objective problems where computational efficiency is critical, offering a practical balance between accuracy and speed.

5 3D Electromagnetic Modeling and Analysis

The extensive multi-objective optimization approaches detailed in the chapter 4 identified a refined machine geometry capable of meeting the desired performance criteria. However, both the Direct and Meta-Model-Based Optimizations were executed with the 2D FEA. R. De Weerdt et al. [53] identified that 2D FEA studies assumes an infinite axial length for mathematical calculation and this caused the 2D planar models to confine the magnetic flux density vectors to radial and tangential components. This fundamentally neglects 3D electromagnetic phenomena such as the axial fringing flux escaping at the physical boundaries of the core. Furthermore, the 2D models do not include end windings in simulations. S. T. Lundmark et al. [54] states that failing to include end windings in simulation models underestimates stator leakage inductance, which can yield prediction failures. Hence, their study [54] concludes that 3D FEA is considered an suitable option for theoretically determining stator winding inductances and comprehensively capturing these complex spatial end effects. Beyond structural and end winding effects, 3D modeling is also necessary to compute the eddy current losses induced within the permanent magnets. Because planar 2D solvers force induced currents to flow in the infinite axial direction, they inherently limited to capture the complex, three-dimensional circulation paths, particularly the end winding loops, leading to underestimations of localized magnet heating. Therefore, while 2D FEA provides a preliminary approximation, this transition to a comprehensive 3D electromagnetic analysis is necessary to evaluate the selected design and predict its physical performance prior to prototype manufacturing.

5.1 Model Configuration and Mesh Generation

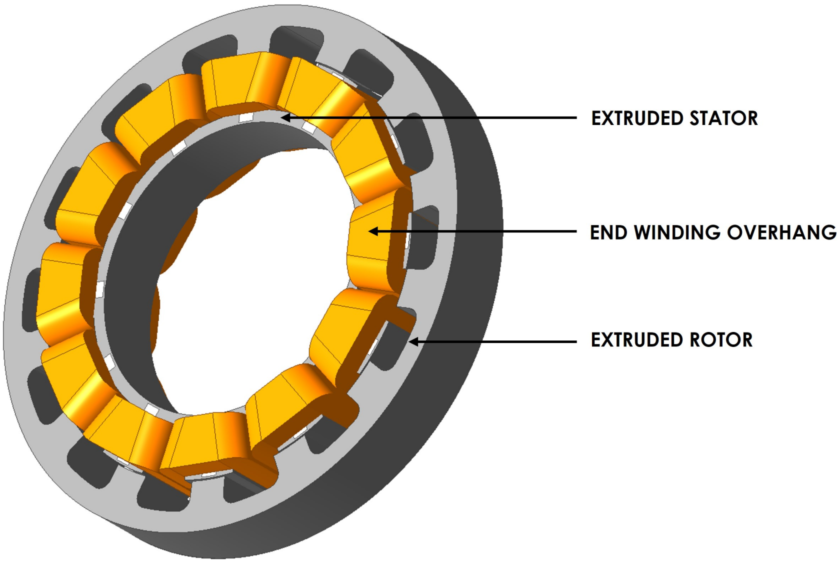

Figure 44: 3D finite element model of the chosen 2D design

The transition from the 2D design to a 3D simulation model requires defining the axial boundaries and the end winding connections. To significantly reduce the computational time associated with 3D simulation, geometric symmetry was strategically exploited during the model configuration.

Rather than simulating the full 25mm stack length, the optimal cross-sectional geometry was extruded to exactly half of the active stack length (12.5mm). The most critical geometric addition to the 3D model is the definition of the end windings. The constructed 3D model prior to the application of symmetry reduction for 3D FEA is shown in Figure 44.

Furthermore, executing 3D FEA requires significantly complex meshing. Unlike 2D mesh, which only consists of planar triangles, 3D mesh utilizes thousands of volumetric tetrahedrons. Applying a uniformly dense mesh across the entire three-dimensional space would result in an exponentially high mesh elements, making the simulation unsolvable in a reasonable time frame. Therefore, components targeted meshing was implemented, directly assigning specific maximum element length to individual physical components and constructed boundary regions based on their electromagnetic significance, similar to the mesh configuration used in ANSYS benchmark models from the example library. The mesh configuration assigned for specific components are listed in Table 17.

Table 17: 3D FEA mesh configuration

Mesh Types	**Magnets**	**Copper Windings**	**Electrical Steel**	**Vacuum**
Element Size	6 mm	7 mm	6 mm	Adaptive Meshing
Surface Approximation	SD = 0.037; ND = 30°	ND = 30°	SD = 0.06; ND = 30°	
Surface Representation Priority	Normal	Normal	Normal	

**SD: Surface Deviation* **ND: Normal Deviation*

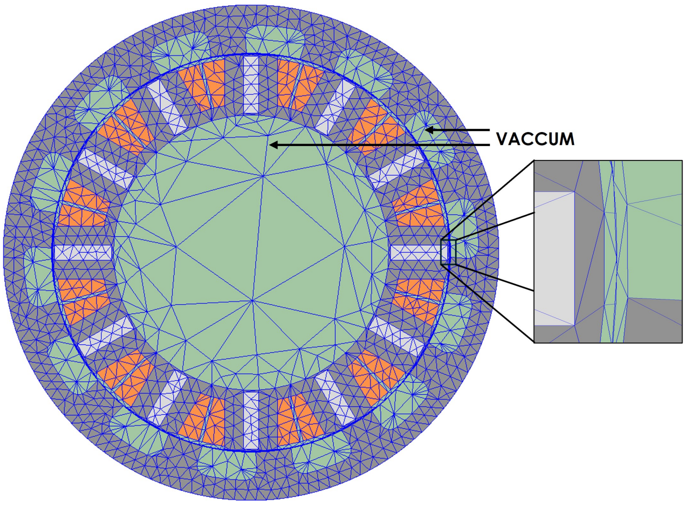

Figure 45: 2D cross-section of the 3D meshed geometry showing a cut section of the air-gap region in the XY-plane

To manage the surrounding air and non-actives spaces, a nested regional strategy utilizing mathematically defined boundaries was deployed. The global computational domain is defined by an outer region, configured as a large encompassing cylinder. Rather than applying strict manual mesh constraints, the mesh configuration inside this region relies on the solver's automatic adaptive meshing algorithm. Because the magnetic leakage flux decays in the air space far from the active machine, the solver generates a highly relaxed coarse mesh in this region as shown in Figure 45, significantly reducing unnecessary computational overhead. Conversely, an inner region, modeled as a hollow cylinder enclosing the rotor structure was also established. The most critical aspect of the 3D meshing is the configuration of the motion boundary, which mathematically separates the stationary stator domain from the rotating rotor domain. This was achieved by defining a motion band, constructed as a hollow cylinder nested between the stator bore and inner region.

A specific 'cylindrical gap treatment' mesh was applied to this boundary. This specialized meshing operation ensures that the tetrahedral elements on the rotating inner face align with the elements on the stationary outer face during every simulated transient time step. This mathematical treatment is vital for preventing artificial numerical noise and interpolation errors from corrupting the calculation of the transient torque ripple as the three-dimensional mesh physically slides across the air-gap interface.

Beyond spatial discretization, a major highlight of the 3D simulation is the effective calculation of magnetic losses, particularly the eddy currents induced within the permanent magnets. To capture these complex three-dimensional circulating currents, the eddy effect computation must be explicitly enabled with in the core solver settings. Crucially, all individual magnets must be manually selected and assigned an 'insulating' boundary condition. This electrical isolation prevents the solver from calculating artificial current paths between adjacent components, ensuring that the induced eddy currents circulate within the geometric volume of each discrete magnet.

5.2 3D Electromagnetic Performance Results

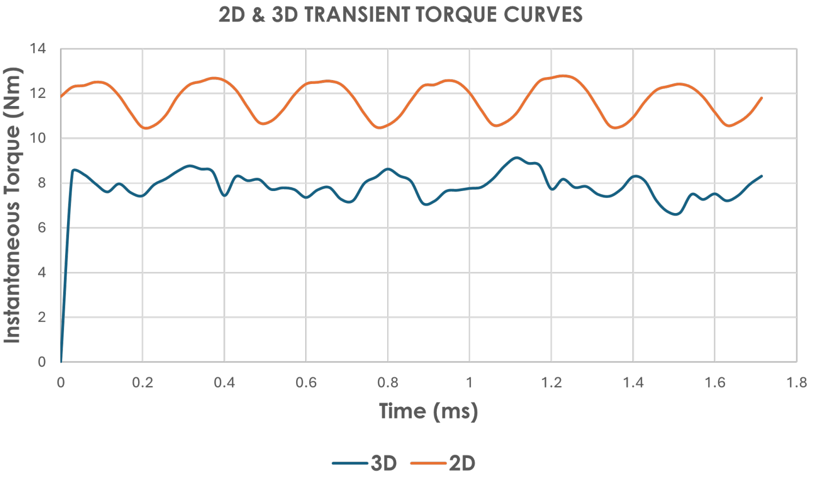

Figure 46: Comparison of 2D and 3D transient torque curves

Table 18: Comparison of 2D and 3D electromagnetic results

Outputs	2D Model	3D Model
T_{avg}	11.5 Nm	8 Nm
T_{ripple}	19 %	36.4 %
P_{out}	3 kW	2.1 kW
η_{avg}	~97.5 %	92.4 %
V_{DC}	88.5 V	89.6 V
$I_{\text{phase,rms}}$	31.8 A	31.8 A
P_{magnet}	-	11.4 W

Table 18 shows the comparison in performance outputs between 2D and 3D analyses. The transition from 2D to 3D FEA results in significant performance metrics change, highlighting the limitations of 2D approximations. Since 2D simulations assume an infinite axial length, they neglect axial fringing and end-winding flux leakages. As a result of this, 3D analysis shows a reduction in average electromagnetic torque, dropping by nearly 30% from 11.43 Nm in 2D to 8 Nm in 3D. The plots of instantaneous torque from both 2D and 3D FEA are shown in Figure 46. With the operating speed remaining constant, the 30% drop in torque brings down the output mechanical power from 3 kW to 2.1 kW. This reduction occurs due to the flux leaking through the end windings rather than linking the poles for torque production. The smooth, periodic torque waveform simulated in 2D becomes distorted in the 3D simulation as torque ripple nearly doubles from 19% to 36.4%. This can be attributed to the localized magnetic saturation well exceeding 2.1 T in the stator teeth, structural bridges, and rotor poles as shown in the Figure 47. Operating in this nonlinear saturation region increases magnetic reluctance, leading to higher flux leakages.

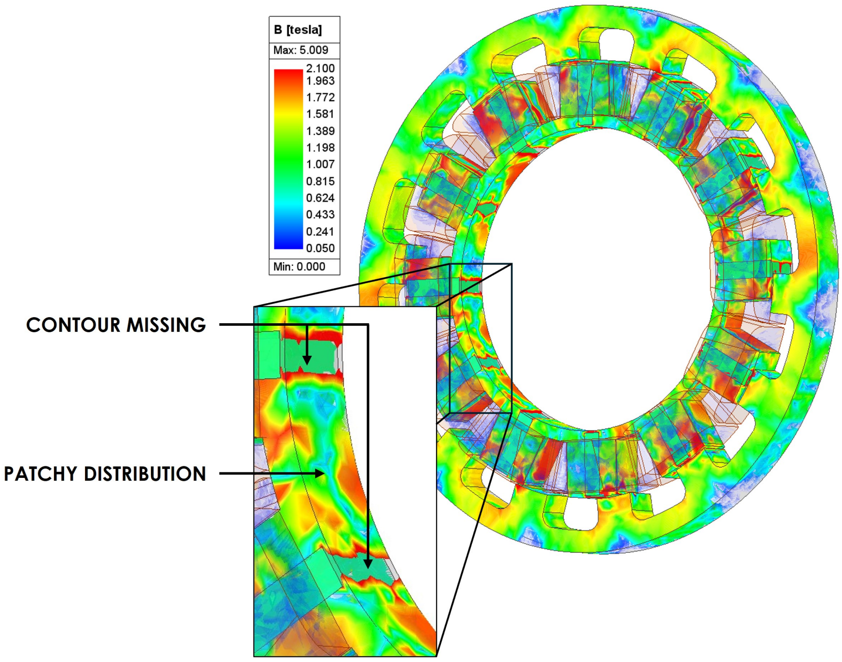

Figure 47: Magnetic flux density contour plot

This comparison has shown that the overall efficiency has dropped to 92.4 % from 97%. While the copper losses remain identical due to constant phase currents, the core losses surged to a 4.7X increase from 20 W to 94.5 W. This increase is attributed to the three-dimensional flux paths, which introduce localized flux variations that are not captured in 2D simulations. Furthermore, the eddy current losses in magnets have been computed to be 11.4 W. These losses arise due to the circulating current paths within the magnet volume, which cannot be represented in 2D analysis. It is important to note that the deviations observed between 2D and 3D results are not unique to this study. Similar trends have been observed in the benchmark models provided within the ANSYS Maxwell example library, where identical machine geometries exhibit noticeable reductions in torque and efficiency when analyzed using 3D FEA. Compared to the refined and structured mesh employed in 2D simulations, the 3D model utilizes a tetrahedral mesh with relatively coarser element sizing due to computational constraints. In particular, the absence of a refined air-gap mesh configuration such as dual air-gap band strategy implemented in the 2D model may introduce the localized inaccuracies in the flux density distribution and contribute to the irregularities observed in the contour plots. However, these meshing effects are secondary and do not significantly alter the overall performance trends observed in 3D. In conclusion, while 2D FEA serves as an efficient tool for preliminary design and optimization, it does not fully capture machine performance by neglecting critical 3D-effects. In contrast, 3D FEA provides a realistic representation of electromagnetic behavior by capturing end effects, saturation and magnet eddy current losses. However, careful attention must be given to mesh configuration to ensure numerical accuracy and reliable results.

6 Mechanical and Manufacturing Design

The transition from theoretical electromagnetic optimization to physical manufacturing requires a robust mechanical design strategy. The primary objective of this design phase is not to engineer a completely novel structural housing, but rather to strategically integrate the newly optimized electromagnetic topology with the pre-existing components from the Hacker Q150 motor. Figure 48 shows the 3D model of the Hacker Q150 motor. By dismantling the critical structural components from the Hacker Q150 specifically the stator bracket, bearings, and the rotor shaft, the newly designed machine can be seamlessly mounted into the existing test bench setup. This approach provides physical compatibility for experimental testing while drastically reducing custom machining costs and assembly complexity. Consequently, this chapter details the 3D mechanical modeling required to adapt the optimized active components to the Hacker motor's structural components, alongside the preparation of production-ready technical drawings and physical mock-ups for verification.

Figure 48: CAD rendering of the Hacker Q150 motor

6.1 3D Mechanical Modeling

The mechanical development and assembly were executed within the Siemens NX computer-aided design (CAD) software. The optimal 2D stator and rotor cross-sections finalized during the optimization phase were exported from ANSYS Maxwell as DXF files. These profiles were imported into Siemens NX and extruded to a stack length of 25 mm to create the 3D active solid bodies. The new rotor housing geometry was specifically adapted to interface securely with the existing shaft, while the stator laminations were dimensioned and provided additional projections to mount into the original Hacker stator bracket. A critical aspect of this assembly is to mechanically verify that the air gap of 0.5 mm is strictly enforced between the new active components, ensuring the physical prototype closely aligns with the design parameters used in simulations.

The construction of the machine within the Siemens NX environment was systematically categorized into three distinct mechanical sub-assemblies: the shaft assembly, the stator assembly, and the rotor assembly. The shaft assembly forms the rotational foundation of the machine, consisting entirely of the unmodified components from the Hacker motor, specifically the main drive shaft,

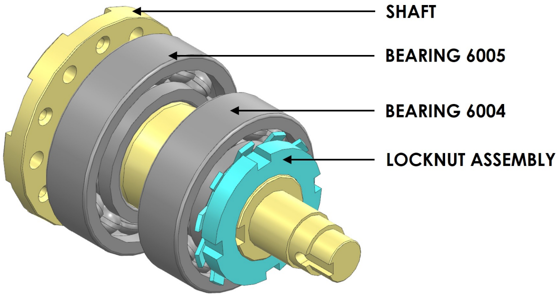

Figure 49: Shaft assembly showing the unmodified Hacker Q150 components

two primary support bearings 6005 and 6004, and the locknut assembly as shown in Figure 49. The locknut assembly ensure the bearing position relative to stator bracket. The remaining two assemblies were designed to integrate the newly optimized electromagnetic cores.

6.1.1 Stator Assembly

The stator assembly illustrated in Figure 50 integrates the newly designed stator core, permanent magnets, and copper windings with the pre-existing stator bracket, twist protection, and axial clamping components. To ensure mechanical stability under high electromagnetic torque, specific securing mechanisms existing in the Hacker motor were adapted into this new model.

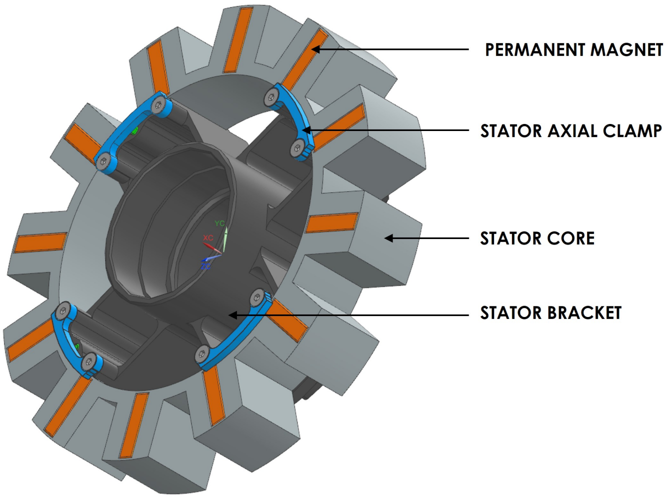

Figure 50: Stator assembly of the machine

To prevent any rotational movement of the stator core during operation, a stator twist protection system was implemented. This utilizes four numbers of ∅3 mm × 24 mm cylindrical pins that physically lock the stator into the corresponding recesses of the stator bracket and the core, thereby acting as a rigid anti-rotation key. Such axial projections shown in orange color in Figure 51 were provided at four different places on the inner circumference of the stator core exactly 90° apart. Furthermore, to prevent the stator core from migrating axially out of the bracket, a compressive retention system from the Hacker motor was also utilized. Once the coil-wound stator core is seated within the bracket, four mechanical clamps from the Hacker motor are positioned over the assembly and securely bolted to the bracket. These clamps apply a continuous axial compression shown as interference in Figure 52, preventing axial movement. In the electrical context, to prevent short circuits between the same phase windings strands or with the stator core due to insulation damage under high thermal loads, the copper conductors coated with dielectric should be utilized. Different insulation class offers different maximum operating temperature. Modified polyester resins categorized as standard Class F insulation allow for continuous operation up to 155°C. This

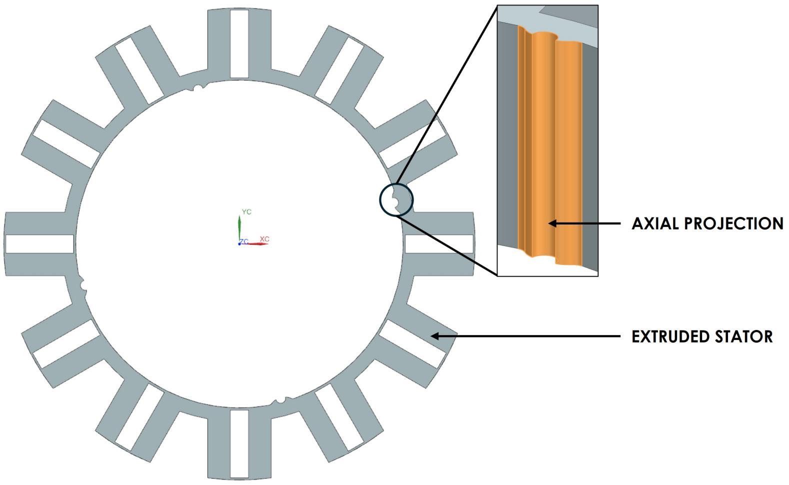

Figure 51: Stator core with axial projections

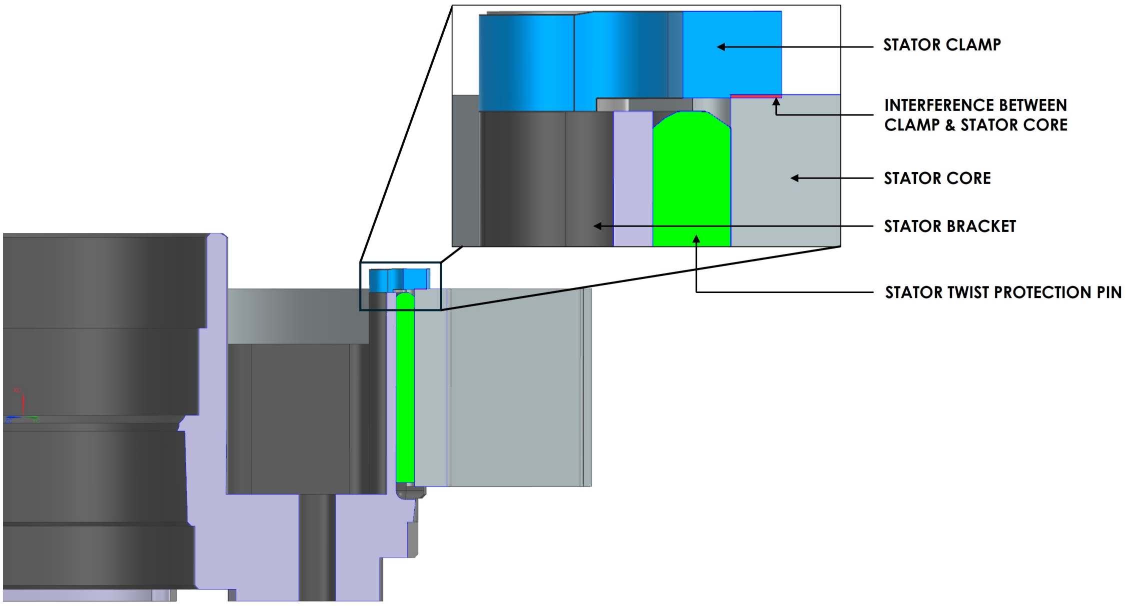

Figure 52: Clamping arrangement from the Hacker Q150 motor shown in sectional view

thermal limit can be further increased to 180°C by using Class H polyamide-imide enamels. This increase in thermal limit directly helps in increasing the allowable current supplied to the motor without the risk of thermal breakdown.

6.1.2 Rotor Assembly

The rotor assembly shown in Figure 53 involves a precise, shrinkage-fit assisted integration between the rotor core and a custom-designed outer-rotor housing machined from 6061-T6 aluminum alloy. Both the outer diameter of the rotor core and the inner diameter of the outer-rotor housing have a nominal dimension of 180 mm. To securely mate these two components without inducing radial compressive stress on the electrical steel laminations, a specialized pinned interference fit was engineered. The design features seven semicircular slots of ⌀3 mm × 25 mm machined along the boundary interface. Crucially, the pitch circle diameter (PCD) of the slots on the aluminum housing is intentionally offset to 179.9 mm, while the corresponding slots on the rotor core maintain a PCD of 180 mm. During the proposed heat shrink assembly process, the aluminum housing will be heated in an industrial oven to induce thermal expansion, allowing the rotor core to be inserted into it with zero interference. Subsequently, cylindrical retaining pins will be inserted into the aligned circular gaps. As the 6061-T6 aluminum cools and naturally contracts, the 0.1 mm PCD offset ensures that the thermal shrinkage force clamps onto the inserted pins rather than crushing the outer diameter of the rotor core. This mechanism transforms the pins into robust shear keys, establishing a high-strength lock between the core and the housing that can withstand the dynamic operational torque of the machine.

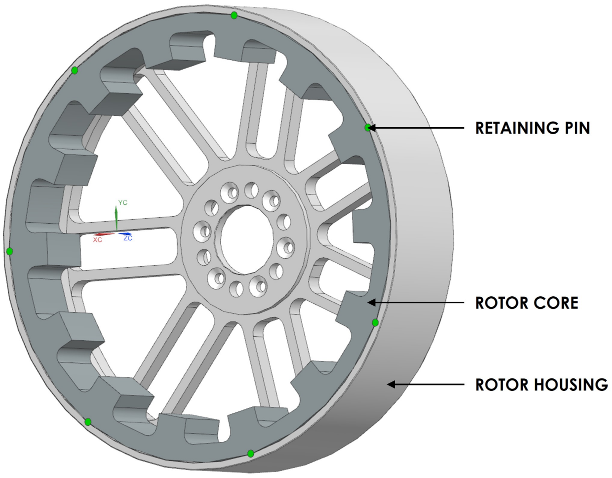

Figure 53: Rotor assembly of the machine

6.1.3 3D Mock-up Creation and Assessment

Final assembled outer-rotor FSPM motor developed for this thesis study is shown in Figure 54. It consists of components listed in Table 19 , which are organized into three distinct sub-assemblies for mechanical integration.

Figure 54: CAD rendering (left) and 3D printed mock-up (right) of prototype FSM machine developed in this study

Following the mechanical assembly in the CAD environment, a full-scale 3D printed mock-up model of the entire motor assembly was created to validate the design physically. The purpose of this mock-up was not to achieve exact manufacturing tolerances, which are difficult with standard 3D printing, but to verify whether the components assemble properly without major geometric errors. The mock-up preparation and assembly were also used for the initial validation of the stator, rotor, and housing integration. Additionally, the 3D printed stator was used to perform manual winding trials on two adjacent teeth using the intended winding configuration to assess the feasibility of achieving the desired slot fill factor of 50%. It was observed that manual winding at such a high fill factor is quite challenging. A key issue identified during this process was related to the end winding overhang length. In the planned mechanical design, a clearance of 10.45 mm was maintained between the top plane of the stator core and the bottom surface of the rotating rotor housing rib.

Table 19: Components used in the machine assembly with origin classification

Assembly Type	**Part Name**	**Quantity**	**Origin**
Shaft Assembly	Shaft	1	H Q150
	Bearing 6004	1	H Q150
	Bearing 6005	1	H Q150
	Locknut	1	H Q150
Stator Assembly	Stator bracket	1	H Q150
	Stator core	1	Designed
	Magnets	12	Designed
	3-phase copper windings	12	Designed
	Twist protection pins	4	H Q150
	Axial clamps	4	H Q150
	Clamp screws	8	H Q150
Rotor Assembly	Rotor housing	1	Designed
	Rotor core	1	Designed
	Shrink fit pins	7	Designed
	Housing to shaft assembly screws	6	H Q150

However, during manual winding, the overhang length reached approximately 11 mm, which would result in interference with the rotor housing. Based on this observation, it was decided to outsource the winding process for machine-assisted winding to ensure better control and maintain the overhang length below 8 mm. Furthermore, the mock-up assembly highlighted the need for a dedicated guiding system for the shrink fit process. Specifically, a mechanism is required to guide the rotor into the heated rotor housing and to assist in inserting the shrink fit pins, as the time available for completing the assembly is very limited. It was also confirmed, as initially anticipated, that the star point connection must be positioned on the rear side of the machine due to limited space on the top side. Other than these concerns, the axial projections created on the stator core inner diameter for twist protection, and the clamping arrangement of the core fit properly as intended. Overall, the 3D mock-up study identified practical manufacturing and assembly challenges before proceeding to the final prototype.

6.2 Preparation of Technical Drawings

Following the mechanical assembly in Siemens NX, comprehensive 2D technical drawings were created to facilitate the physical manufacturing of the steel laminations, magnets and rotor housing. These production drawings serve as the definitive communications tool for fabrication, detailing the exact geometric dimensioning and tolerancing (GD&T) required for the cutting process. The most critical geometric parameters, specifically the ISO fit tolerances governing the structural interfaces and the precise dimensional offsets for the thermal assembly, are summarized in Table 20.

Special attention was dedicated to the ISO tolerance classes at these specific mechanical interfaces to ensure that the final manufactured active components assemble smoothly with the Hacker motor parts. The specification of an H7/h6 sliding fit for the 180 mm outer-rotor boundary ensures that the core can be precisely seated within the housing prior to the shrink fit process. The complete, production-ready manufacturing drawings including material specifications and geometric tolerances for all sub-assemblies are provided in Appendices E, F, G, and H. The assembly procedure for the machine developed in this thesis study is provided in Appendix I.

Table 20: Summary of mechanical interface tolerances and ISO fit classes

Mechanical Interface	**Nom. Dia. (mm)**	**ISO Fit**	**Component Type**	**Tol. Limits (mm)**	**Dimensions (mm)**
Outer-Rotor Housing / Rotor Core	180	H8 / h8	Housing (Hole)	+0.063 / 0.000	180 / 180.063
			Core (Shaft)	0.000 / -0.063	179.937 / 180
Rotor Slot PCD offset	180	Shrink Fit	Housing Slots	-	179.9 (offset)
			Core Slots	-	180 (Base)
Rotor Housing / Shaft	49	H7 / f7	Housing (Hole)	+0.025 / 0.000	49 / 49.025
			Shaft (Shaft)	-0.025 / -0.050	48.950 / 48.975
Stator Bracket / Stator Core	100	H7 / h6	Core (Hole)	+0.035 / 0.000	100 / 100.035
			Bracket (Shaft)	0.000 / -0.022	99.978 / 100
Air Gap (Stator to Rotor)	145/144	H7 / e7	Stator ID (Hole)	+0.040 / 0.000	145 / 145.040
			Rotor OD (Shaft)	-0.085 / -0.125	143.875 / 143.915

7 Multidisciplinary Design Evaluation

The transition toward electric aircraft and electrified aerospace propulsion systems demands electrical machines that not only has high-power density but also is characterized by high reliability and fault tolerance. Aerospace protocols dictate that no single-point failure can precipitate a catastrophic loss of the system. This requires exhaustive redundancy, rigorous Failure Mode and Effects Analysis (FMEA), and validation of all operational boundaries before a prototype is made flight-worthy. PMSMs used in current aerospace subsystems have been certified through existing certification structures, although certification practices are still evolving for high-power electric propulsion applications. However, transitioning from PMSM to FSPM topologies brings a fundamentally altered mechanical and electromagnetic aspect that nullifies many traditional failure baselines.

In conventional PMSMs, primary failure modes at high speeds often involve the mechanical retention of rotor magnets, where centrifugal forces can cause magnet detachment. The FSPM topology overcomes this problem by accommodating both the armature winding and the permanent magnets entirely within the static stator, leaving the rotor as a salient iron structure. While this solves high speed rotor retention problems, it consequently creates the thermal and structural complexities into the stator housing. The close placement of heat generating windings to temperature sensitive permanent magnets could create an environment susceptible to local saturation, thermal degradation, and cascading thermomechanical failures. Hence, a custom, detailed failure mode analysis is necessary. Such an analysis is needed to understand how the coupled effects of aerospace temperature gradients, microscopic manufacturing tolerances, and localized electromagnetic hotspots interact to influence the machine's integrity during flight operations.

It is important to note that the idea for performing the FMEA presented in this chapter was initiated during the later stages of this thesis. Therefore, this chapter is structured to document the recommendations provided by the expert panel, along with targeted validation studies for selected design improvements. These outcomes are intended to guide the next design iteration of the machine, ensuring a more robust and manufacturable solution in future development phases.

7.1 Workshop Design and Evaluation Framework

To identify and analyze these failure modes, a cross-functional technical design review workshop was convened on March 16, 2026 at Hybrid Electric Propulsion Cottbus (HepCO) hall. A structured peer-review methodology was implemented, aimed at interrogating the designed FSPM machine across three engineering domains, Electromagnetic, Mechanical and Manufacturing. To ensure a diverse and robust brainstorming session, 5 participants from different areas of expertise were invited. To avoid idea convergence and to avoid reflecting on the same idea, the participants were split and grouped into three teams (2–2–1). Following a presentation detailing the machine's current iteration, the workshop was structured around three, 20-minute tasks. After every 20-minutes, the teams were made to switch their focus between the electromagnetic, mechanical, and manufacturing contexts. This rotating, multidisciplinary structure ensured that the geometric constraints, material choices, and performance metrics were scrutinized from multiple engineering focus, yielding a summary of design vulnerabilities. The discussions conducted during the workshop across the three engineering domains were compiled into structured failure mode assessments. Tables 21-25 in the following sections summarize the identified failure modes, their causes, associated effects and recommended mitigation strategies, providing an overview of the key design vulnerabilities.

7.1.1 Manufacturing Feasibility, Tolerances, and Assembly Complexities

Table 21: Summary of manufacturing feasibility, tolerances, and assembly complexities for the proposed FSPM prototype (Part 1)

Part/ Assembly	Failure Mode (short)	Failure Statement	Cause(s)	Effect(s)/ Consequence	Recommended Mitigation(s)
Technical drawings / machined parts	Out-of-tolerance dimensions	Critical dimensions are not achieved repeatably in manufacture.	Exceptionally tight tolerances; simulated model assumes ideal rigidity/material behavior; standard machining capability may be insufficient.	Rework or scrap; high cost; delayed prototype build; non-repeatable assembly.	Relax non-functional tolerances; preserve only function-critical fits; run tolerance stack-up review; confirm supplier capability.
Shaft–rotor housing interface	Missing GD&T / runout control	Inadequate geometric tolerancing allows wobble, misfit, or mechanical interference at the shaft–housing interface.	Drawings lack explicit runout/-concentricity controls; datum insufficiently defined.	Rotor wobble; eccentric running; interference; degraded air-gap control.	Add explicit GD&T per function; retain the stated 0.02 mm perpendicularity; add runout/concentricity controls.
Shrink-fit joint	Shrink-fit assembly failure	The shrink-fit operation fails to achieve the intended interference joint during assembly.	Compounded tolerance chain; narrow thermal assembly window; high process sensitivity.	Incomplete seating; insecure torque transfer; possible scrap.	Create a controlled SOP; calculate interference formally; define heating/cooling window and assembly timing.
Shrink-fit mating faces	Assembly-induced component damage	Components are permanently damaged while mating during shrink-fitting.	Poor guidance/load distribution; rushed assembly; limited contact points.	Permanent damage; hidden defects; scrap.	Increase guidance; use alignment tooling; define force/time limits; perform dry runs.
Rotor and casing subassembly	Decentering during manufacture	Rotor and casing are not centered correctly during manufacturing/assembly.	Insufficient centering features; tolerance-stack accumulation.	Eccentricity; air-gap variation; vibration risk.	Introduce centering features; verify coaxiality before bearing installation.
Bearing locations / bearing build	Bearing misassembly	Ambiguous bearing assembly steps lead to incorrect installation.	Unclear sequence and preload control.	Premature bearing damage; misalignment; reduced life.	Define detailed assembly procedure and verification checks.
Magnetized stator / rotor insertion	Unsafe or imprecise manual insertion	Manual insertion of the rotor into the fully magnetized stator becomes unsafe or inaccurate.	Strong magnetic attraction; no insertion fixture.	Component damage; safety hazard; misalignment.	Design a controlled non-magnetic insertion fixture; prohibit manual insertion.

Table 22: Summary of manufacturing feasibility, tolerances, and assembly complexities for the proposed FSPM prototype (Part 2)

Part/ Assembly	**Failure Mode (short)**	**Failure Statement**	**Cause(s)**	**Effect(s)/ Consequence**	**Recommended Mitigation(s)**
Stator magnets / adhesive bond	Inadequate magnet retention (inferred)	Magnets can debond under thermal expansion or radial load.	Single-sided bonding; thermal mismatch.	Magnet movement; secondary damage.	Apply adhesive on all faces; validate with thermal-cycle and load testing.

7.1.2 Thermomechanical Vulnerabilities and Structural Integrity Limits

Table 23: Summary of thermomechanical vulnerabilities and structural integrity limits for the proposed FSPM prototype

Part/ Assembly	**Failure Mode (short)**	**Failure Statement**	**Cause(s)**	**Effect(s)/ Consequence**	**Recommended Mitigation(s)**
Rotor support / shrink-fit pins / air gap	Air-gap deformation and loss of concentricity	Thermal growth of shrink-fit pins and radial loads distort the primary air gap and push the rotor off-centre.	Pin thermal expansion; radial-load deformation; high air-gap sensitivity of FSPM topology.	Reduced torque quality; possible rubbing; electromagnetic asymmetry; efficiency loss.	Model coupled thermal-mechanical deformation; review pin geometry/material; define allowable eccentricity limits.
Stator core iron bridges	Local yielding of narrow bridges	Narrow stator bridges yield locally under combined radial force and thermal expansion.	Single-piece stator with narrow bridges; high radial forces; thermal expansion effects.	Permanent geometry change; altered air-gap; reduced stiffness; possible crack initiation.	Optimise bridge geometry; reassess one-piece vs segmented stator; define stress margins and minimum thickness.

7.1.3 Electromagnetic Constraints and Thermal Management Strategies

Table 24: Summary of electromagnetic constraints and thermal-management risks for the proposed FSPM prototype (Part 1)

Part/ Assembly	**Failure Mode (short)**	**Failure Statement**	**Cause(s)**	**Effect(s)/ Consequence**	**Recommended Mitigation(s)**
Permanent magnets	High magnet eddy-current loss (inferred)	Magnet eddy-current loss remains unnecessarily high in the unsliced configuration.	Long axial magnet piece supports larger circulating loss paths.	Additional magnet heating; reduced thermal margin; possible demagnetisation risk if severe.	Adopt the slicing concept: split 25 mm magnet into 5 pieces; loss reduction about 3.5×.
Outer-rotor electromagnetic geometry	Excess torque ripple (inferred)	Rotor geometry without suitable skew exhibits high torque ripple.	Harmonic content and discrete rotor geometry without validated skew optimisation.	Torque pulsation; vibration/NVH; possible control and mechanical-loading penalty.	Use stepped-skew optimisation: 5 steps, 4° skew, 79% ripple reduction with 6% torque drop.

Table 25: Summary of electromagnetic constraints and thermal-management risks for the proposed FSPM prototype (Part 2)

Part/ Assembly	**Failure Mode (short)**	**Failure Statement**	**Cause(s)**	**Effect(s)/ Consequence**	**Recommended Mitigation(s)**
Air-cooling path / windings	Asymmetric cooling and temperature non-uniformity	Rotor-induced airflow cools one side more than the other, creating uneven winding temperature.	Asymmetric internal airflow from rotating geometry; no validated CFD/thermal model yet.	Local thermal imbalance; uneven aging; additional asymmetry in machine behavior.	Validate cooling symmetry; adjust ducts/flow guides if needed; allowable side-to-side ΔT unspecified.
Stator insulation system	Insulation breakdown	If local thermal limits are exceeded, the insulation system fails.	Persistent hotspots; non-uniform cooling; underestimated losses; insufficient thermal qualification.	Short circuit; destructive asymmetrical operation; potentially severe machine behavior.	Qualify the insulation system for expected thermal/electrical stresses; introduce temperature-based protection until validated.
Cooling concept	Insufficient continuous-duty cooling	Ambient air cooling cannot remove enough heat at continuous rated aerospace load.	Highly concentrated losses; limited heat-transfer path; no comprehensive thermal analysis yet.	Continuous operation not sustainable; overheating; derating; reduced mission capability.	Benchmark against comparable motors; evaluate enhanced air cooling or alternate cooling concept.
System-level operating envelope	Off-design efficiency loss	Sizing around a single critical operating point causes unacceptable efficiency drop over the wider flight envelope.	Peak-point-centered optimization; limited multi-point mission analysis.	Lower mission efficiency; excess off-design heat; reduced system-level benefit.	Extend optimization to representative flight-envelope points and continuous mode.
Stator winding region	Concentrated thermal hotspots	Localized stator heat generation creates thermal hotspots in windings and nearby magnets.	Excitation source and armature windings are concentrated in the stator; heat sources are spatially clustered.	Local overtemperature; accelerated insulation aging; magnet heating; reduced continuous capability.	Add detailed thermal model; redistribute losses where feasible; improve local heat extraction.
Tooth / yoke saturated regions	Non-linear temperature spike	High local saturation and material-property uncertainty trigger unexpected non-linear temperature rise.	Local magnetic saturation; uncertain material characteristics; loss-model uncertainty.	Under-predicted heating; collapse of thermal margin.	Run sensitivity studies on material properties; include worst-case margins; validate loss assumptions experimentally; saturation threshold unspecified.

Despite the depth and technical value of these multidisciplinary discussions, it is important to define the scope boundaries of this thesis. The electromagnetic design and optimization performed in this work focus on a specific operating point under a defined temperature limit, in accordance with the initial task definition. Based on the critical electromagnetic design recommendations provided by the expert's panel, targeted follow-up analyses were done to evaluate the impact of proposed

Table 26: Results of magnet slicing study

Magnet Length	**Eddy Current Loss**
5 mm	3.4 W
25 mm	12 W

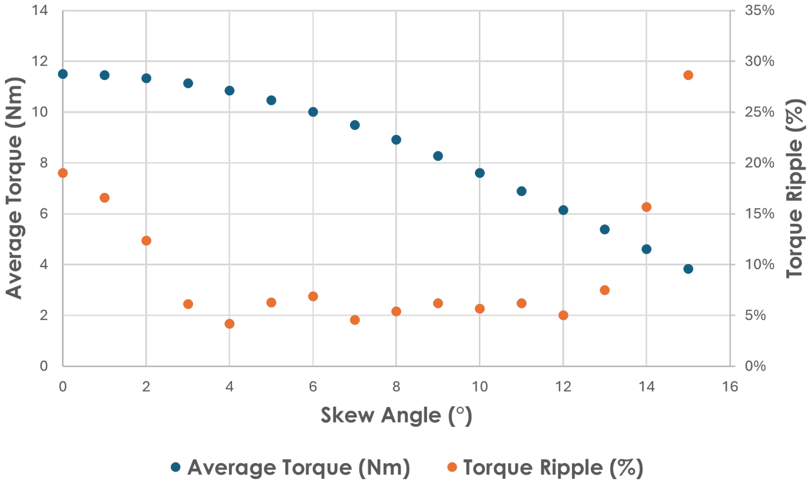

Figure 55: Results of outer-rotor skew study

electromagnetic modifications such as rotor skewing and magnets slicing. 3D FEA modeling study was done with sliced magnets and the results in Table 25 show a 3.5X drop in magnet eddy current losses when the 25mm magnet dimension defining its length proportional to the stack length is split into 5 pieces of 5mm each. Further, a stepped skewing of the outer rotor with five axial steps, and a parametric sweep of the skew angle from 0° to 15° with 1° increment is executed. The results shown in Figure 55 demonstrates almost a flat torque ripple zone between 4° and 12° skew angle, with a negative slope of the average torque. However, beyond 12°, a sharp increase in torque ripple is observed. This behavior is consistent with studies on flux-switching machines [55], which show that torque ripple depends on skew angle and step configuration. The increase in ripple at higher skew angles can be attributed to reduced harmonic cancellation and the discrete nature of stepped skew. Based on this analysis, a skew angle of 4° is identified for next design iteration, resulting in a torque ripple of 4%, corresponding to a 79% reduction compared to the unskewed design, with 6% decrease in average torque to 10.84 Nm.

7.2 Future Work and Design Validation Road map

The evaluation of magnet slicing and rotor step skewing shows the practical value of this design review, particularly in addressing key electromagnetic performance limitations. Building upon these outcomes, the workshop discussions highlighted several important directions for further development toward a fully validated machine. One of the primary extensions of this work is the need to expand the design evaluations beyond the single operating point considered in this thesis. Future studies should investigate the performance of the machine across the complete flight envelope. In addition to electromagnetic performance, the mechanical integrity of the machine requires further investigation. While potential risks such as radial deformation and dynamic eccentricity were identified during the workshop, a detailed structural validation of the machine has not been carried out within the scope of this thesis. Future work should therefore include comprehensive three-dimensional structural and thermomechanical analyses to evaluate the robustness of critical components, including the stator bridges, rotor assembly, and air-gap stability under combined thermal and mechanical loading conditions. Thermal management also represents a key area for further study. Due to the localized heat generation in FSPM topologies, advanced thermal modeling is required to understand temperature distribution and hotspot formation. This may also involve evaluating alternative cooling strategies to ensure reliable continuous operation under realistic loading conditions. Furthermore, the acoustic and vibrational behavior of the machine should be considered in future investigations. For aerospace and UAM applications, minimizing noise, vibration, and harshness (NVH) is an important requirement that was beyond the analytical scope of the present work. Overall, these future investigations extend the present study from a constrained electromagnetic design toward a more comprehensive, multi-physics validated machine design.

8 Conclusion

This thesis study explored the design, and preparation processes involving the manufacturing of an outer-rotor Flux Switching Permanent Magnet machine under non-ideal engineering constraints. This study addressed gap in the existing literature by integrating electromagnetic optimization with practical mechanical, electrical, and manufacturing constraints. In contrast to the studies conducted under idealized conditions, this research study employed a constraint driven design methodology that reflects real-world application requirements. Beginning with the analytical sizing of the machine, this study developed a parametric geometric model based on established design relations. This parameterization enabled systematic control over essential geometric variables. These parameters were defined using dimensionless ratio, ensuring geometric consistency and scalability throughout the optimization process. This analytical framework provided a 2D base model while highlighting limitations of analytical approaches in capturing nonlinear electromagnetic effects such as saturation and flux leakage. To overcome these limitations, a comprehensive FEA-based modeling framework was developed using ANSYS Maxwell. Both magnetostatic and transient analyses were conducted to evaluate key performance indicators, including average torque, efficiency, torque ripple, and inductance characteristics. The results demonstrated the nonlinear coupling between geometric variables and electromagnetic performance, thereby validating the necessity of advanced optimization strategies.

The core contribution of this thesis lies in the implementation and comparative evaluation of three distinct optimization methodologies which are Parametric Sweep Optimization, Direct optimization, and Meta-Model-Based Optimization. Each approach was applied within the same constrained design space to identify optimal trade-offs between competing objectives, namely maximizing torque and efficiency while minimizing torque ripple. The results showed that no single optimization method universally outperforms the others, rather their effectiveness depends on the complexity of the design space and computational resources. Parametric Sweep Optimization provided valuable insight into the sensitivity of design variables and enabled initial exploration of the design space. However, due to the exponential increase in computational cost with the number of variables, it proved inefficient for high-dimensional optimization problems. Direct optimization using evolutionary algorithms demonstrated strong capability in identifying Pareto optimal solutions, effectively handling nonlinear and complex objective functions. Nevertheless, this approach required a significant number of FEA evaluations, resulting in high computational expense. In contrast, the Meta-Model-Based Optimization approach offered a balanced trade-off between accuracy and computational efficiency. By constructing surrogate models using sampled FEA data, this method significantly reduced the number of required simulations while maintaining acceptable prediction accuracy. The validation results confirmed that the Meta-Model predictions closely matched time intensive FEA results, demonstrating its effectiveness for complex multi-objective optimization problems.

Following optimization, the selected design was evaluated through 3D FEA analysis to account for end-winding effects and axial flux leakage. The comparison between 2D and 3D results revealed reductions in performance due to these effects, insisting the importance of 3D evaluation for performance prediction. Beyond electromagnetic design, this thesis extended into mechanical and manufacturing domains. A complete mechanical assembly was developed by adapting the improved electromagnetic design with components derived from the Hacker Q150 motor. Technical drawings and tolerancing considerations were prepared to ensure manufacturability. Furthermore, a structured failure mode analysis conducted through a technical workshop identified potential risks related to electromagnetic performance, structural integrity, and manufacturing feasibility.

In conclusion, this work suggests that a constraint driven optimization framework is an effective approach for the design of high performance FSPM machines. The integration of FEA, advanced optimization techniques, and practical design considerations shows potential for developing machines that are both efficient and manufacturable. The findings highlight the importance of selecting appropriate optimization strategies based on problem complexity and computational resources. This thesis provides a comprehensive methodology that can be extended to other electric machine topologies, contributing to the advancement of electrified propulsion systems, particularly in aerospace applications where performance reliability, and feasibility are critical.

8.1 Future Outlook

Beyond the design recommendations from Chapter 7, one additional improvement identified in this study is the inclusion of cogging torque as an optimization objective. Cogging torque, arising from the interaction between permanent magnets and stator slots, partially contributes to torque ripple [31]. While torque ripple was considered in the present work, cogging torque has direct influence on vibration, acoustic noise, and low-speed performance, and treating it independently could further enhance machine behavior. In addition to that, incorporating the minimization of active machine mass as an additional objective would help achieve higher power density.

References

[1] E. Teichert and S. Kazula, *Overview and evaluation of electric machines for electric regional aircraft propulsion systems*, URN: urn:nbn:de:101:1-2412131008206.292630672769, Dec. 2024. DOI: `10.25967/630118`. [Online]. Available: `https://doi.org/10.25967/630118`.

[2] United Nations Framework Convention on Climate Change, *The paris agreement*, Available at: https://unfccc.int/process-and-meetings/the-paris-agreement, 2015.

[3] R. Leichter, *How much CO2 does the transportation sector emit?* [Online]. Available: https://www.cargoson.com/en/blog/how-much-co2-does-the-transportation-sector-emit, Cargoson blog. [Accessed: Oct. 12, 2025], 2025.

[4] J. Benzaquen, J. He, and B. Mirafzal, "Toward more electric powertrains in aircraft: Technical challenges and advancements," *CES Transactions on Electrical Machines and Systems*, vol. 5, no. 3, pp. 177–193, Sep. 2021. DOI: `10.30941/CESTEMS.2021.00022`.

[5] W. Cao, B. C. Mecrow, G. J. Atkinson, J. W. Bennett, and D. J. Atkinson, "Overview of electric motor technologies used for more electric aircraft (mea)," *IEEE Transactions on Industrial Electronics*, vol. 59, no. 9, pp. 3523–3531, Sep. 2012. DOI: `10.1109/TIE.2011.2165453`.

[6] National Centers for Environmental Information, *Climate at a glance: Global time series*, [Online]. Available: https://www.ncei.noaa.gov/access/monitoring/climate-at-a-glance/global/time-series, [Accessed: Oct. 12, 2025], 2026.

[7] D. Lee, S. Arrowsmith, A. Skowron, B. Owen, R. Sausen, O. Boucher, J. Faber, L. Marianne, J. Fuglestvedt, and L. van Wijngaarden, "Updated analysis of the non-CO2 climate impacts of aviation and potential policy measures pursuant to eu emissions trading system directive article 30 (4)," European Aviation Safety Agency, Report, 2020, [Accessed: Oct. 12, 2025].

[8] European Commission, "Flightpath 2050: Europe's vision for aviation," Publications Office of the European Union, Tech. Rep., 2011. DOI: `10.2777/50266`.

[9] M. Jahami, P. Singh, and B. Khandelwal, "Advancing aviation sustainability by 2050: Scaling renewable energy systems for hydrogen production and e-fuel integration," *Progress in Aerospace Sciences*, vol. 160, p. 101 170, 2026, ISSN: 0376-0421. DOI: `10.1016/j.paerosci.2025.101170`.

[10] International Air Transport Association (IATA), *Fly net zero by 2050*, [Online]. Available: https://www.iata.org/en/programs/sustainability/flynetzero/, [Accessed: Oct. 12, 2025], 2021.

[11] International Energy Agency (IEA) 4E Electric Motor Systems Annex (EMSA), "Policy brief – electric motor systems: Why are they important?" IEA 4E Electric Motor Systems Annex, Tech. Rep. Dec. 2025, [Online]. Available: https://www.iea-4e.org/emsa/publications/policy-brief-electric-motor-systems-why-are-they-important/. [Accessed: Oct. 12, 2025].

[12] ABB, *Abb motor sets new world record by achieving 99.13% energy efficiency*, [Online]. Available: https://new.abb.com/news/detail/126290/abb-motor-sets-new-world-record-by-achieving-9913-energy-efficiency, Press release, Zurich, Switzerland. [Accessed: Oct. 12, 2025], May 2025.

[13] R. H. Jansen, C. L. Bowman, S. Clarke, D. Avanesian, P. J. Dempsey, and R. W. Dyson, "Nasa electrified aircraft propulsion efforts," *Aircraft Engineering and Aerospace Technology: An International Journal*, vol. 92, no. 5, pp. 667–673, 2020. DOI: `10.1108/AEAT-05-2019-0098`.

[14] K. T. Chau and C. C. Chan, "Emerging energy-efficient technologies for hybrid electric vehicles," *Proceedings of the IEEE*, vol. 95, no. 4, pp. 821–835, Apr. 2007. DOI: `10.1109/JPROC.2006.890114`.

[15] B. Ban, "Synchronous reluctance machine optimization based on reduced set of geometric parameters with improved convergence and robust geometric feasibility verification," Ph.D. dissertation, Sveučilište u Zagrebu, Sveučilište u Zagrebu Fakultet elektrotehnike i . . ., 2022.

[16] S. E. Rauch and L. J. Johnson, "Design principles of flux-switch alternators," *Transactions of the American Institute of Electrical Engineers*, 1955.

[17] W. Hua, Z. Q. Zhu, M. Cheng, Y. Pang, and D. Howe, "Comparison of flux-switching and doubly-salient permanent magnet brushless machines," in *Proceedings of the International Conference on Electrical Machines and Systems (ICEMS)*, Nanjing, China, 2005, pp. 165–170. DOI: `10.1109/ICEMS.2005.202506`.

[18] Y. Liao, F. Liang, and T. A. Lipo, "A novel permanent magnet motor with doubly salient structure," in *Conference Record of the IEEE Industry Applications Society Annual Meeting (IAS)*, Houston, TX, USA, 1992, pp. 308–314. DOI: `10.1109/IAS.1992.244279`.

[19] R. P. Deodhar, S. Andersson, I. Boldea, and T. J. E. Miller, "The flux-reversal machine: A new brushless doubly-salient permanent-magnet machine," *IEEE Transactions on Industry Applications*, vol. 33, no. 4, pp. 925–934, Jul. 1997. DOI: `10.1109/28.605734`.

[20] E. Hoang, A. H. B. Ahmed, and J. Lucio, "Flux-switching permanent magnet motor," in *European Conference on Power Electronics and Applications*, 1997.

[21] Z. Q. Zhu, Y. Pang, D. Howe, S. Iwasaki, R. Deodhar, and A. Pride, "Analysis of electromagnetic performance of flux-switching permanent-magnet machines by nonlinear adaptive lumped parameter magnetic circuit model," *IEEE Transactions on Magnetics*, vol. 41, no. 11, pp. 4277–4287, Nov. 2005. DOI: `10.1109/TMAG.2005.854441`.

[22] W. Hua, M. Cheng, Z. Q. Zhu, W. Zhao, and X. Kong, "Comparison of electromagnetic performance of brushless motors having magnets in stator and rotor," *Journal of Applied Physics*, vol. 103, no. 7, 07F124, Apr. 2008. DOI: `10.1063/1.2838222`.

[23] M. Lehr, "Auslegung und bewertung elektrischer maschinen mit permanentmagneten im stator für hohe drehmomentdichten," Doctoral dissertation, Technische Universität Darmstadt, 2020. DOI: `10.25534/tuprints-00011751`. [Online]. Available: `https://tuprints.ulb.tu-darmstadt.de/id/eprint/11751`.

[24] J. T. Chen, Z. Q. Zhu, and D. Howe, "Stator and rotor pole combinations for multi-tooth flux-switching permanent-magnet brushless ac machines," *IEEE Transactions on Magnetics*, vol. 44, no. 12, pp. 4659–4667, Dec. 2008. DOI: `10.1109/TMAG.2008.2004264`.

[25] J. T. Chen, Z. Q. Zhu, S. Iwasaki, and R. Deodhar, "A novel e-core flux-switching pm brushless ac machine," in *Proceedings of the IEEE Energy Conversion Congress and Exposition (ECCE)*, Atlanta, GA, USA, 2010, pp. 3811–3818. DOI: `10.1109/ECCE.2010.5618332`.

[26] J. T. Chen, Z. Q. Zhu, S. Iwasaki, and R. P. Deodhar, "Influence of slot opening on optimal stator and rotor pole combination and electromagnetic performance of switched-flux pm brushless ac machines," *IEEE Transactions on Industry Applications*, vol. 47, no. 4, pp. 1681–1691, Jul. 2011. DOI: `10.1109/TIA.2011.2155011`.

[27] T. Raminosoa, C. Gerada, and M. Galea, "Design considerations for a fault-tolerant flux-switching permanent-magnet machine," *IEEE Transactions on Industrial Electronics*, vol. 58, no. 7, pp. 2818–2825, Jul. 2011. DOI: `10.1109/TIE.2010.2070782`.

[28] W. Z. Fei and J. X. Shen, “Novel permanent magnet switching flux motors,” in *Proceedings of the International Universities Power Engineering Conference (UPEC)*, Newcastle upon Tyne, UK, 2006, pp. 729–733. DOI: `10.1109/UPEC.2006.367575`.

[29] Y. J. Zhou and Z. Q. Zhu, “Torque density and magnet usage efficiency enhancement of sandwiched switched flux permanent magnet machines using v-shaped magnets,” *IEEE Transactions on Magnetics*, vol. 49, no. 7, pp. 3834–3837, Jul. 2013. DOI: `10.1109/TMAG.2013.2238219`.

[30] W. Fei, P. C. K. Luk, J. X. Shen, Y. Wang, and M. Jin, “A novel permanent-magnet flux switching machine with an outer-rotor configuration for in-wheel light traction applications,” *IEEE Transactions on Industry Applications*, vol. 48, no. 5, pp. 1496–1506, Sep. 2012. DOI: `10.1109/TIA.2012.2210009`.

[31] W. Fei, P. C. K. Luk, D. M. Miao, and J. X. Shen, “Investigation of torque characteristics in a novel permanent magnet flux switching machine with an outer-rotor configuration,” *IEEE Transactions on Magnetics*, vol. 50, no. 4, pp. 1–10, Apr. 2014. DOI: `10.1109/TMAG.2013.2288219`.

[32] X. Zhu, Z. Shu, L. Quan, Z. Xiang, and X. Pan, “Multi-objective optimization of an outer-rotor v-shaped permanent magnet flux switching motor based on multi-level design method,” *IEEE Transactions on Magnetics*, vol. 52, no. 10, p. 8 205 508, Oct. 2016. DOI: `10.1109/TMAG.2016.2581767`.

[33] G. Zhang, Q. Tong, A. Qiu, X. Xu, W. Hua, and Z. Chen, “Parameter sensitivity analysis and robust design approach for flux-switching permanent magnet machines,” *Energies*, vol. 15, no. 6, p. 2194, 2022. DOI: `10.3390/en15062194`.

[34] V. Dmitrievskii, V. Prakht, and V. Kazakbaev, “Design optimization of a permanent-magnet flux-switching generator for direct-drive wind turbines,” *Energies*, vol. 12, no. 19, p. 3636, 2019. DOI: `10.3390/en12193636`.

[35] K. S. Chai and C. Pollock, “Using genetic algorithms in design optimization of the flux switching motor,” in *Proceedings of the International Conference on Power Electronics, Machines and Drives (PEMD)*, Santa Fe, NM, USA, 2002, pp. 540–545. DOI: `10.1049/cp:20020174`.

[36] J. Gao, A. Liu, J. Yang, S. Zhao, and J. Liu, “Optimization of outer-rotor flux-switching permanent magnet motor using response surface method,” *Strojniški Vestnik - Journal of Mechanical Engineering*, vol. 70, no. 11-12, pp. 543–553, 2024. DOI: `10.5545/sv-jme.2023.859`.

[37] Z. Wang, Z. Wang, D. Xu, and F. Wang, “Multi-objective optimization of hybrid axial field flux-switching permanent magnet machine using genetic algorithms,” in *The Proceedings of the 11th Frontier Academic Forum of Electrical Engineering (FAFEE 2024)*, ser. Lecture Notes in Electrical Engineering, Q. Yang and J. Li, Eds., vol. 1293, Singapore: Springer, 2025. DOI: `10.1007/978-981-97-8832-3_33`.

[38] W. Fei, P. C. K. Luk, J. Shen, and Y. Wang, “A novel outer-rotor permanent-magnet flux-switching machine for urban electric vehicle propulsion,” in *Proceedings of the International Conference on Power Electronics Systems and Applications (PESA)*, Hong Kong, China, 2009, pp. 1–6.

[39] R. J. LeVeque, *Finite Difference Methods for Ordinary and Partial Differential Equations: Steady-State and Time-Dependent Problems*. Philadelphia, PA, USA: Society for Industrial and Applied Mathematics, 2007.

[40] L. Río-Martín, S. Busto, and M. Dumbser, “A massively parallel hybrid finite volume/finite element scheme for computational fluid dynamics,” *Mathematics*, vol. 9, no. 18, p. 2316, 2021. DOI: `10.3390/math9182316`.

[41] T. Betcke, E. van 't Wout, and P. Gélat, "Computationally efficient boundary element methods for high-frequency helmholtz problems in unbounded domains," in *Modern Solvers for Helmholtz Problems*, ser. Geosystems Mathematics, D. Lahaye, J. Tang, and K. Vuik, Eds., Cham: Birkhäuser, 2017. DOI: `10.1007/978-3-319-28832-1_9`.

[42] R. Harrington, "Origin and development of the method of moments for field computation," *IEEE Antennas and Propagation Magazine*, vol. 32, no. 3, pp. 31–35, Jun. 1990. DOI: `10.1109/74.80522`.

[43] H. Tiegna, Y. Amara, and G. Barakat, "Overview of analytical models of permanent magnet electrical machines for analysis and design purposes," *Mathematics and Computers in Simulation*, vol. 90, pp. 162–177, 2013, ISSN: 0378-4754. DOI: `10.1016/j.matcom.2012.12.002`.

[44] J. M. Jin, *The Finite Element Method in Electromagnetics*. Hoboken, NJ, USA: John Wiley & Sons, 2015.

[45] R. T. Ramamoorthy, B. Larimore, and M. Bhardwaj, "Sensored field oriented control of 3-phase permanent magnet synchronous motors using tms320f2837x," Texas Instruments, Dallas, TX, USA, Tech. Rep. SPRABZ0, 2016.

[46] A. Aktas and Y. Kircicek, *Solar Hybrid Systems: Design and Application*. London, UK: Academic Press, 2021.

[47] MathWorks, *Svpwm generator (2-level)*, [Online]. Available: https://de.mathworks.com/help/sps/powersys/ref/svpwmgenerator2level.html, [Accessed: Nov. 15, 2026].

[48] D. Pretorius, "Design study and analysis of a conventional radial-field flux-switching permanent magnet machine for a medium-speed wind turbine," M.S. thesis, Faculty of Engineering and the Built Environment, Department of Electrical Engineering, 2021. [Online]. Available: `http://hdl.handle.net/11427/33844`.

[49] G. Farina, *Lecture 1: Introduction*, MIT 6.7220/15.084 Nonlinear Optimization, Massachusetts Institute of Technology, [Online]. Available: https://www.mit.edu/ gfarina/67220/, [Accessed: Dec. 20, 2025], Feb. 2025.

[50] P. Gangl, S. Köthe, C. Mellak, A. Cesarano, and A. Mütze, "Multi-objective free-form shape optimization of a synchronous reluctance machine," *COMPEL: The International Journal for Computation and Mathematics in Electrical and Electronic Engineering*, vol. 41, no. 5, pp. 1849–1864, 2022. DOI: `10.1108/COMPEL-02-2021-0063`.

[51] T. Orosz, A. Rassõlkin, A. Kallaste, P. Arsénio, D. Pánek, J. Kaska, and P. Karban, "Robust design optimization and emerging technologies for electrical machines: Challenges and open problems," *Applied Sciences*, vol. 10, no. 19, p. 6653, 2020. DOI: `10.3390/app10196653`.

[52] Z. Zhu, X. Li, Y. Lin, H. Wu, J. Chen, N. Zhang, T. Wu, B. Lin, and S. Wang, "Multi-objective optimization design of high-power permanent magnet synchronous motor based on surrogate model," *Sustainability*, vol. 18, no. 3, p. 1705, 2026. DOI: `10.3390/su18031705`.

[53] R. D. Weerdt, E. Tuinman, K. Hameyer, and R. Belmans, "Finite element analysis of steady state behavior of squirrel cage induction motors compared with measurements," *IEEE Transactions on Magnetics*, vol. 33, no. 2, pp. 2093–2096, Mar. 1997. DOI: `10.1109/20.582733`.

[54] S. T. Lundmark, T. Thiringer, and E. A. Grunditz, "Traction motor 2d models with end winding leakage inductance consideration," in *Proceedings of the International Conference on Electrical Machines (ICEM)*, Torino, Italy, 2024, pp. 1–7. DOI: `10.1109/ICEM60801.2024.10700356`.

[55] W. Fei, P. C. K. Luk, and J. Shen, "Torque analysis of permanent-magnet flux switching machines with rotor step skewing," *IEEE Transactions on Magnetics*, vol. 48, no. 10, pp. 2664–2673, Oct. 2012. DOI: `10.1109/TMAG.2012.2198223`.

Appendices

Appendix A: B-H & J-H curve for Vacodym 633HR

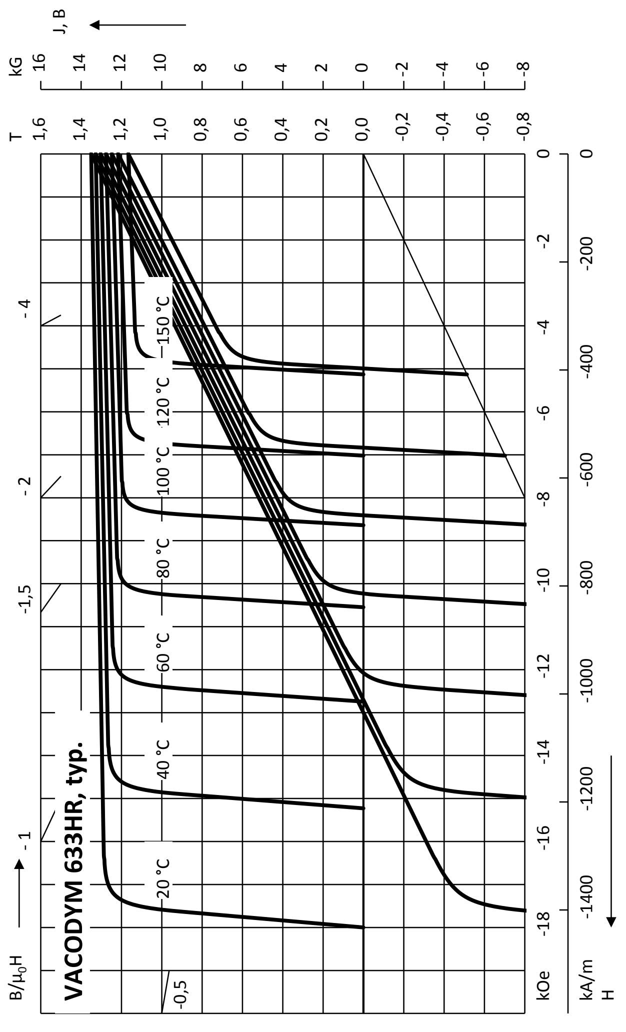

Appendix B: Post-Processing Script for Parametric Sweep Results

Script 1: Python script for parametric sweep data processing, constraint evaluation, and 3D surface generation.

```
import pandas as pd
import numpy as np
import matplotlib.pyplot as plt
from matplotlib import cm
import os

# ============================================================================
# SECTION 1: Setup and Directory Definition
# ============================================================================
base_dir = ’./Parametric_Sweep_Results’
torque_file_path = os.path.join(base_dir, ’Torque_Plot.csv’)
efficiency_file_path = os.path.join(base_dir, ’Efficiency_Plot.csv’)
voltage_file_path = os.path.join(base_dir, ’3Phase_Total_Voltage_Drop.csv’)
current_file_path = os.path.join(base_dir, ’BranchCurrent_Plot.csv’)

merge_cols = [’$Beta_M␣[deg]’, ’$Beta_R␣[deg]’]

# ============================================================================
# SECTION 2: Data Processing and Constraint Evaluation
# ============================================================================
df_torque = pd.read_csv(torque_file_path, float_precision=’round_trip’)
torque_col = ’Moving1.Torque␣[NewtonMeter]’
df_torque[torque_col] = df_torque[torque_col].astype(np.float64)

# Calculate Torque Statistics
torque_stats = df_torque.groupby(merge_cols).head(61).groupby(merge_cols)[torque_col].agg(
    Tavg=’mean’, Tmax=’max’, Tmin=’min’
).reset_index()
torque_stats[’Torque_Ripple_[%]’] = ((torque_stats[’Tmax’] - torque_stats[’Tmin’]) /
     torque_stats[’Tavg’]) * 100

# Calculate Efficiency Statistics
df_efficiency = pd.read_csv(efficiency_file_path, float_precision=’round_trip’)
eff_col = ’Efficiency␣[]’
df_efficiency[eff_col] = df_efficiency[eff_col].astype(np.float64)
eff_stats = df_efficiency.groupby(merge_cols).head(61).groupby(merge_cols)[eff_col].agg(
    Avg_Efficiency=’mean’
).reset_index()

# Evaluate Voltage Constraints
df_volt = pd.read_csv(voltage_file_path, float_precision=’round_trip’)
v_cols = [’NodeVoltage(IV_ph_A_Total)␣[V]’, ’NodeVoltage(IV_ph_B_Total)␣[V]’, ’NodeVoltage(
     IV_ph_C_Total)␣[V]’]
volt_stats = df_volt.groupby(merge_cols).head(61).groupby(merge_cols).apply(
    lambda g: max(g[v_cols[0]].abs().max(), g[v_cols[1]].abs().max(), g[v_cols[2]].abs().max())
         / 0.866
).reset_index(name=’Req_V_DC_[V]’)

# Evaluate Current Constraints
df_curr = pd.read_csv(current_file_path, float_precision=’round_trip’)
i_cols = [’BranchCurrent(Vi_a)␣[A]’, ’BranchCurrent(Vi_b)␣[A]’, ’BranchCurrent(Vi_c)␣[A]’]
curr_stats = df_curr.groupby(merge_cols).head(61).groupby(merge_cols).apply(
    lambda g: max([np.sqrt(np.mean(g[c]**2)) for c in i_cols])
).reset_index(name=’Max_I_RMS_[A]’)

# ============================================================================
# SECTION 3: Normalization and Ranking
# ============================================================================
df_master = pd.merge(torque_stats, eff_stats, on=merge_cols)
df_master = pd.merge(df_master, volt_stats, on=merge_cols)
df_master = pd.merge(df_master, curr_stats, on=merge_cols)

# Apply Hardware Constraints
df_master[’Hardware_Valid’] = (df_master[’Req_V_DC_[V]’] < 100.0) & (df_master[’Max_I_RMS_[A]’]
      < 80.0)

# Normalize metrics for scoring
w = 1.0 / 3.0
for c, norm in [(’Tavg’, ’Norm_Tavg’), (’Avg_Efficiency’, ’Norm_Efficiency’)]:
    df_master[norm] = (df_master[c] - df_master[c].min()) / (df_master[c].max() - df_master[c].
        min())
```

```
df_master[’Norm_Ripple’] = (df_master[’Torque_Ripple_[%]’].max() - df_master[’Torque_Ripple_[%]
     ’]) / (df_master[’Torque_Ripple_[%]’].max() - df_master[’Torque_Ripple_[%]’].min())

# Calculate Total Score and Rank
df_master[’Total_Score’] = (df_master[’Norm_Tavg’] * w) + (df_master[’Norm_Ripple’] * w) + (
     df_master[’Norm_Efficiency’] * w)
df_master_ranked = df_master.sort_values(by=’Total_Score’, ascending=False).reset_index(drop=
     True)

# ===========================================================================
# SECTION 4: 3D Response Surface Generation
# ===========================================================================
valid_designs = df_master_ranked[df_master_ranked[’Hardware_Valid’] == True]
best_design_coords = valid_designs.iloc[0] if not valid_designs.empty else None

beta_m_axis = np.sort(df_master_ranked[’$Beta_M␣[deg]’].unique())
beta_r_axis = np.sort(df_master_ranked[’$Beta_R␣[deg]’].unique())
X, Y = np.meshgrid(beta_m_axis, beta_r_axis)

metrics_to_plot = [
    (’Tavg’, ’Average␣Torque␣(Nm)’, ’Surface_Plot_Average_Torque.png’),
    (’Torque_Ripple_[%]’, ’Torque␣Ripple␣(%)’, ’Surface_Plot_Torque_Ripple.png’),
    (’Avg_Efficiency’, ’Average␣Efficiency␣(%)’, ’Surface_Plot_Average_Efficiency.png’)
]

for col, z_label, filename in metrics_to_plot:
    Z_matrix = df_master_ranked.pivot(index=’$Beta_R␣[deg]’, columns=’$Beta_M␣[deg]’, values=
         col).values
    fig = plt.figure(figsize=(10, 8))
    ax = fig.add_subplot(111, projection=’3d’)
    surf = ax.plot_surface(X, Y, Z_matrix, cmap=cm.coolwarm, edgecolor=’black’, linewidth=0.5,
         alpha=0.65)

    if best_design_coords is not None:
        ax.scatter(best_design_coords[’$Beta_M␣[deg]’], best_design_coords[’$Beta_R␣[deg]’],
             best_design_coords[col],
                   color=’red’, s=150, marker=’o’, edgecolor=’black’, zorder=50, label=’Optimal
                       ␣Design’)
        ax.legend(loc=’upper␣right’)

    ax.set_xlabel(r’Magnet␣Arc␣($^\circ$)’)
    ax.set_ylabel(r’Rotor␣Arc␣($^\circ$)’)
    ax.set_zlabel(z_label)
    ax.set_title(f’Response␣Surface:␣{z_label}’)

    fig.colorbar(surf, ax=ax, shrink=0.5, aspect=12, pad=0.1, label=’Magnitude’)
    ax.view_init(elev=40, azim=135)

    plt.tight_layout()
    plt.savefig(os.path.join(base_dir, filename), dpi=300)
    plt.close()
```

Appendix C: Automation Framework Script

Script 2: Python script for PyAEDT automated geometry generation, constraint calculation, and two-step FEM simulation.

```
import math
import os
import shutil
import time
import pandas as pd
from pyaedt import Maxwell2d, Desktop
import numpy as np

# ===========================================================================
# SECTION 1: Setup and Directory Definition
# ===========================================================================
base_project_name = "Base_Machine_Model"
original_template_path = r"./Templates/Base_Machine_Model.aedt"
swg_lookup_path = r"./Reference_Data/swg_lookup.csv"

if not ’OSL_REGULAR_EXECUTION’ in locals():
    OSL_REGULAR_EXECUTION = False

if not OSL_REGULAR_EXECUTION:
    wdir = r"./Simulation_Runs"
    design_name_suffix = "test_run"
    project_path = original_template_path
    output_folder = os.path.join(wdir, "output_" + design_name_suffix)
    swg_path = swg_lookup_path

    if not os.path.exists(output_folder):
        os.makedirs(output_folder)

    # Standalone Test Parameters
    osl_ORD = 180
    osl_IRD = 145
    osl_SDia = 100
    osl_AG = 0.5
    osl_Ntc = 10
    osl_Strands = 4
    osl_Gamma_Beta_S = 0.515207
    osl_Gamma_S = 0.217847
    osl_hs0 = 1
    osl_Gamma_R = 0.562551
    osl_R_tip_taper_Outer = 0.910889
    osl_R_tooth_ratio = 0.66467
    osl_RMSCurrentDensity = 5.0
    osl_rotor_rpm = 2500
    osl_Thick_Ratio = 0.288585
    osl_Len_Ratio = 0.94
    osl_R_Fillet = 0
    osl_F_Ratio = 0.797786
else:
    wdir = OSL_DESIGN_DIR
    design_name_suffix = OSL_DESIGN_NAME
    project_path = os.path.join(wdir, base_project_name + "_" + design_name_suffix + ".aedt")
    output_folder = os.path.join(wdir, "output_" + design_name_suffix)
    swg_path = swg_lookup_path

    if not os.path.exists(output_folder):
        os.makedirs(output_folder)

    if not os.path.exists(project_path):
        shutil.copyfile(original_template_path, project_path)

param_dict = {
    "$ORD": (osl_ORD, "mm"),
    "$IRD": (osl_IRD, "mm"),
    "$SDia": (osl_SDia, "mm"),
    "$AG": (osl_AG, "mm"),
    "$Ntc": (osl_Ntc, ""),
    "$Strands": (osl_Strands, ""),
    "$Gamma_Beta_S": (osl_Gamma_Beta_S, ""),
    "$Gamma_S": (osl_Gamma_S, ""),
    "$hs0": (osl_hs0, "mm"),
    "$Gamma_R": (osl_Gamma_R, ""),
    "$R_tip_taper_Outer": (osl_R_tip_taper_Outer, ""),
    "$R_tooth_ratio": (osl_R_tooth_ratio, ""),
    "$Ic": (0.0, "A"),
```

```
    "$rotor_rpm": (osl_rotor_rpm, ""),
    "$Thick_Ratio": (osl_Thick_Ratio, ""),
    "$Len_Ratio": (osl_Len_Ratio, ""),
    "$R_Fillet": (0.0, "mm"),
    "$F_Ratio": (osl_F_Ratio, ""),
    "$L_Stack": (25, "mm"),
    "$Phases": (3, ""),
    "$S_Slots": (12, ""),
    "$R_Poles": (14, ""),
    "$WIre_Diameter": (2.946, "mm"),
    "$Rho_Copper_20": (1.72E-08, "Ohmm"),
    "$T_ambient": (40, "cel"),
    "$Temp_Coefficient": (0.0039, "per_cel"),
    "$T_rise": (60, "cel"),
    "$Npph": (1, ""),
    "$R_tip_taper": (1, ""),
    "$Bridge_Thickness": (0.5, "mm"),
    "$alpha_Is": (90, ""),
    "$Ind": (29.10908, "uH"),
    "$n": (60, "")
}

# =============================================================================
# SECTION 2: Dynamic Geometry and Winding Area Calculations
# =============================================================================
IRD_val = float(param_dict["$IRD"][0])
AG_val = float(param_dict["$AG"][0])
SDia_val = float(param_dict["$SDia"][0])
Thick_Ratio_val = float(param_dict["$Thick_Ratio"][0])
Len_Ratio_val = float(param_dict["$Len_Ratio"][0])
Gamma_Beta_S_val = float(param_dict["$Gamma_Beta_S"][0])
S_Slots_val = int(param_dict["$S_Slots"][0])
pi = math.pi

alpha_s_deg_for_magnets = 360.0 / S_Slots_val
beta_s_rad_for_magnets = Gamma_Beta_S_val * alpha_s_deg_for_magnets * (pi / 180)
stw_for_magnets = (IRD_val - 2 * AG_val) * math.sin(beta_s_rad_for_magnets / 2)
Mag_Thickness = Thick_Ratio_val * stw_for_magnets
Mag_Length = Len_Ratio_val * (IRD_val / 2 - AG_val - SDia_val / 2)

param_dict["$Mag_Thickness"] = (Mag_Thickness, "mm")
param_dict["$Mag_Length"] = (Mag_Length, "mm")

Gamma_S = float(param_dict["$Gamma_S"][0])
Alpha_S = 30
hs0 = float(param_dict["$hs0"][0])
Ntc = int(param_dict["$Ntc"][0])
Strands = int(param_dict["$Strands"][0])
slot_fill_factor = 0.5
Beta_S = Alpha_S * Gamma_Beta_S_val * (pi / 180)
STW = (IRD_val - 2 * AG_val) * math.sin(Beta_S / 2)
STW_elongated = (IRD_val - 2 * AG_val) * (Beta_S / 2)
SYW = Gamma_S * STW
STH = ((IRD_val - SDia_val) / 2) - (AG_val + SYW)
A_shaft = pi * (SDia_val ** 2) / 4
A_yoke = (pi / 4) * (((SDia_val + 2 * SYW) ** 2) - (SDia_val ** 2))
A_teeth = S_Slots_val * STW_elongated * STH
tip_circ = pi * (IRD_val - 2 * AG_val)
total_tip_circ = ((IRD_val / 2) - AG_val) * Beta_S * S_Slots_val
X = (tip_circ - total_tip_circ) / (2 * S_Slots_val)
hs_dia_circ = pi * (IRD_val - 2 * (AG_val + hs0))
total_tip_circ_hs = ((IRD_val / 2) - AG_val - hs0) * Beta_S * S_Slots_val
Y = (hs_dia_circ - total_tip_circ_hs) / (2 * S_Slots_val)
A_hs = ((X + Y) / 2) * (hs0 * 2 * S_Slots_val)
A_stator = (pi * (IRD_val - 2 * AG_val) ** 2) / 4
A_winding = (A_stator - (A_shaft + A_yoke + A_teeth + A_hs)) / (2 * S_Slots_val)

df_swg = pd.read_csv(swg_path)
df_swg["Total_Area_Required"] = df_swg["Area␣[mm^2]"] * Ntc * Strands / slot_fill_factor
df_swg["Diff"] = np.abs(df_swg["Total_Area_Required"] - A_winding)
best_match = df_swg.loc[df_swg["Diff"].idxmin()]
wire_diameter = best_match["Diameter␣[mm]"]
wire_area_single_strand = best_match["Area␣[mm^2]"]

param_dict["$WIre_Diameter"] = (wire_diameter, "mm")
o_WireDiameter_Chosen = round(wire_diameter, 3)

rms_current_density_input = float(osl_RMSCurrentDensity)
calculated_ic = rms_current_density_input * wire_area_single_strand * Strands
```

```
param_dict["$Ic"] = (calculated_ic, "A")
o_Ic = round(calculated_ic, 3)
calculated_current_density = (calculated_ic / Strands) / wire_area_single_strand
o_CalculatedCurrentDensity = round(calculated_current_density, 3)
o_CurrentDensityExceeded = 1 if calculated_current_density > rms_current_density_input * 1.001
     else 0

# =============================================================================
# SECTION 3: FEM Simulation Execution and Extraction
# =============================================================================
desktop = None
app = None
transient_app = None

try:
    desktop = Desktop(specified_version="2024.1", non_graphical=False, new_desktop_session=
        False)

    # --- Magnetostatic Simulation ---
    mag_static_name = "Step_1_MagnetoStatic"
    app = Maxwell2d(project=project_path, design=mag_static_name, solution_type="Magnetostatic"
        , non_graphical=False)

    for name, (val, unit) in param_dict.items():
        app[name] = f"{val}{unit}" if unit else str(val)

    target_edge_id_1 = 39561
    target_edge_id_2 = 39692
    measured_length_edge_1 = app.modeler.get_edge_length(target_edge_id_1)
    measured_length_edge_2 = app.modeler.get_edge_length(target_edge_id_2)
    lowest_measured_length = min(filter(lambda x: x > 0, [measured_length_edge_1,
        measured_length_edge_2]), default=0.0)
    calculated_r_fillet = (lowest_measured_length / 2) * float(param_dict["$F_Ratio"][0])

    param_dict["$R_Fillet"] = (calculated_r_fillet, "mm")
    app["$R_Fillet"] = f"{calculated_r_fillet}mm"
    o_MeasuredEdgeLength = round(lowest_measured_length, 3)
    o_R_Fillet_Calculated = round(calculated_r_fillet, 3)

    app.variable_manager["i_a"] = "1"
    app.variable_manager["i_b"] = "0"
    app.variable_manager["i_c"] = "0"
    app.analyze()

    app.post.export_report_to_csv(output_folder, "Self␣Inductance")
    app.post.export_report_to_csv(output_folder, "Mutual␣Inductance")
    df_self = pd.read_csv(os.path.join(output_folder, "Self␣Inductance.csv"))
    df_mutual = pd.read_csv(os.path.join(output_folder, "Mutual␣Inductance.csv"))
    avg_Laa = df_self["Matrix1.L(PhaseA,PhaseA)␣[uH]"].mean()
    avg_M = (df_mutual["Matrix1.L(PhaseA,PhaseB)␣[uH]"].mean() + df_mutual["Matrix1.L(PhaseA,
        PhaseC)␣[uH]"].mean()) / 2
    net_Ind = round(avg_Laa - avg_M, 3)
    o_Inductance = net_Ind

    # --- Transient Simulation ---
    transient_name = "Step_2_Transient"
    transient_app = Maxwell2d(project=project_path, design=transient_name, solution_type="
        Transient", non_graphical=False)
    for name, (val, unit) in param_dict.items():
        transient_app[name] = f"{val}{unit}" if unit else str(val)
    transient_app["$Ind"] = f"{net_Ind}uH"
    transient_app.analyze()

    transient_app.post.export_report_to_csv(output_folder, "Torque")
    df_torque = pd.read_csv(os.path.join(output_folder, "Torque.csv"))
    torque_col = [col for col in df_torque.columns if "Torque" in col][0]
    processed_torque_data = df_torque[torque_col]
    o_AvgTorque = round(processed_torque_data.mean(), 3)
    o_TorqueRipple = round(((processed_torque_data.max() - processed_torque_data.min()) /
        o_AvgTorque) * 100, 3) if o_AvgTorque != 0 else 0.0

    transient_app.post.export_report_to_csv(output_folder, "Efficiency")
    df_eff = pd.read_csv(os.path.join(output_folder, "Efficiency.csv"))
    o_AvgEfficiency = round(df_eff["Efficiency␣[]"].mean(), 3)

    transient_app.post.export_report_to_csv(output_folder, "Total_Voltage")
    df_volt = pd.read_csv(os.path.join(output_folder, "Total_Voltage.csv"))
    v_peaks = [df_volt[col].max() for col in ["NodeVoltage(IV_ph_A_Total)␣[V]", "NodeVoltage(
        IV_ph_B_Total)␣[V]", "NodeVoltage(IV_ph_C_Total)␣[V]"]]
```

```
    o_VphasePeak = round(max(v_peaks), 3)
    o_VdcCalculated = round(o_VphasePeak / 0.866, 3)
    o_VoltageLimitExceeded = 1 if o_VdcCalculated > 100.0 else 0

finally:
    if app: app.save_project()
    if transient_app: transient_app.save_project()
    if desktop: desktop.release_desktop(close_projects=True)
```

Appendix D: Standard Wire Gauge (SWG) Reference Table

Standard Wire Gauge (SWG) Dimensions and Corresponding Areas.

SWG #	**Diameter (mm)**	**Area (mm^2)**
(7/0)	12.700	126.6769
(6/0)	11.786	109.0921
(5/0)	10.973	94.5638
(4/0)	10.160	81.0732
(3/0)	9.449	70.1202
(2/0)	8.839	61.3643
0	8.230	53.1921
1	7.620	45.6037
2	7.010	38.5989
3	6.401	32.1780
4	5.893	27.2730
5	5.385	22.7735
6	4.877	18.6793
7	4.470	15.6958
8	4.064	12.9717
9	3.658	10.5071
10	3.251	8.3019
11	2.946	6.8183
12	2.642	5.4805
13	2.337	4.2888
14	2.032	3.2429
15	1.829	2.6268
16	1.626	2.0755
17	1.422	1.5890
18	1.219	1.1675
19	1.016	0.8107
20	0.914	0.6567
21	0.813	0.5189
22	0.711	0.3973
23	0.610	0.2919
24	0.559	0.2452
25	0.508	0.2027
26	0.4572	0.1642
27	0.4166	0.1363
28	0.3759	0.1110

Continued on next page

– continued from previous page

SWG #	**Diameter (mm)**	**Area (mm^2)**
29	0.3454	0.0937
30	0.3150	0.0779
31	0.2946	0.0682
32	0.2743	0.0591
33	0.2540	0.0507
34	0.2337	0.0429
35	0.2134	0.0358
36	0.1930	0.0293
37	0.1727	0.0234
38	0.1524	0.0182
39	0.1321	0.0137
40	0.1219	0.0117
41	0.1118	0.0098
42	0.1016	0.0081
43	0.0914	0.0066
44	0.0813	0.0052
45	0.0711	0.0040
46	0.0610	0.0029
47	0.0508	0.0020
48	0.0406	0.0013
49	0.0305	0.0007
50	0.0254	0.0005

Appendix E: Stator Core Lamination Drawing

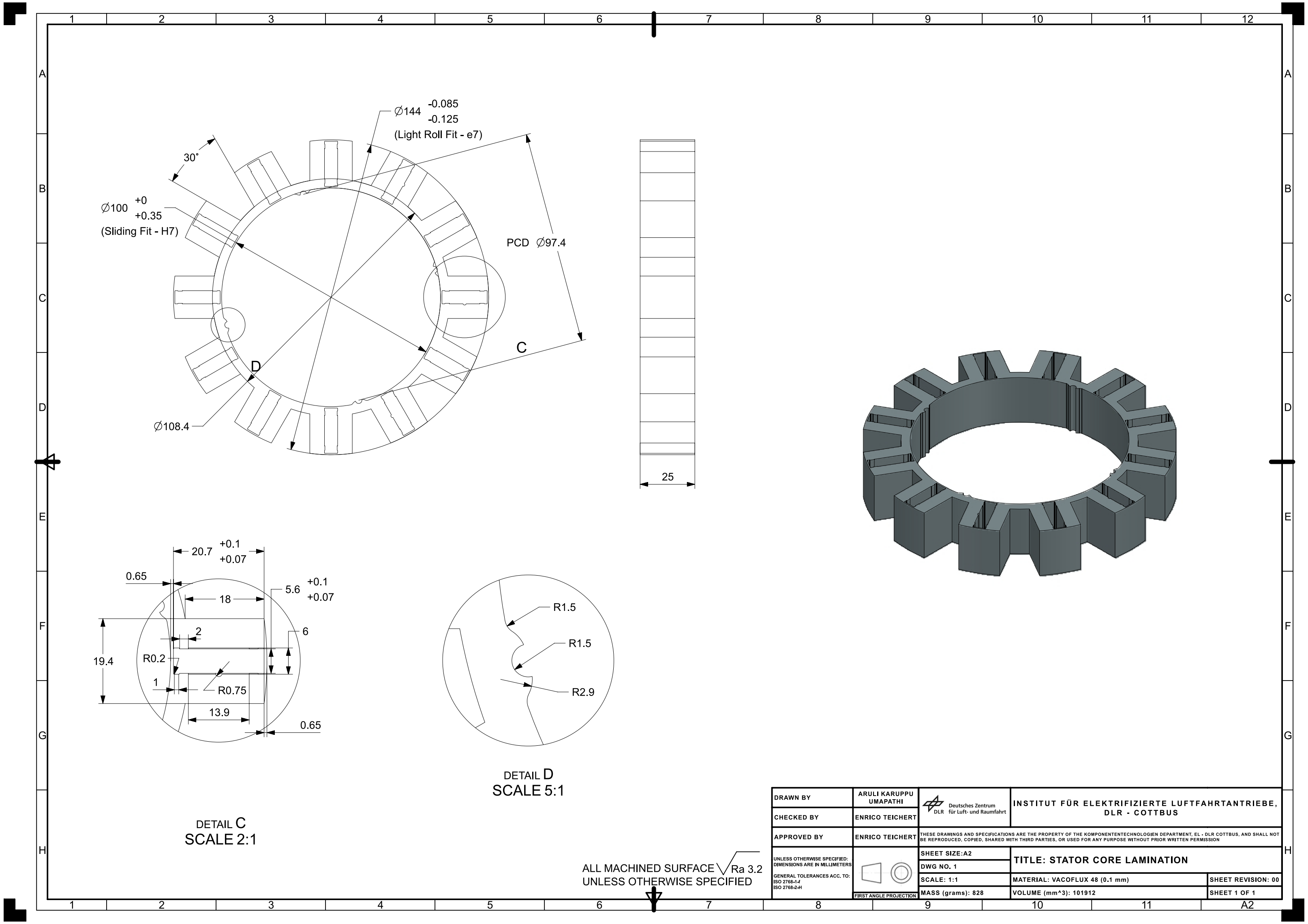

DRAWN BY	ARULI KARUPPU UMAPATHI	INSTITUT FÜR ELEKTRIFIZIERTE LUFTFAHRTANTRIEBE, DLR - COTTBUS
CHECKED BY	ENRICO TEICHERT	
APPROVED BY	ENRICO TEICHERT	THESE DRAWINGS AND SPECIFICATIONS ARE THE PROPERTY OF THE KOMPONENTENTECHNOLOGIEN DEPARTMENT, EL - DLR COTTBUS, AND SHALL NOT BE REPRODUCED, COPIED, SHARED WITH THIRD PARTIES, OR USED FOR ANY PURPOSE WITHOUT PRIOR WRITTEN PERMISSION
UNLESS OTHERWISE SPECIFIED: DIMENSIONS ARE IN MILLIMETERS GENERAL TOLERANCES ACC. TO: ISO 2768-1-f ISO 2768-2-H	SHEET SIZE:A2 DWG NO. 1	TITLE: STATOR CORE LAMINATION
	SCALE: 1:1	MATERIAL: VACOFLUX 48 (0.1 mm) — SHEET REVISION: 00
	MASS (grams): 828	VOLUME (mm^3): 101912 — SHEET 1 OF 1

Appendix F: Rotor Core Lamination Drawing

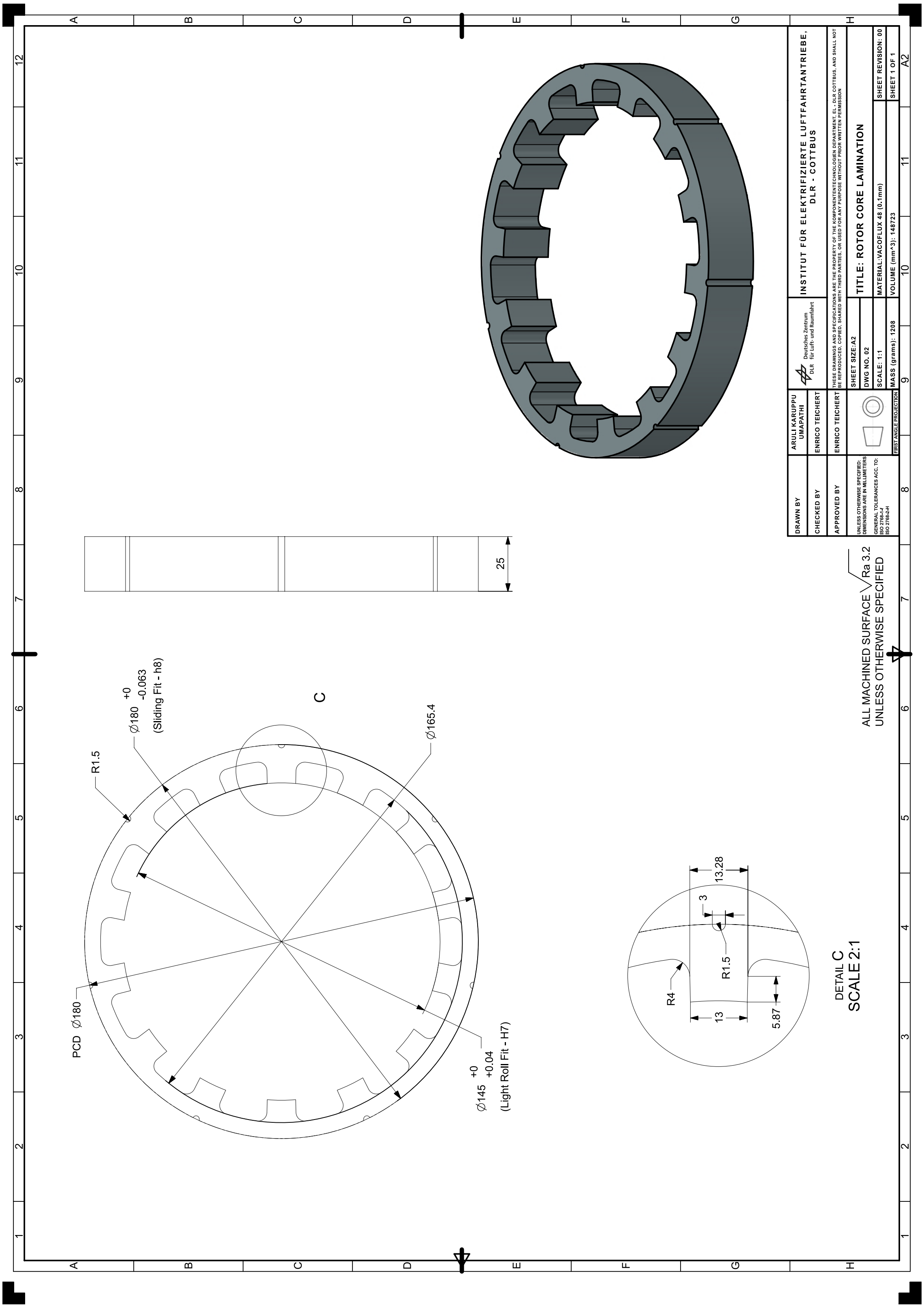

Appendix G: Rotor Housing Drawing

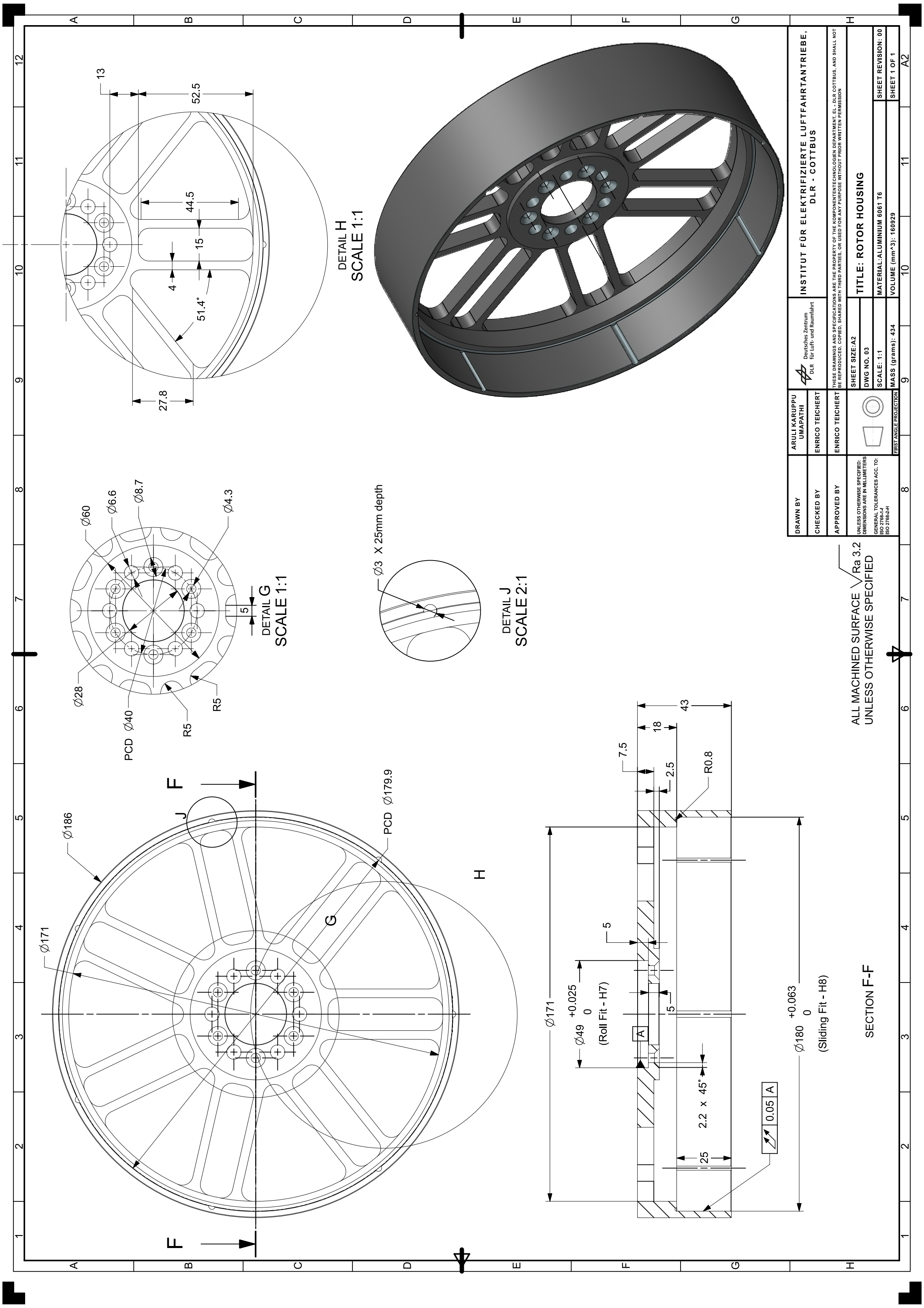

Appendix H: Magnet Drawing

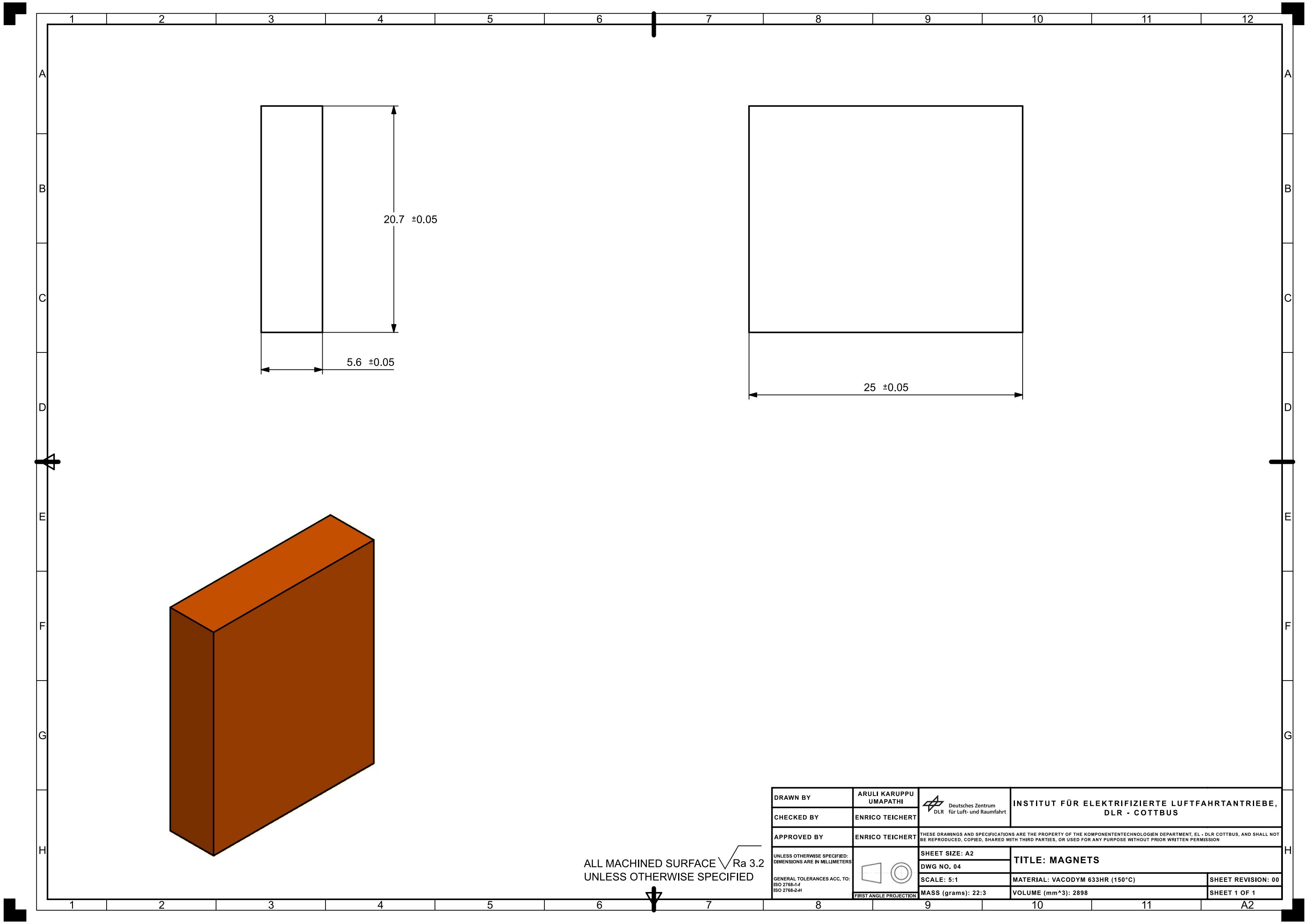

Appendix I: Prototype FSM Assembly Procedure

Step 1:	Place the rotor housing in the oven at the specified temperature for the required duration. Remove the heated rotor housing and place it on a thermally insulated flat surface.
Step 2:	Insert the integrated rotor core into the heated rotor housing. Ensure that the rotor core is not tilted and is properly seated on the horizontal surface provided inside the housing, as shown in Figure 56.
Step 3:	Align the semi-circular hole of the rotor core with the corresponding semi-circular hole in the rotor housing, as shown in Figure 57.
Step 4:	Insert the seven rotor shrink-fit pins (⌀3 mm × 25 mm) into the designated holes in the assembly. After insertion, allow the rotor housing to contract and secure the rotor core and pins firmly in place, as shown in Figure 58.
Step 5:	Assemble the shaft with the rotor housing using six countersunk screws (M3 × 10 mm), as shown in Figure 59.
Step 6:	Insert bearing 6005 onto the shaft from the opposite side, as shown in Figure 60, and ensure that it is properly seated at the designated position on the shaft.
Step 7:	Set the rotor assembly aside. Take the integrated stator core and insert the 12 magnets, applying adhesive on the circumference and in the slots provided in the stator core. Allow sufficient curing time before proceeding with the winding process, as shown in Figure 61.
Step 8:	After winding the core, insert the wound stator core into the stator bracket. Align it with the axial projection provided on the inner diameter of the stator core, as shown in Figure 62. The winding illustrated is a representative depiction and does not correspond to the actual winding geometry.
Step 9:	Insert the twist-protection pins into the four holes between the stator bracket and the stator core, as shown in Figure 63.
Step 10:	Attach four axial compression clamps to secure the stator core to the bracket. Use two countersunk screws (M3 × 10 mm) per clamp to prevent any axial movement of the core, as shown in Figure 64.
Step 11:	Insert the completed stator assembly into the prepared rotor assembly. Ensure that the clamped stator side is inserted into the rotor housing, as shown in Figure 65.
Step 12:	Insert bearing 6004 into the assembly onto the shaft side and ensure that it is properly seated, as shown in Figure 66.
Step 13:	Install the locknut onto the shaft, as shown in Figure 67. Tighten it to prevent axial movement during operation.
Step 14:	Secure the locknut using the lock washer and shaft keyway to prevent loosening due to vibrations, as shown in Figure 68.

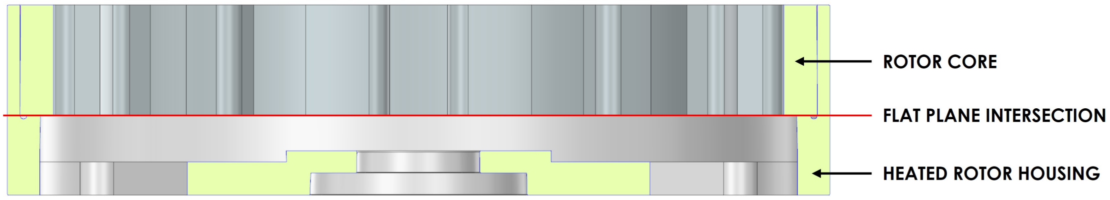

Figure 56: Rotor core seated inside heated rotor housing

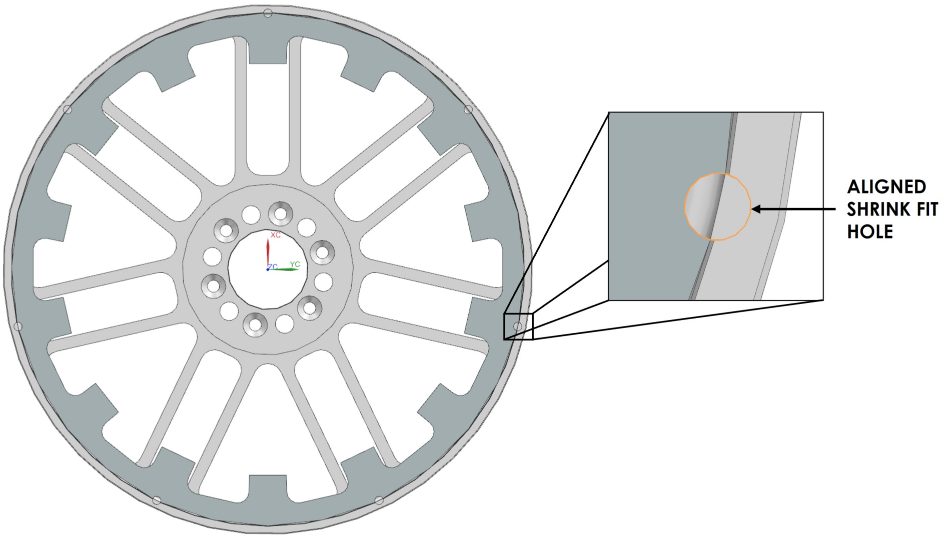

Figure 57: Alignment of semi-circular holes in rotor core and housing

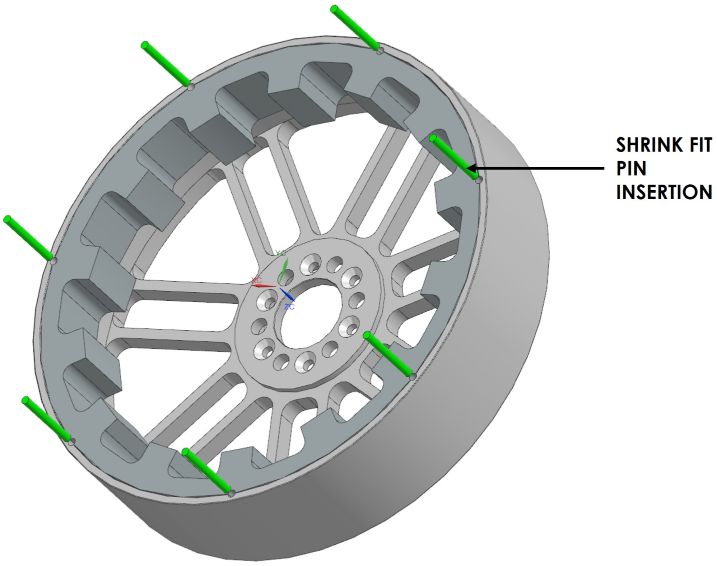

Figure 58: Insertion of rotor shrink-fit pins

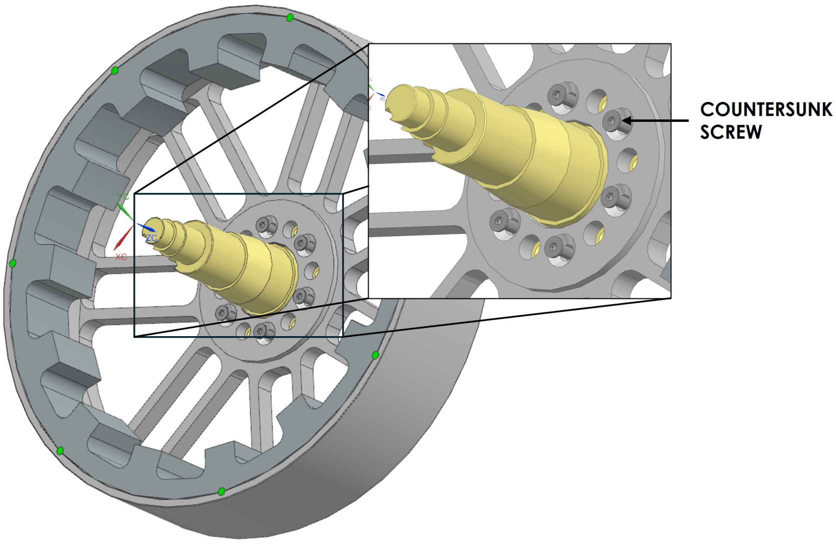

Figure 59: Shaft assembly with countersunk screws

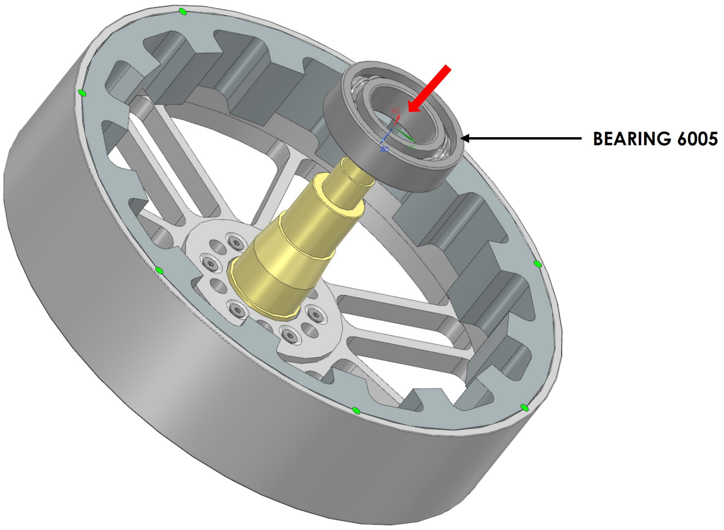

Figure 60: Installation of bearing 6005 on shaft

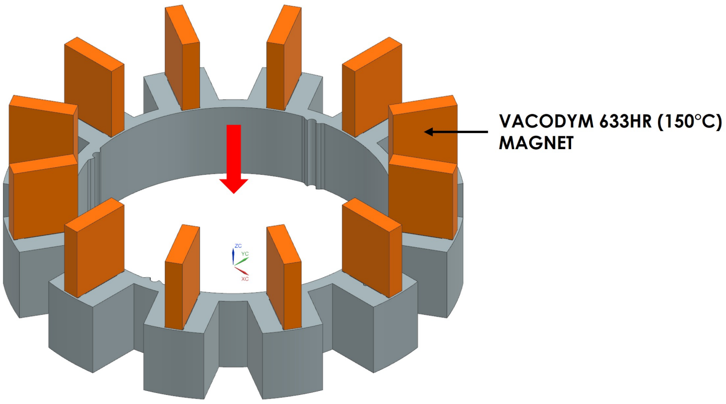

Figure 61: Magnet insertion into stator core

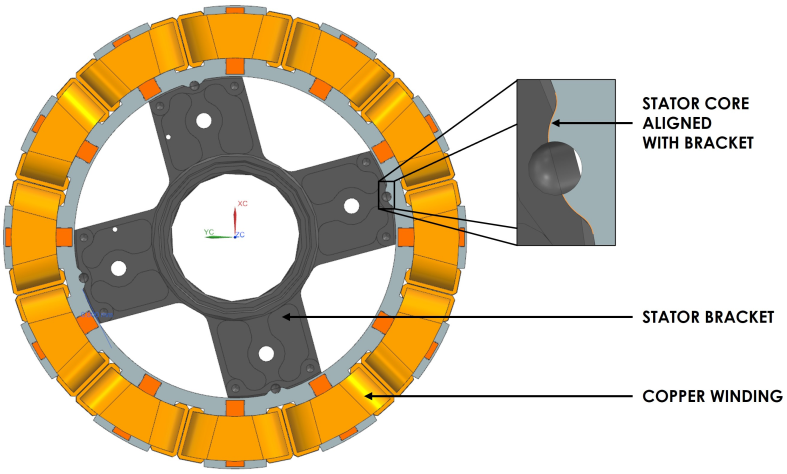

Figure 62: Stator core alignment with bracket

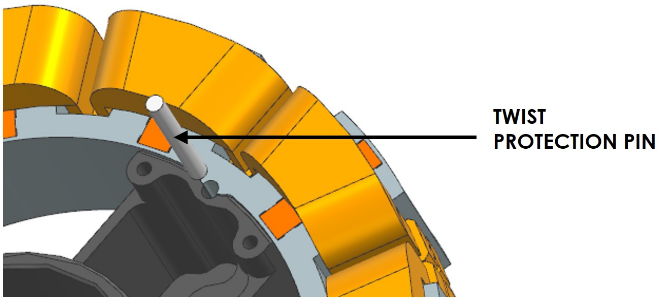

Figure 63: Insertion of twist-protection pins

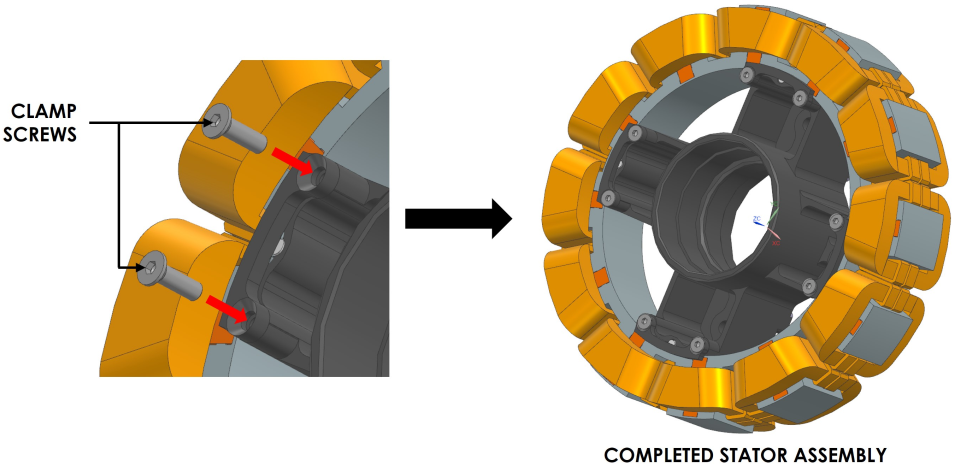

Figure 64: Clamping of stator core to bracket

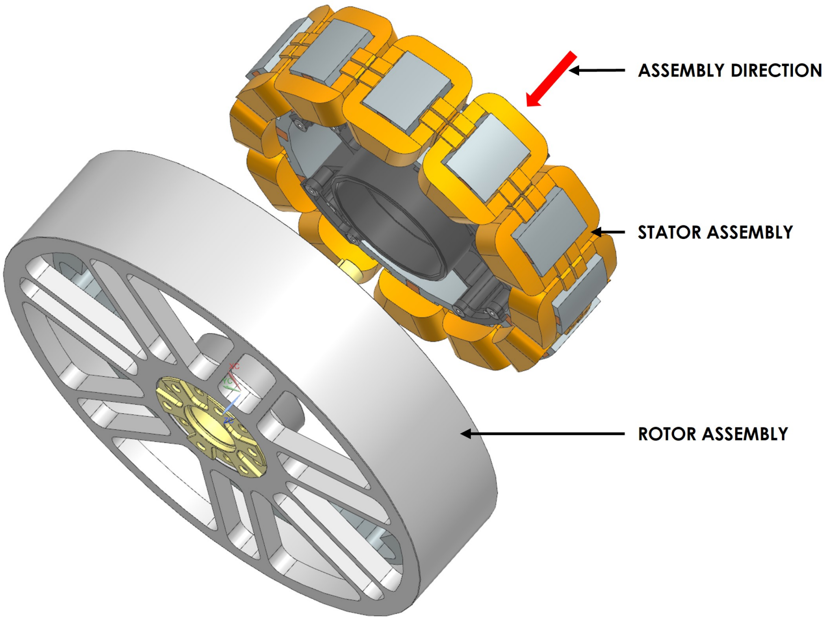

Figure 65: Insertion of stator assembly into rotor assembly

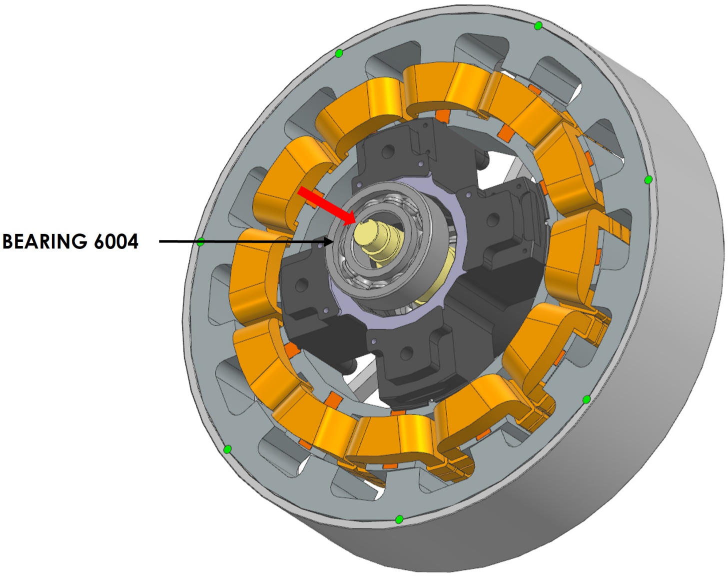

Figure 66: Installation of bearing 6004 on shaft

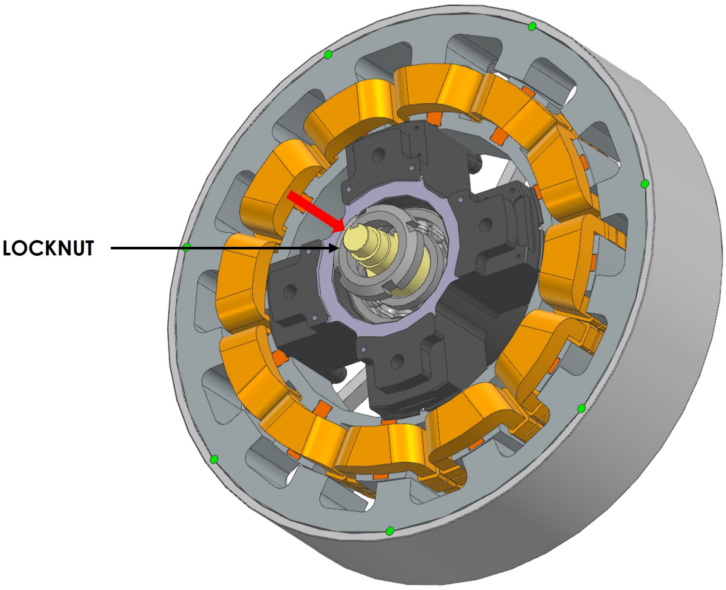

Figure 67: Installation of locknut on shaft

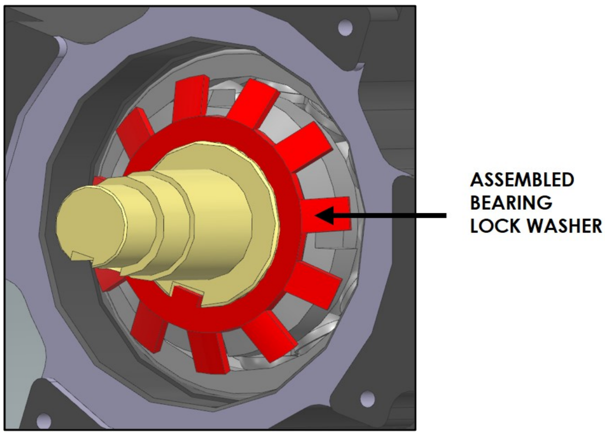

Figure 68: Bearing lock washer securing the locknut

Eigenständigkeitserklärung

Diese Erklärung gilt für Hausarbeiten, Studienarbeiten, Essays, einschließlich Bachelor- und Master-Arbeiten

(vgl. § 12 Abs. 9 und § 20 Abs. 4 RahmenO-BA/MA)

Hiermit versichere ich (Name, Matrikelnummer), **Aruli Karuppu Umapathi, 5008917**, dass ich die vorliegende Arbeit (Titel, Seminar, Semester **Design and Preparation of a Manufacturable Flux-Switching Machine, Master Thesis (11491), 6th Semester,** dass ich die vorliegende Arbeit selbständig, ohne fremde Hilfe und ohne Benutzung anderer als der angegebenen Hilfsmittel angefertigt hat. Die aus fremden Quellen (einschließlich elektronischer Quellen) direkt oder indirekt übernommenen Gedanken sind ausnahmslos als solche kenntlich gemacht. Wörtlich und inhaltlich verwendete Quellen wurden entsprechend den anerkannten Regeln wissenschaftlichen Arbeitens zitiert. Insbesondere sind alle Anwendungen von generativen KI-Methoden explizit ausgewiesen und dokumentiert worden. Die Arbeit ist nicht in gleicher oder vergleichbarer Form, auch nicht auszugsweise im Rahmen einer anderen Prüfung bei einer anderen Hochschule vorgelegt worden. Sie wurde bisher auch nicht veröffentlicht.

Ich erkläre mich damit einverstanden, dass die Arbeit mit Hilfe eines Plagiatserkennungsdienstes auf enthaltene Plagiate überprüft wird.

Hiermit versichere ich außerdem, dass ich die „Satzung zur Sicherung guter wissenschaftlicher Praxis und zum Umgang mit Verdachtsfällen wissenschaftlichen Fehlverhaltens an der Brandenburgischen Technischen Universität Cottbus–Senftenberg vom 20. Juli 2023“ beachte (https://opus4.kobv.de/opus4-tu/frontdoor/deliver/index/docId/6774/file/31_Satzung.pdf).

______________________________	______________________________
Ort, Datum	Unterschrift